University of Nevada, Reno

Design, Characterization, and Control of a High-Bandwidth Serial-Kinematic Nanopositioning Stage for Scanning Probe Microscopy Applications

A thesis submitted in partial fulfillment of the requirements for the degree of Master of Science in Mechanical Engineering

by

Brian Jeffrey Kenton

Dr. Kam K. Leang/Thesis Advisor

August 2010

University of Nevada, Reno
Statewide • Worldwide

THE GRADUATE SCHOOL

We recommend that the thesis
prepared under our supervision by

BRIAN JEFFREY KENTON

entitled

**Design, Characterization, and Control
of a High-Bandwidth Serial-Kinematic Nanopositioning Stage
for Scanning Probe Microscopy Applications**

be accepted in partial fulfillment of the
requirements for the degree of

MASTER OF SCIENCE

Kam K. Leang, Ph.D., Advisor

Eric L. Wang, Ph.D., Committee Member

M. Sami Fadali, Ph.D., Graduate School Representative

Marsha H. Read, Ph.D., Associate Dean, Graduate School

August 2010

Abstract

This thesis focuses on the development of a new three-axis serial-kinematic nanopositioning stage for high-bandwidth applications. Particularly, the nanopositioner is designed to be integrated with commercial scanning probe microscopes (SPMs), such as scan-by-probe atomic force microscopes (AFMs), for video-rate imaging and high-throughput probe-based nanomanufacturing. The positioning stage employs uniquely designed compliant flexures for guiding the motion of the sample platform to minimize parasitic motion (runout) and off-axis effects compared to previous designs. Finite element analysis (FEA) predicts the dominant resonances along the fast (x-axis) and slow (y-axis) scanning axes at 25.9 and 5.96 kHz, respectively. The first mechanical resonance modes for each stage are axial (*i.e.* piston). A monolithic prototype is fabricated from aluminum alloy using the wire electric discharge machining process. The performance of the positioning stage is evaluated and the measured dominant lateral resonances in the fast and slow scanning directions are 24.2 and 6.00 kHz, respectively, which are in good agreement with the FEA predictions. In the vertical (z) direction, the measured dominant resonance is approximately 70 kHz. The lateral and vertical positioning range is measured at approximately 9×9 μm and 1 μm, respectively. Four approaches to control the lateral motion of the stage are evaluated for precision tracking at high-scan rates: (1) open-loop smooth inputs, (2) PID feedback, (3) discrete-time repetitive control implemented using FPGA hardware, and (4) model-based feedforward control. Atomic force microscope imaging and tracking results are presented to demonstrate the performance of the stage. It is shown that the stage can be utilized for video-rate AFM imaging with line rates in excess of 7,000 Hz. Compared to the positioning stage found on a basic commercial AFM system (*e.g.* NanoSurf EasyScan AFM), the newly developed nanopositioner offers an improvement in the line rate by a factor of 700 (10 Hz to 7,000 Hz).

Acknowledgment

I would first like to give sincere thanks to my adviser, Kam, for his patience and insight through the learning process, his encouragement when I was unsure, and his sincere honesty and friendship.

To Dr. Wang and Dr. Fadali, thank you for your support and guidance while serving on my thesis committee.

I would like to thank all of my friends and colleagues for their encouraging support and honesty. To Yingfeng Shan, thank you for your insightful discussions and assistance in implementing the FPGA based repetitive controller.

I would like to thank the Nevada NASA Space Grant Consortium and the National Science Foundation (DUE 0852756 and EEC 0939261) for their financial support in this project.

To my family, I cannot imagine where I would be without your unconditional love and support. Thank you for showing me the value of an education, providing me with the tools and opportunities to achieve success, and encouraging me to continue.

Contents

List of Figures

List of Tables

Chapter 1

Introduction

This thesis presents the design, characterization, and control of a new three-axis high-bandwidth serial-kinematic nanopositioning stage for scanning applications. The specific objectives are to develop a three-axis high-speed nanopositioning stage (*i.e.*, nanopositioner) and integrate it with a commercial atomic force microscope (AFM) to produce video-rate AFM images. The proposed serial-kinematic nanopositioner is designed specifically for scanning purposes, and it utilizes unique flexure geometry and stage configurations to insure that the first mechanical resonance for each stage is the corresponding actuation direction (*i.e.* piston mode). Having the first mechanical resonance occur in the stages' actuation direction is critical in reducing cross-coupling effects which can cause image distortion.

1.1 Overview

Multi-axis nanopositioning is critical in many areas of micro and nano technology. For example, nanopositioners are used in optics to precisely position and steer light beams. In scanning probe microscopy (SPM) applications such as AFM [2], nanopositioners are used to position a probe tip relative to a sample surface to create sub-nanometer resolution images of both organic [3–10] and inorganic samples [2]. Additionally, nanopositioners are used with SPM systems for surface interrogation [11,12],

nanofabrication [13], surface manipulation [14], and high-density data storage [14,15]. In AFM imaging, a probe tip is positioned relative to a sample surface while probe-to-sample interactions are measured with a laser. The probe-to-sample interactions are then used to produce topographic images of samples such as live DNA, which cannot be imaged at comparable resolutions by any other means. Additionally, to capture the dynamic characteristics of these live biological cells, it is critical to scan at very high speeds. Therefore, the need for high-speed nanopositioning to enable video-rate AFM motivates the work in this thesis.

One key limitation to AFM imaging speed is low mechanical resonances of the nanopositioner. The triangle trajectories often used for raster scanning excites the resonances of the scanner resulting in tracking error and image distortion [16,17]. As a result, the scanning speed is typically limited to 1 to 10% of the lowest mechanical resonance of the scanner. Additionally, out-of-plane mechanical resonance modes such as rocking, can cause severe dynamic cross-coupling. Dynamic cross-coupling is out-of-plane motion caused by excited resonance modes. To reduce this effect, it is preferred that out-of-plane modes occur beyond the actuation (or piston) modes. Control methods such as feedforward- [16, 17] and feedback-based techniques [18] can be employed to improve the tracking performance of nanopositioners. However, significant improvement in operating bandwidth (particularly in the kHz range) is achieved by mechanical design, such as mechanically-stiff flexure-guided stages driven by piezo-stack actuators [19]. A variety of multi-axis high-speed nanopositioning stages have been proposed [9, 20–24]. However, most designs are limited by either cross-coupling, low displacement range, or high-power requirements. Therefore, there is still a need for improved mechanical design, specifically to increase range and to reduce the effects of cross-coupling. The major challenge faced in the mechanical design is that increased range leads to lower bandwidth due to decreased in- and

out-of-plane stiffness. In particular, the out-of-plane modes tend to occur before the axial actuation mode. This work focuses on a design where the actuation mode along all three scan directions occur before the out-of-plane modes.

1.2 Contribution

The contribution of this work is the development of a new high-speed serial-kinematic nanopositioning stage for scanning-type applications. The serial-kinematic design has one high-speed axis along the lateral directions and it uses one piezoactuator for each lateral degree of freedom. As a result, the design is low-cost because it avoids the need for multiple expensive amplifiers to drive the piezoactuators. The stage has an operating range of $9\times9\times1$ μm in the x, y, and z axes, while the first mechanical resonance for each stage occurs at 24.2, 6.00, and 70 kHz respectively. Novel flexure geometry and placement are proposed to increase the out-of-plane stiffness to insure that the first mechanical resonance for each stage occurs in the corresponding actuation direction. Compared to previous designs, this design increases the range by up to three times [9] while maintaining desired dynamic characteristics without increasing the the cost of drive electronics [25]. A commercial AFM is integrated with the nanopositioning stage to produce video-rate AFM images at over 30 frames-per-second (fps) and it scans at line rates greater than 7 kHz.

1.3 Methodology

1.3.1 Mechanical Design

For scanning-type applications, one lateral axis operates much faster than the other, making the serial-kinematic configuration ideal in this case. An advantage of such a

design is the ability to further constrain the out-of-plane motion of a one-degree-of-freedom stage through flexure placement and geometry, which is difficult to accomplish in multi-degree-of-freedom stages. This configuration has been shown to offer one of the fastest scanning speeds [9, 22]. However, existing serial-kinematic designs offer relatively short range motion, typically less than a few micrometers [9].

To limit the effect of cross-coupling, the out-of-plane stiffness of the stages is increased by designing vertically stiff flexures and placing them at the corners of the stages. Parametric equations were derived to study the effects of the quantity of flexures n, flexure length L, and thickness t. It was determined that by increasing the quantity of flexures and decreasing the flexure thickness (and length), the vertical stiffness of the beam flexure was dramatically increased. To further increase the vertical stiffness the center section of the flexure was "thickened" to produce a serial-compliant double-hinged flexure.

A novel z-stage configuration is proposed which improves the mechanical resonance of the x- and z-stages by reducing the overall mass and profile of the x-stage and further constraining out-of-plane motion of the z-stage. The x-stage mass and profile are reduced by recessing the z-piezoactuators within the x-stage and hollowing out the center section. The mechanical resonance of the vertical z-axis is increased by constraining the free end of the piezoactuator with a plate flexure. The plate flexure guides the motion in the z-actuation direction while increasing out-of-plane stiffness to minimize the effects of bending modes. Such modes can significantly limit the positioning speed by allowing the sample platform to rock side-to-side.

A prototype design is fabricated from 7075 aluminum using traditional machining and wire electric discharge machining processes. The machined stage body is assembled with plate-stack piezoactuators and characterized to determine it's performance.

1.3.2 Testing, Control, and AFM imaging

The performance of the nanopositioner are verified by testing to determine the flexure stiffness, maximum range, and dynamic characteristics. Four approaches to control the lateral motion of the stage are evaluated for precision tracking at high-scan rates: (1) open-loop smooth inputs, (2) PID feedback, (3) discrete-time repetitive control implemented using FPGA hardware, and (4) model-based feedforward control. The prototype stage is integrated with a commercial SPM (NanoSurf easyScan 2 AFM, 10 Hz max line rate) to demonstrate improved scan speed with line rates greater than 7 kHz.

1.4 Organization

This thesis is organized as follows. Chapter 2 presents a background of nanopositioning systems, piezoactuators which are used to drive high-performance nanopositioners, compliant flexures which are used to guide the motion of the stages, and scanning probe microscopes. Chapter 3 presents the details of the mechanical design, along with the fabrication and assembly of the three-axis high-bandwidth nanopositioning stage. Chapter 4 describes the drive electronics used to control motion of the nanopositioner as well as position sensors to measure displacement. Chapter 5 presents the mechanical characterization of the fabricated stage. Specifically, the in-plane flexure stiffness, displacement range, cross-coupling, and frequency response functions are measured. Chapter 6 presents the four control techniques applied to the system. Chapter 7 presents the tracking and imaging results, followed by a discussion in Chapter 8 discusses the results from this work. Finally, conclusions are presented in Chapter 9.

Chapter 2

Background

This chapter provides a background on positioning at the nanometer scale and the use of nanopositioners in AFM applications. Section 2.1 explains nanopositioning and reviews current piezo-actuated nanopositioning systems. Section 2.2 gives the history and background of piezoactuators as well as essential mechanical properties, basic production methods, and different types of actuators. Section 2.3 provides a brief introduction to compliant mechanisms. Finally, Section 2.4 explains the importance, history, and basic mechanical configurations of atomic force microscopes.

2.1 Micro/Nano Positioning Systems

A positioning system is simply a mechanical system that moves an object to a specific location or along a desired path. Typically, the object of interest is fixed to a moving platform (or stage) and then positioned relative to a tool. Operating range, precision, and achievable positioning speed are important characteristics of a positioning system, large or small.

2.1.1 Example: Macro-Scale Positioning System

Take for example the common three-axis computer numeric controlled (CNC) milling machine such as the one shown in Fig. 2.1. The two-axis x, and y, positioning stage

holds the part that work is being done to and moves it in the xy-plane relative to the milling tool (spindle and cutter). A vertical z-positioner then moves the milling tool relative to the part on the xy-stage. Through the linear motion of the part on the xy-stage and the vertical motion of the mill relative to the part, the CNC machine enables three-axis milling to be done through computer control. The total x, y, and z travel of the CNC machine shown in Fig. 2.1 is 18× 9.5×16.25 inches with accuracy near 0.0013 inch[1].

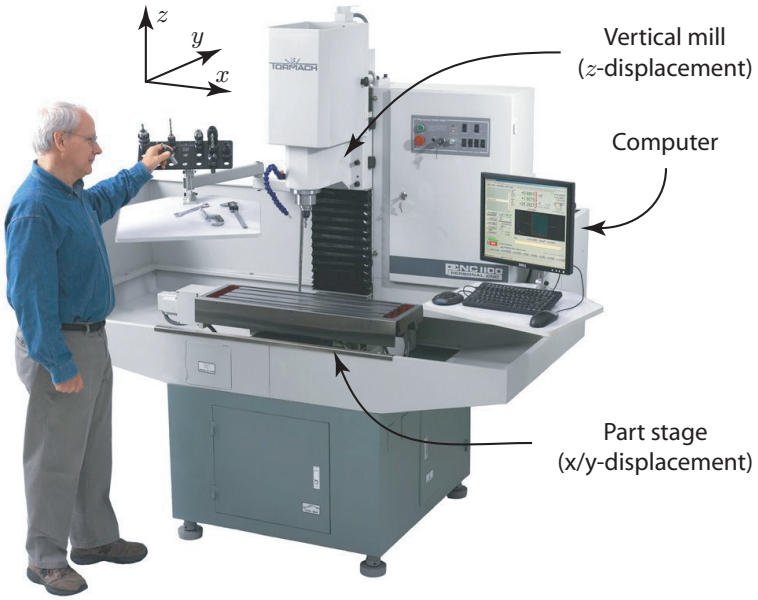

Figure 2.1: Linear three-axis CNC milling machine (www.tormach.com).

2.1.2 Positioning at the Nanometer Scale

Nanopositioning stages are much like CNC milling machines in that they move objects with a specific degree of precision but over a much smaller range. The typical range of a translational nanopositioning stage is between 3 and 500 μm while the accuracy must be less than or equal to 100 nm to be classified as having nanometer-precision.

[1] www.tormach.com/Product_PCNC_performance.html

Figure 2.2 shows an example of a small variety of commercial three-axis translational x, y, z nanopositioning stages with different ranges, actuators, drive configurations, and kinematic configurations. It is noted that many stages also offer rotation (up to six-degrees-of-freedom) for applications such as beam steering.

The long-range stage shown in Fig. 2.2(a) has a maximum displacement of 4.0 mm through a dual drive configuration. The fixed differential drives on the sides offer coarse adjustment up to 4.0 mm while nanometer-precision positioning is performed through internal piezoactuators with a resolution of 20 nm. Although this configuration offers a large range-of-motion with precise alignment, the coarse adjustment limits the long-range repeatability to 1.0 μm on axis accuracy.

The stage in Fig. 2.2(b) is an example of a long-range serial-kinematic nanopositioning stage which uses displacement amplifiers to achieve 300 μm of x-, y-, z-displacement. In a serial-kinematic design, the actuators for each degree of freedom are connected in series relative to ground. The y-stage must be larger than the x-stage to carry the actuator and mechanisms for the x-stage. The increased size of the outer y-stage causes its first mechanical resonance to be less than the inner x-stage.

The parallel-kinematic stage in Fig. 2.2(c) has shorter range-of-motion of $33 \times 33 \times 14$ μm (x, y, z) and as a result higher mechanical resonances. In a parallel-kinematic design, the actuators are connected in parallel from the stage to the ground which causes the resonance frequencies for the x, y, and z axes to be very close in value.

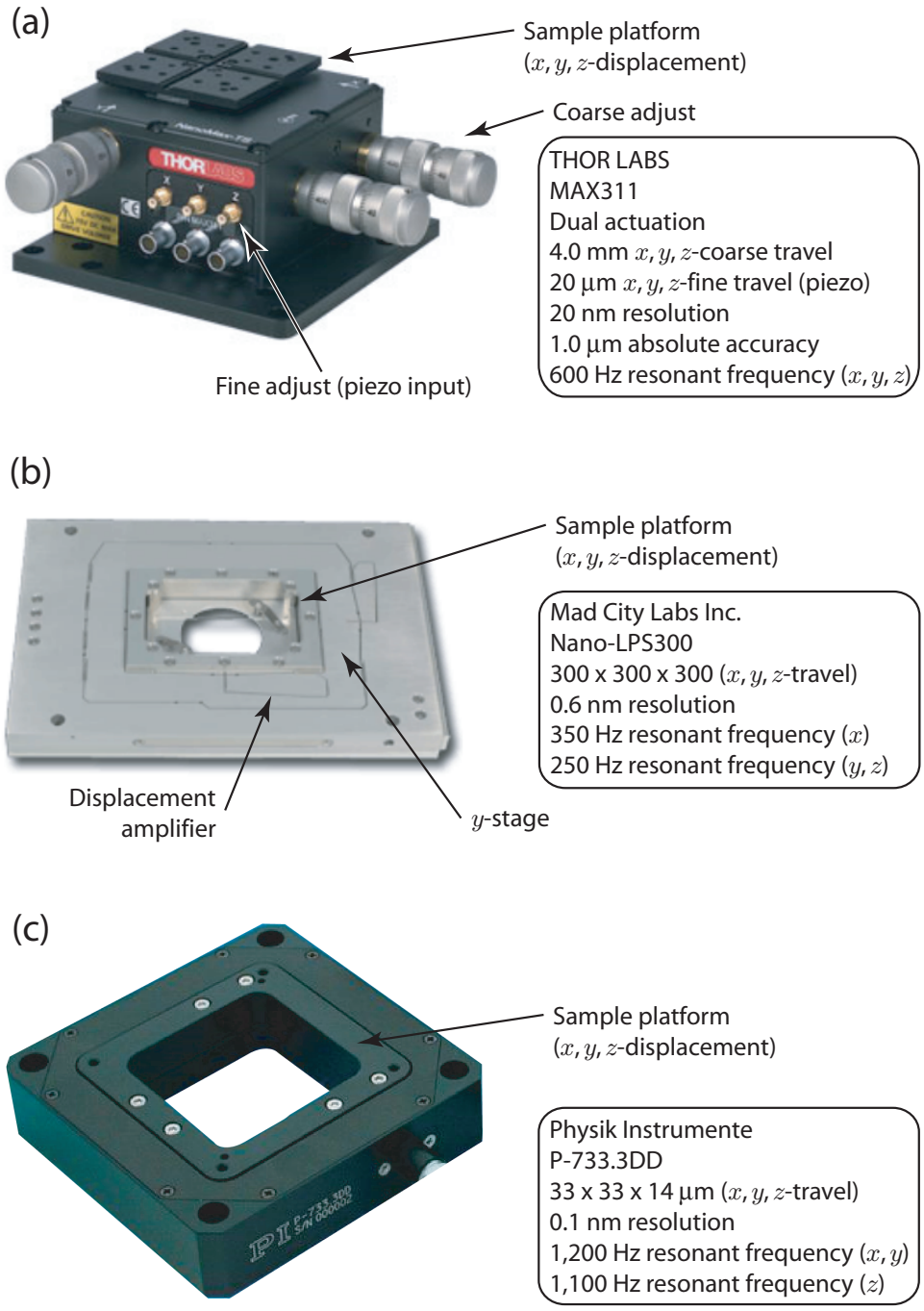

Figure 2.2: Commercial micro/nanopositioning stages.

Figure 2.3 provides a more detailed view of a two-axis serial-kinematic nanopositioning stage to show key mechanisms used. Piezoactuators are chosen for nanopositioning systems because they are mechanically stiff, have many diverse forms and

applications, and have nearly unlimited resolution. More information on piezoactuators will be provided later in Sec. 2.2. Flexures are used to guide the motion of the stage in the desired directions and reduce cross-coupling. The x, and y actuators shown are 5 x 5 x 12 mm plate-stack piezoactuators which have a free stroke of 14.7 μm. In this specific design, the displacement of the piezoactuator is mechanically amplified by a cantilever beam to produce approximately 40 μm of displacement in the lateral x-, and y-axis. Although this is an effective way to achieve large displacements, the decreased effective stiffness at the stage body reduces the mechanical resonance values. The first mechanical resonances are approximately 400 and 600 Hz in the corresponding x, and y axes.

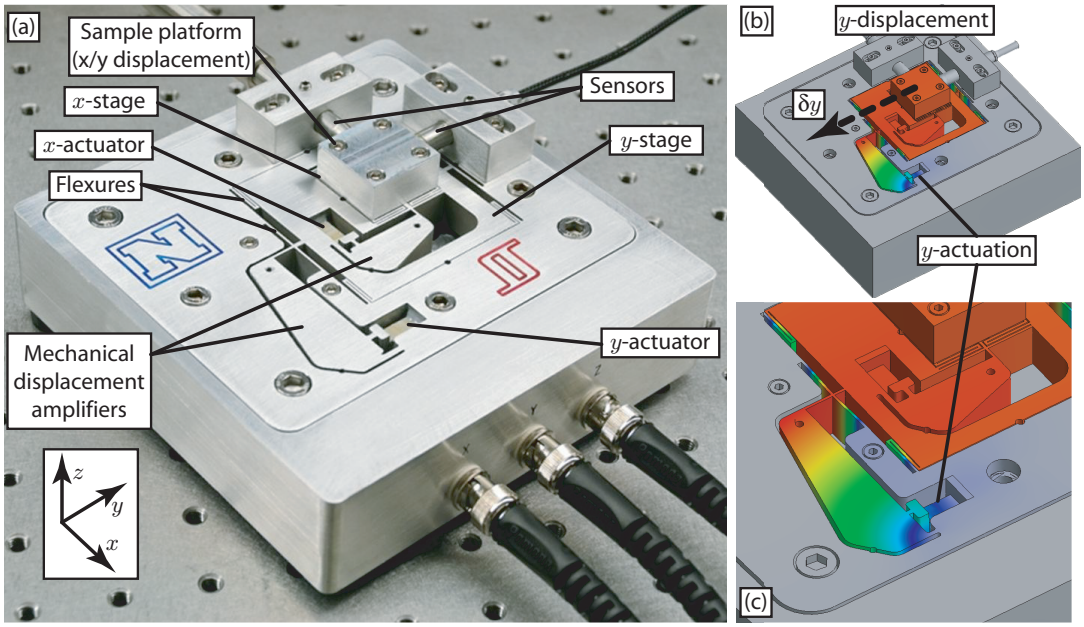

Figure 2.3: Two-axis serial-kinematic x, y piezo-actuated nanopositioning stage; (a) assembled prototype, (b) FEA simulation of y displacement, and (c) expanded image of FEA simulation.

2.1.3 Review of Nanopositioners

A wide variety of multi-axis nanopositioning stages have been developed; Table 2.1 summarizes a small collection of high-performance stages. The performance of the positioners in Table 2.1 are then compared to commercial positioners in Fig. 2.4. The positioners are shown in Figs. 2.5 and 2.6.

The simplest and most effective way to achieve three-axis motion is to employ sectored tube-shaped piezoelectric actuators [26]. However, the mechanical resonance of piezoelectric tube scanners [Fig. 2.5(a)] is typically less than 1 kHz in the lateral scan directions, thus limiting the scan speed [27–30]. Additionally, the mechanical cross-coupling causes undesirable image distortion [30]. In general, the maximum positioning bandwidth in open-loop without compensation is $1/100^{th}$ to $1/10^{th}$ of the dominant resonance. Shear piezos [Fig. 2.5(b)] because of their geometry have high mechanical resonances [20]. The major drawback of shear-type piezoactuators is they provide limited range, typically less than 1 μm. Tuning forks have been implemented in both sample scanning [21, 22] and in probe scanning SPMs [31] as shown in Figs. 2.5(c) and (d). The tuning-fork-based sample scanners are mechanically simple, but the small dimensions of the quartz tuning fork limits the scan range and scanning motion is typically sinusoidal. Flexure-guided piezo-actuated scanning stages [32], both direct drive serial-kinematic [1,9] and parallel-kinematic [33] configurations, have been developed for high-speed purposes. A variety of flexure-guided sample scanners are shown in Figs. 2.5(e) and 2.6(a) through(d). The advantages of flexure-guided scanners are high mechanical resonances and low cross-coupling effects. Multiple piezoactuators per degree-of-freedom have been used to increase range and scanning bandwidth [Figs. 2.5(e) and 2.6(d)], but at the cost of increased power to drive the piezoactuators at high frequencies [9,33]. Designs which involve mechanical amplification have been studied to increase range without having to increase the ac-

tuator's length as shown in Figs 2.6(a) and (b) [32, 34, 35]. However, the added mass of the mechanical amplifier along with the flexible linkages, and decreased effective stiffness at the stage lowers the mechanical resonance. In general, a tradeoff must be made between range and speed.

Table 2.1: Summary of common nanopositioning designs.

Reference	**Configuration**	**Range** (μm)	**Dominant Res.** (kHz)	**Imaging/line rate (range)**
G. Schitter et al., 2004 [27]	Tube scanner	125 (x/y)	0.71 (x) 0.70 (y)	122 lines/s (13.5×13.5 μm)
G. Schitter et al., 2008 [28]	Tube scanner Dual stage (z)	n/a	6.35 (x/y) 80 (z)	3 lines/s (25 μm)
A.J. Fleming, 2009 [29]	Tube scanner Dual stage (z)	100 (x/y) 10 (z)	0.68 (x/y) 23 (z)	6.25 lines/s (25×25 μm)
M.J. Rost, 2005 [20]	Shear piezo	0.3 (x/y) 0.20 (z)	∼64 >100	80 frames/s (128×128 px)
T. Ando et al., 2008 [9]	Flexure-guided	1 (x) 3 (y) 2 (z)	45 360 ("self")	33 frames/s (100×100 px)
L.M. Picco et al., 2007 [22]	Tuning fork (x) Flexure-guided (y)	<1 (x) 2 (y)	100 40	1000 frames/s (100×100 px)
G. Schitter et al., 2008 [33]	Flexure-guided	13 (x/y) 4.3 (z)	>20 33	7810 lines/s (n/a)
Y.K. Yong et al., 2009 [34]	Flexure-guided	25 (x/y)	2.73	n/a

The general relationship between range and unloaded resonant frequency is shown in Fig. 2.4. In this plot, a variety of custom high-performance nanopositioners (academic research) are compared to positioners from commercial manufacturers. The range is plotted with respect to the resonant frequency for each stage when provided. When full details are not provided for multi-axis positioners, it is assumed that the resonant frequency is provided for the stage with the largest displacement, and therefore;

the largest range is plotted with respect to the lowest resonant frequency. Theoretically, the maximum attainable range for a given actuation (longitudinal) resonance is $R = 567,460f^{-1}$ (as derived in Sec. 3.3.2) where R is range and f is resonant frequency. This value is for a fixed-free piezoactuator with a modulus of elasticity of 33.9 GPa and a density of 8000 kg/m^3 assuming 1 μm of travel per mm of piezo length. This relationship is shown in Fig. 2.4 as a dashed line. The commercial and custom nanopositioners in Fig. 2.4 are well below this theoretical limit. A trend line depicted as a solid line shows that for commercial and custom nanopositioners, the relationship is approximately $R = 30,688f^{-0.916}$. Building a nanopositioner that attains the maximum is extremely difficult due to the fact that added end mass, such as a sample, stage, or flexure to the piezoactuator decreases the actuation resonance dramatically. For example, when a 2.53 g mass is added to a 5×5×10 mm piezoactuator, the actuation resonance decreases from 56.8 to 25.9 kHz due to the effective mass increasing from 0.67 to 3.20 g. Additionally, if the out-of-plane stiffness is less than the actuation stiffness, the first mechanical resonance will be even less than the actuation resonance. The major focus of this thesis is on decreasing the effective mass of the high-speed stage and increasing the out-of-plane stiffness.

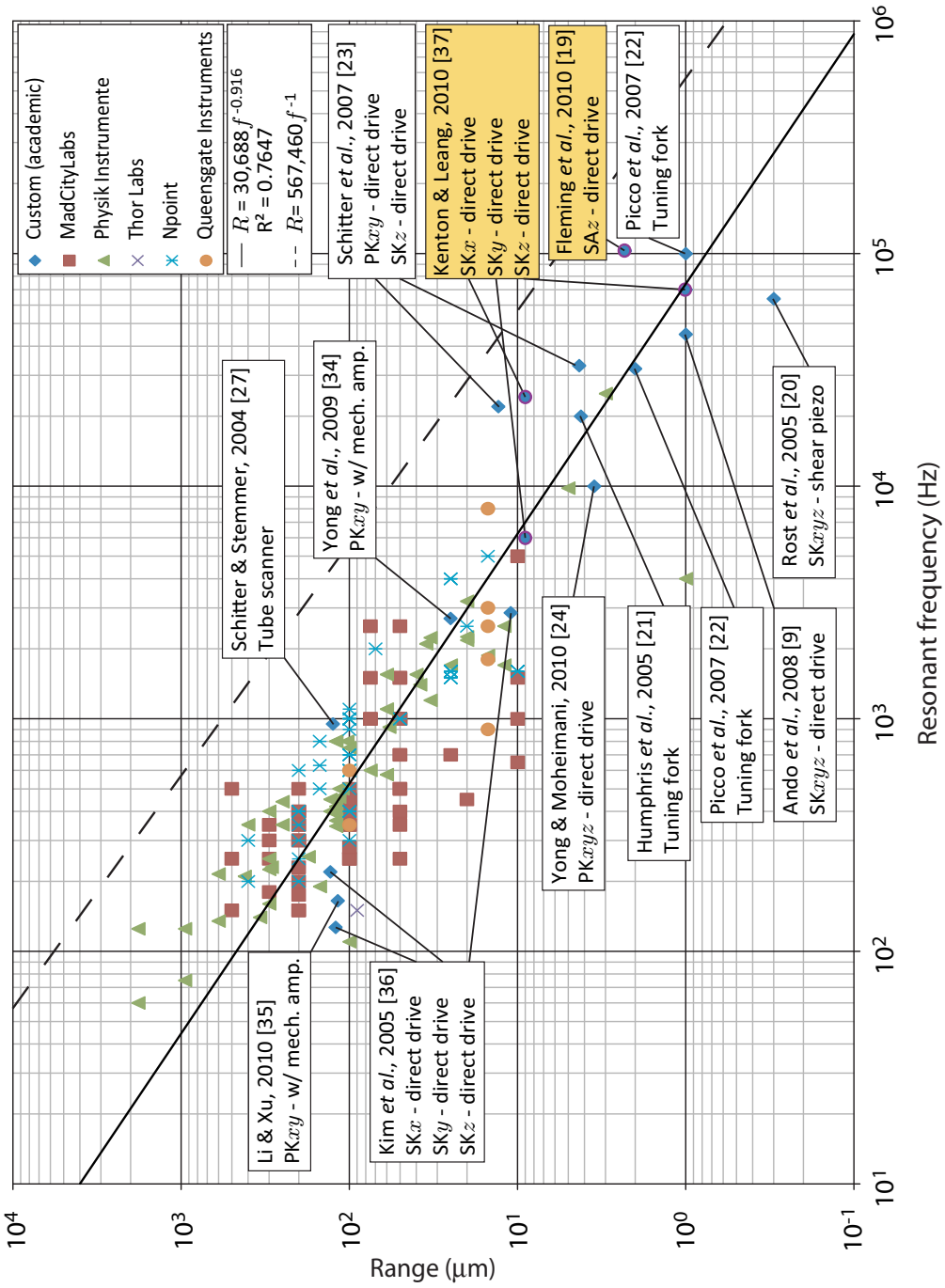

Figure 2.4: High-performance commercial and custom nanopositioners plotted as range R with respect to resonant frequency f. The solid line represents a linear least-square-error line fit to the data points. The dashed line represents the theoretical first actuation mode mechanical resonance for a fixed-free piezoactuator assuming 1 μm of travel per 1 mm length for a piezoactuator. SK = serial-kinematic, PK = parallel-kinematic, SA = single-axis, x, y, z refers to axis being referenced.

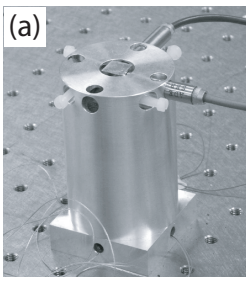

Sectored piezo tube
Bhikkaji et al., 2007 [18]
850 Hz

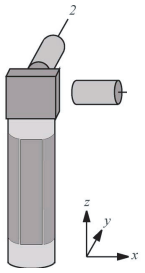

similar to
Schitter & Stemmer, 2004 [27]
125 µm, 950 Hz (x, y)

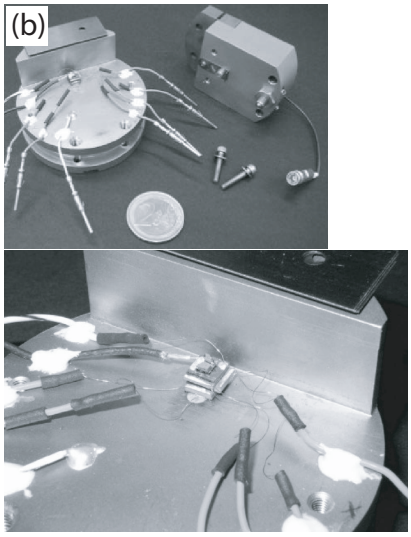

Rost et al., 2005 [20]
0.3 µm, 64 kHz (x, y)
0.2 µm, 100 kHz (z)

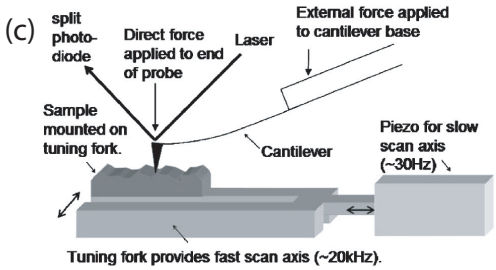

Humphris et al., 2005 [21]
4.2 µm, 20 kHz (x)

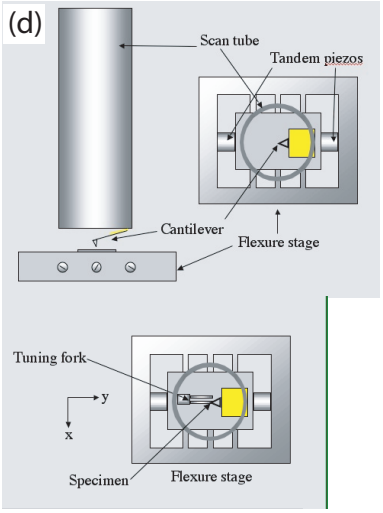

Picco et al., 2007 [22]
1 µm, 100 kHz (x)
2 µm, 32kHz (x)

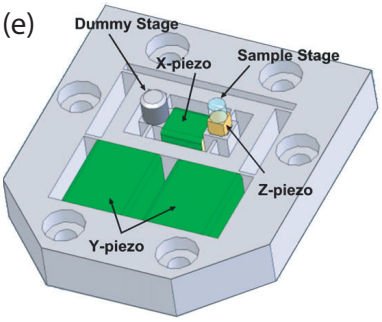

Ando et al., 2008 [9]
1 µm, 45 kHz (x)

Figure 2.5: High-performance nanopositioners: (a) is a common tube scanner with an aluminum block fixed to the free end, (b) is a 3-DOF shear-stack/plate-stack (x, y, z) configuration, (c) and (d) are both serial-kinematic configurations that use tuning forks for the high-speed scan stage, and (e) is a serial-kinematic x, y, z that uses flexures to guide the motion of the piezoactuators.

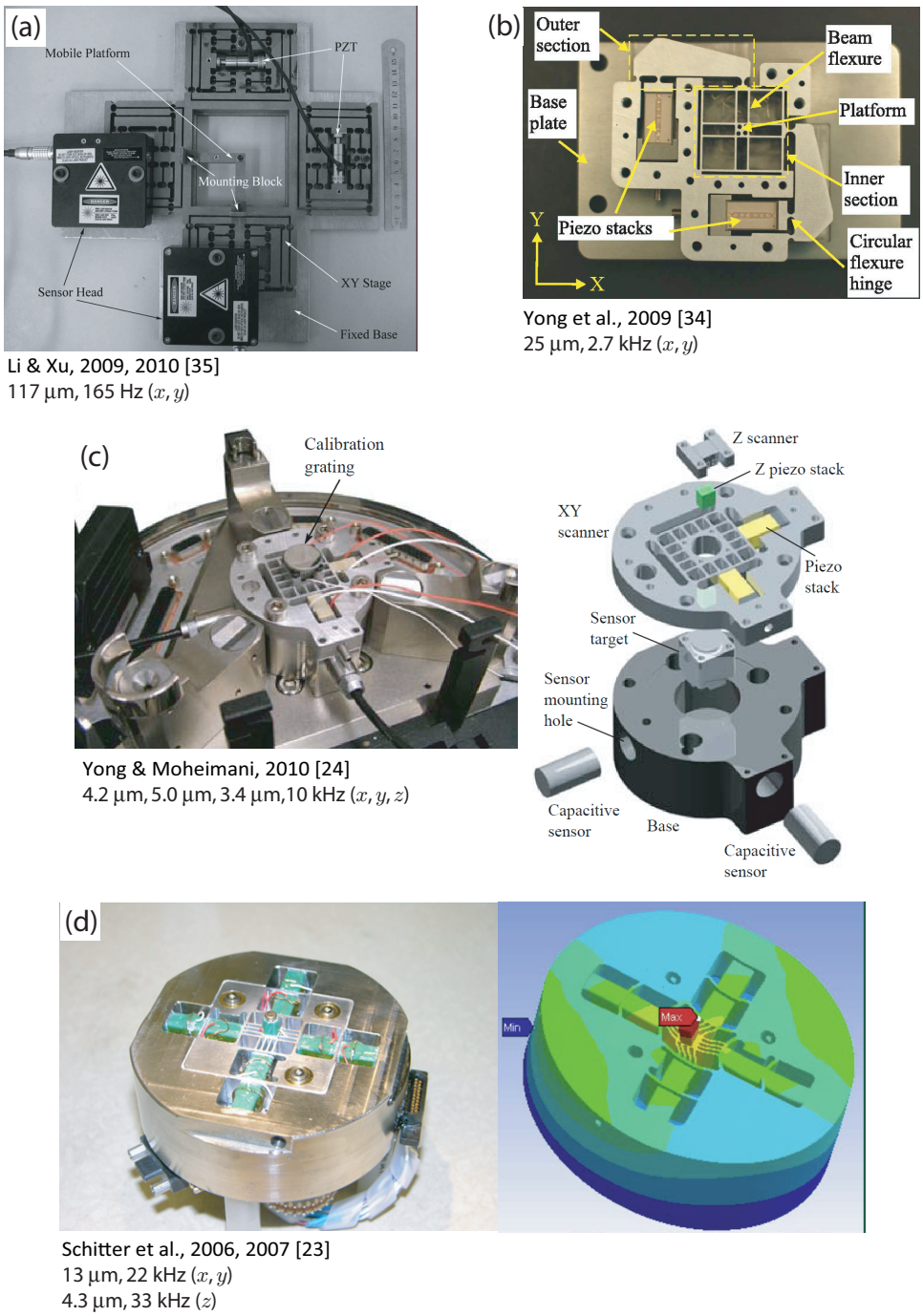

Li & Xu, 2009, 2010 [35]
117 µm, 165 Hz (x, y)

Yong et al., 2009 [34]
25 µm, 2.7 kHz (x, y)

Yong & Moheimani, 2010 [24]
4.2 µm, 5.0 µm, 3.4 µm,10 kHz (x, y, z)

Schitter et al., 2006, 2007 [23]
13 µm, 22 kHz (x, y)
4.3 µm, 33 kHz (z)

Figure 2.6: High-performance parallel-kinematic nanopositioners: (a) and (b) utilize mechanical displacement amplifiers to increase the range, (c) and (d) use a direct drive configuration to provide higher resonant frequencies.

2.2 Piezoactuators

Piezoelectric materials are materials that produce voltage when they are stressed and likewise are stressed (and strained) when voltage is applied to them. The root word piezo comes from the Greek word *piezein*, which means press or squeeze thus the word piezoelectric means pressure-electric. The theory that electricity could be produced when a material is stressed was first proposed by Charles Augustine de Coulomb (1736-1806) [38]. Initial experiments performed by Abbé René Just Haüy (1743-1822) and Antoine Césear Becquerel (1788-1878) in 1820 were unsuccessful until 1880 when Pierre and Jacques Curie experimentally proved that polar electricity could be produced by applying pressure to hemihedral crystals with inclined faces such as such as quartz, topaz, and cane sugar [38]. A year later, piezoelectric actuators were established when they showed that applying an electric field across these materials produced displacement.

Many piezoelectric materials are ferroelectric in that they exhibit spontaneous polarization in the absence of an electric field when they are below their inherent ferroelectric Curie temperature T_C. An example of some ferroelectric materials are Rochelle salt ($NAKC_4H_4O_6{\cdot}4H_2O$), potassium dihydrogen phosphate (KH_2PO_4), potassium niobate ($KNbO_3$), and lead zirconate-titanate ($Pb[ZrO_3,TiO_3]$, PZT). The material PZT is the most commonly used in piezoactuators [39]. Figure 2.7 shows a PZT unit cell above [(a) and (b)] and below [(c) and (d)] its curie temperature where (a) and (c) are isometric views showing the crystal structure and (b) and (d) are side views to help show the elongation due to spontaneous poling [39–41]. Groups of unit cells with the same orientation in a ceramic are called a Weiss domains [41].

In the production of PZT actuators, the ceramic is first processed and formed into its desired shape. In this initial form, the PZT is in its final shape, but cannot yet be used to actuate because the Weiss domains of the unit cell dipoles are randomly

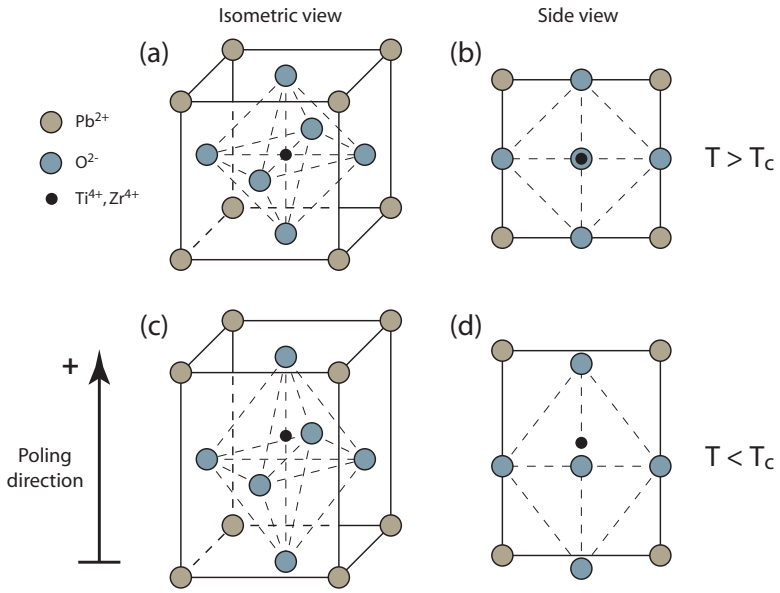

Figure 2.7: Unit cell crystal structure of lead zirconate-titanate ($Pb[ZrO_3,TiO_3]$, PZT) (a) shown above the Curie temperatre in isometric view and (b) side view and again with (c) voltage induced displacement in an isometric and (d) side view.

oriented. Figure 2.8(a), shows a side view of a PZT block in its final shape with randomly oriented Weiss domains. In order for the PZT block to actuate, the Weiss domains must be oriented in the same general direction through the process of poling as shown in Fig. 2.8(b) and (c). In this process, the PZT ceramic is heated above its Curie temperature while a DC voltage is applied to the electrodes. Raising the temperature of the PZT ceramic above its Curie temperature causes the poled unit cells to return to their un-poled state. By applying a high DC voltage to the ceramic while cooling, the Weiss domains are oriented in the desired direction. Once cooled, the Weiss domains are locked in the general poled direction. From here, voltage can be applied to the piezoelectric crystal to produce displacement.

The simplest piezoactuator, shown in Fig. 2.9(a) is a block type axial piezoactuator. In this case, the piezoactuator is composed of a single PZT ceramic in a cubic or block shape. Application of an electric field across the block (through the electrodes) produces axial displacement (*i.e.*axial stress and strain). The main problem with

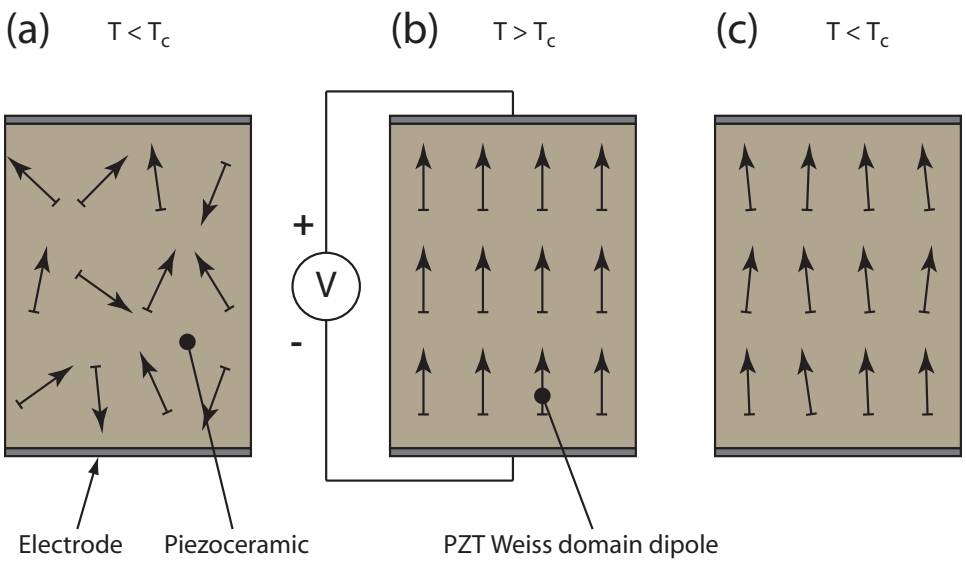

Figure 2.8: PZT ceramic with (a) randomly oriented Weiss domains of unit cells, (b) heated above the Currie temperature with an electric field applied to the electrodes, and (c) a "poled" PZT ceramic.

block actuators is that they require high voltage loads due to their thickness (distance between the electrodes). As the distance between the electrodes increases, the required voltage to achieve full displacement increases. To reduce the required voltage, plate-stack actuators (b) are made by stacking thin sheets of PZT piezoceramic on top of each other. The individual stacks are then wired in parallel. The reduced distance between the electrodes reduces the required voltage as a function of the thickness. In production, the sheets of piezoceramic material ranging from 2 to 100 μm thick, and are laminated together to form plate-stack piezoactuators. The limitation of stack type actuators is the increased manufacturing cost and limited tensile loads often seen in dynamic applications. Plate-stack actuators can be formed to produce both axial Fig. 2.9(b) and (b) shear displacements. Linear three-axis displacement can be achieved by stacking two lateral x, y shear plate-stack piezoactuators with an axial z plate-stack piezoactuator to produce displacements of 10×10×10 μm with an unloaded first mechanical resonance of 30 kHz (PI P-153.10H). However, when

loaded, the mechanical resonance decreases dramatically.

Additional types of piezoactuators are shown in Fig. 2.9 which include (d) ring-stack piezoactuators, (e) sectored tube piezoactuators, and (f) bimorph piezoelectric actuators. Ring-stack piezoactuators are like traditional plate stack actuators in that

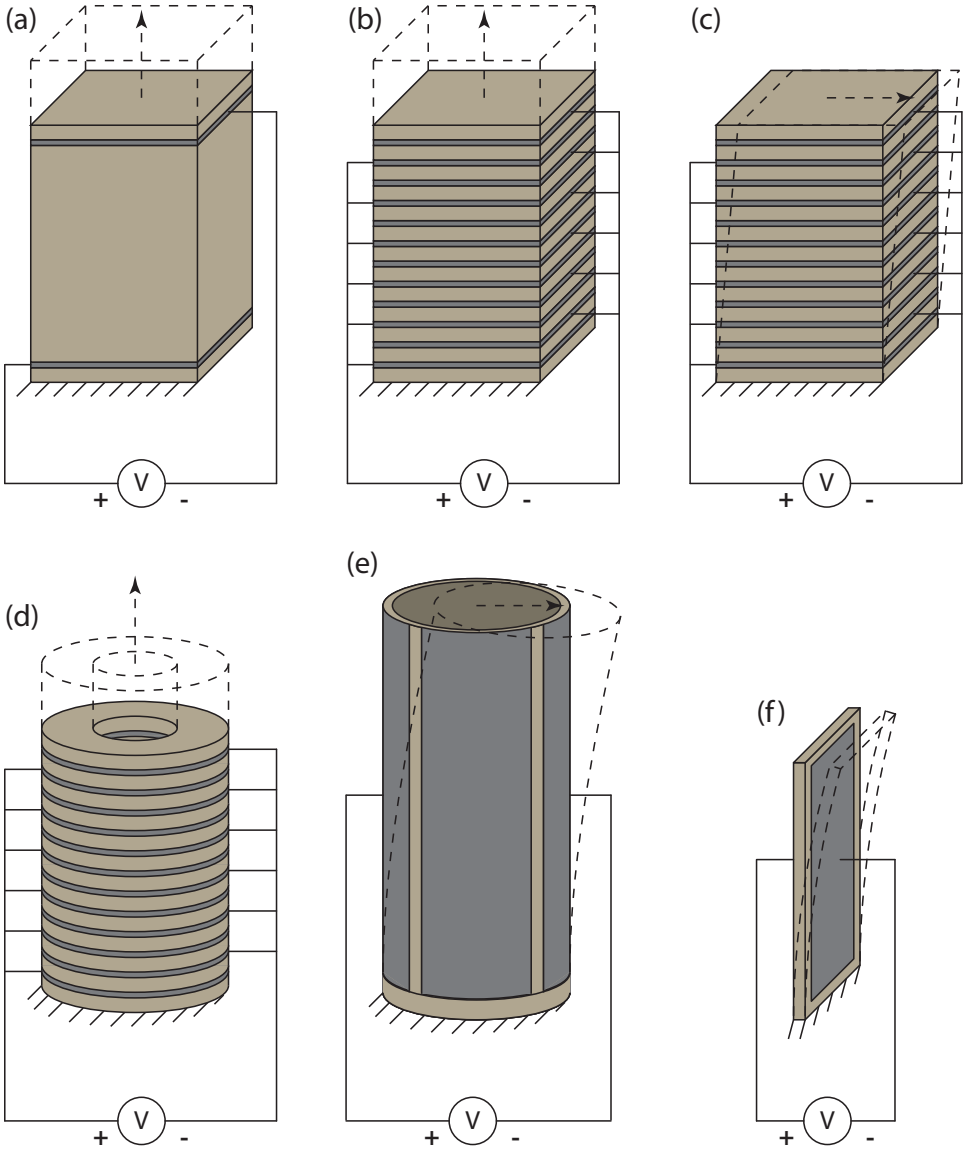

Figure 2.9: Some common piezoactuators including (a) axial block piezoactuator, (b) axial plate-stack piezoactuator, (c) shear plate-stack piezoactuator, (d) axial ring-stack piezoactuator, (e) sectored-tube piezoactuator, and (f) bimorph piezoactuator.

they are primarily used for axial displacements. The advantage of a ring-stack actua-

tor is increased bending and torsional stiffness due to the increased radius of gyration for an equivalent cross-sectional area. Higher cost of ring-stack actuators however make them less desirable than rectangular plate stacks. Sectored tube piezoactuators offer long range multi degree of freedom displacements (80 μm xy) but with relatively low resonance frequencies around 500 Hz x, y. Bimorph piezoactuators act as a cantilevered beam and produce displacements at the free end through bending.

For flexure-guided linear displacements, plate-stack piezoactuators have become the standard actuator for nanopositioning applications. Their high stiffness and precise displacements enable quick and accurate displacements while their atomic resolution is only limited by power supply noise and closed loop sensor resolution.

2.3 Compliant Mechanisms

Flexure based compliant mechanisms are dynamic structures that rely on the elastic deformation of material to provide freedom of motion [42]. For example, with the common tweezer shown in Fig. 2.10(a), the displacement and return of the gripping end is enabled by the mechanisms compliance. An alternative configuration to the simple compliant tweezer would be a hinged tweezer with a spring return. The compliant beam flexure of a tweezer is simple in that the stress and bending displacement is spread out through the length of the beam. An example of a more complex flexure based mechanism is the gripper shown in Fig. 2.10(b). In this case, the injection molded plastic gripper utilizes four flexures to create a four-bar compliant mechanism. Displacement of the handle produces displacement of the gripper, as shown closed in (c). In this case, a mechanism that would be made up of four or more pieces is now made up of just one that does not require assembly. Figure 2.10(d) shows discoloration of the flexures due to high stress values.

The benefits of monolithic compliant mechanisms are that there is no frictional

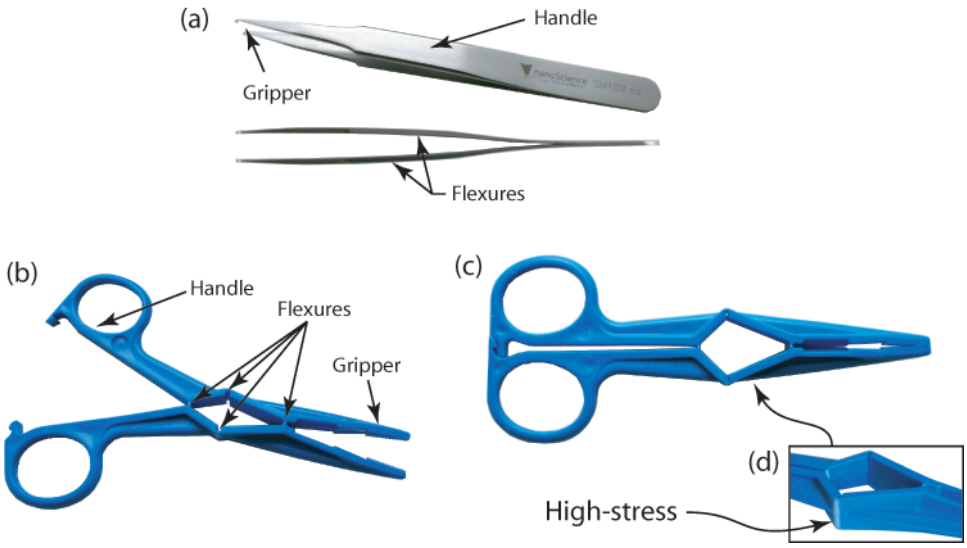

Figure 2.10: (a) Household tweezers utilize compliant flexures for displacement and return force. (b) Compliant pliers utilize four flexures to create a four-bar mechanism from one piece of injection molded plastic. The pliers are shown closed in (c) while (d) shows flexure discoloration due to high stress values.

loses or hysteresis, no backlash, no need for lubrication, they are compact, easy to fabricate, can require little to no assembly, and are virtually maintenance free [42, 43]. The negative aspects of flexure hinge based mechanisms are that additional displacement losses can occur due to unanticipated material compliance, cyclic failure can occur if stress values are above the materials fatigue load limit, the displacement limits are relatively low, the rotation is complex due to the combination of bending, shear, axial, and torsional deformation, the center of rotation of a short flexure is not fixed when shear and moment loads are combined, and flexure characteristics can be sensitive to temperature changes. Accounting for material fatigue is especially important for materials that do not have a fatigue load limit such as aluminum. For these materials, any load will cause the material to fail if over cycled.

Flexures are often used in micro- and nanopositioning stages to guide the motion of a stage in a desired direction, and restrict the stage from moving in undesired directions. Figure 2.11 illustrates the axial displacement of a piezo-actuated flexure-

guided stage. In (a), the stage is in its initial location where the piezoactuator has no voltage applied to it. Stage displacement due to piezoactuation is shown in (b) where the flexures are deformed allowing the stage to move along the x-axis. Beam flexures are used in this configuration in the presented design to allow axial motion of the stage by being *soft* in the axial direction, while limiting out-of-plane motion by being *stiff* in all other directions.

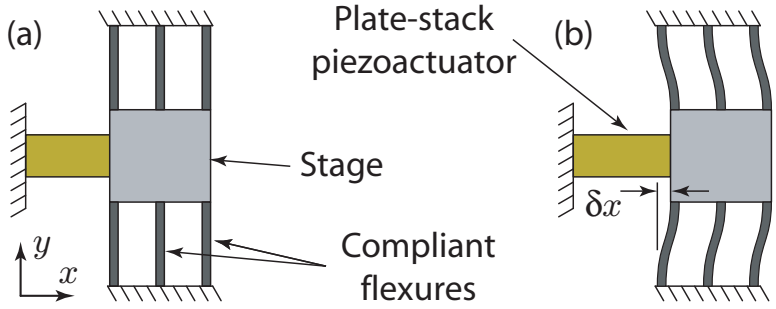

Figure 2.11: Top view of a piezo-actuated, flexure-guided stage, (a) undeformed, and (b) deformed due to piezoactuation.

2.4 Scanning Probe Microscopy

Scanning probe microscopes (SPM) scan the surface of a material using an ultra-sharp probe to obtain surface characteristics and manipulate matter at the nanoscale. A popular example of an SPM is the atomic force microscope. The AFM, invented in 1986 by G. Binnig, C. F. Quate and Ch. Gerber [2], uses an ultra-sharp tip attached to the free end of a micro-cantilever to image, interrogate, and manipulate material surfaces at the nano-scale. The imaging resolution of light microscopes is limited to approximately 190 nm due to the wavelength of the imaging light (360 nm wavelength). Electron microscopes improve the resolution to smaller than 0.5 nm, but require the samples to be dry and placed in a vacuum. Unlike visible light and electron microscopy, the AFM allows surfaces to be imaged at the nano-scale in both

wet and dry environments, as well as enables mechanical characterization such as friction, adhesion studies [11] and surface manipulation such as nano-fabrication, DNA sequencing [12], and high-density data storage [14]. For this reason, the AFM has become a critical tool for research at the nano-scale.

2.4.1 History

The first AFM [2] used a scanning tunneling microscope (STM) [44] to measure the deflection of an ultra-sharp nano-tip on the free end of a micro-cantilever beam as it traced the surface of a sample. The cantilever they used was hand fabricated out of aluminum foil with dimensions of 0.8-mm long by 0.25-mm wide by 25 μm thick. An ultra-sharp micro diamond tip was attached to the end of the cantilever beam as a stylus (probe) for tracing the sample surface. The cantilever was then oscillated at its mechanical resonance by a piezoactuator while a three-axis xyz piezoactuator was used to move a sample relative to the probe tip. The magnitude of the cantilever beam deflection varied due to the atomic forces between the tip on the cantilever and the sample surface and was used to produce topographic data. The initial setup produced three dimensional surface images with angstrom ($\mathring{A}$) resolution [2]. Later research produced images of cleaved graphite with resolution of 1.4 $\mathring{A}$ (0.14 nm) [45]. Since its invention, the AFM has maintained its general form but has undergone tremendous mechanical refinement.

2.4.2 AFM Mechanical System

The modern AFM, like its predecessor, traces the surface of a sample with an ultra-sharp tip attached to the free end of a soft cantilever to provide topographic data as it scans the surface of an x/y-plane. The two main scanning methods for AFM shown in Figure 2.12, are (a) probe scanning where the probe is moved relative

to the sample, and (b) sample scanning where the sample is moved relative to the probe. The simplest and most common actuator for both scan methods is the sectored tube piezoactuator as shown. In both methods, a scanning trajectory is formed by the relative motion of the cantilever probe to the sample. A raster scan trajectory [Fig. 2.12(c)] composed of a pure triangle x- and ramp y-trajectory, is the most common scan trajectory because data is evenly distributed about the scan plane. As the probe scans the surface, cantilever deflection is measured by the laser reflecting off the cantilever to the photodiode. The deflection of the cantilever is then used to produce topographic images.

2.4.3 Imaging Modes

The two imaging modes for AFM are *contact mode* and *tapping mode*, which refers to the way in which the cantilever is operated. In *contact mode* the cantilever acts as a static spring, as the probe is scanned across the sample surface. Figure 2.12(d) shows the path the probe tip follows as it traces the surface in *contact mode*. The atomic force interactions cause the relatively soft cantilever to deflect as it encounters elevation variances.

In *tapping mode* Fig. 2.12(e), the AFM cantilever is oscillated at or near its resonance frequency by an additional piezoactuator. As the probe encounters elevation variances, the atomic force interaction causes a phase and amplitude shift of the cantilever oscillation. The amplitude change is then used to produce the cantilever deflection data. The advantage of imaging in *tapping mode* over *contact mode* is that there is less interaction between the tip and the sample causing there to be less tip wear, and less damage to softer samples [46].

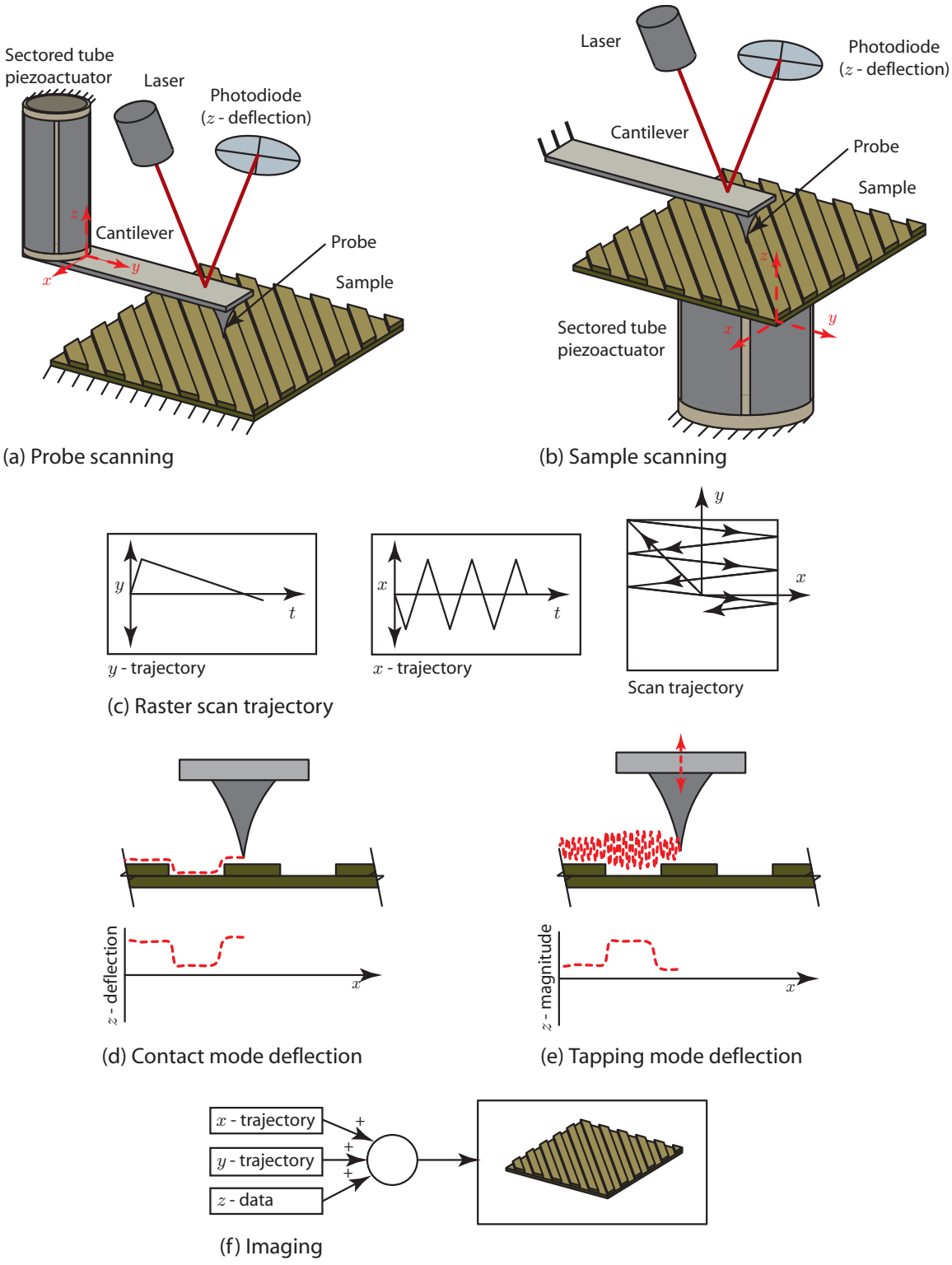

Figure 2.12: General AFM configuration.

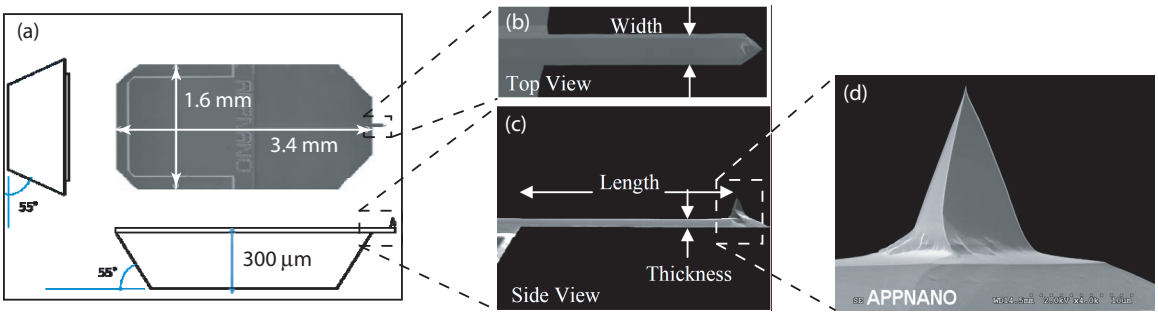

Figure 2.13: Commercial AFM cantilever produced by AppNano (www.appnano.com). (a) is a schematic showing the silicon chip that the micro-cantilever shown in (b) and (c) is attached to. (d) shows a zoomed view of the probe tip. Note: the length, width and thickness of the 300 kHz cantilever used in this thesis is approximately 125×40×4 μm respectively where the tip is 14μm high with radius <10 nm

2.4.4 Cantilevers

Because of its direct interaction with the sample surface, the AFM cantilever is the most critical system for both high-speed and high-resolution imaging. The bandwidth of the cantilever and the tip shape are both equally important. Figure 2.13 shows an AFM cantilever where (a) is a schematic showing the silicon chip that the micro-cantilever shown in (b) and (c) is attached to, and (d) shows a zoomed view of the probe tip.

High-bandwidth cantilevers are required to maintain probe to surface contact and produce high-resolution images. For example, when imaging a sample with step features in *contact mode*, the cantilever bandwidth must be high enough track the features. Likewise in *tapping mode* the mechanical resonance can be compared to the vertical sampling rate, as scan speeds increase the sampling rate must increase to maintain high resolution images. The first mechanical resonance f_1 of a fixed-free cantilever beam with no and mass is

$$f_1 = \frac{1}{2\pi}\sqrt{\frac{EI}{\rho A}}\left(\frac{1.875}{L}\right)^2 \tag{2.1}$$

where E is the elastic modulus, I is the second moment of inertia about the bending axis, ρ is density, A is the cross sectional area, and L is the length of the beam. Increasing the stiffness EI and decreasing the mass per unit length ρA as well as length L of the cantilever will increase the mechanical resonance. The maximum scan rate for a cantilever is

$$v \ll \frac{\lambda}{2}\sqrt{\frac{k+s}{m} - \frac{D^2}{2m^2}} \tag{2.2}$$

where v is the maximum achievable probe velocity, λ is the periodicy of the surface features, D is the damping, k is the spring constant, m is the effective mass of the cantilever, and S is the surface elasticity [6]. A stiff cantilever however is not ideal due to increased probe wear and sample damage. Therefore to increase the mechanical resonance while maintaining a soft spring constant, the cantilever must be short, light, and small.

2.4.5 Deflection Versus Topology Imaging

In both imaging modes, the cantilever deflection data is used to either directly produce an image called a *deflection image*, or a closed loop z-controller is used with the z-actuator to maintain constant cantilever deflection. The vertical displacement of the z-actuator is then used to produce a *topology image* (alternatively called *constant force imaging*). *Deflection imaging* is the easiest way to achieve high-speed imaging because the cantilever acts as the vertical sensor, which eliminates the need for high-speed vertical positioning. For high-speed *topology imaging*, it is essential to have a high-speed vertical positioning system to track the vertical sample features. In such systems, the vertical system must be counterbalanced with a dummy mass or be highly decoupled from the scanning system to prevent dynamic mechanical excitation.

2.5 Summary

This section introduced nanopositioning systems, piezoactuators which are the actuator of choice for high-speed positioning, compliant flexures which are used to guide motion for high-speed applications, and the AFM which is used to produce raster images with high-speed nanopositioning systems. The following section will focus on improving positioning speed through mechanical design.

Chapter 3

Mechanical Design

This chapter describes the mechanical design of the high-speed nanopositioning stage. The objective is to create a long-range linear three-axis x, y, z nanopositioning stage for high-speed AFM imaging at 30 frames per second with 100×100 pixel resolution. For raster scanning at this rate, the high-speed and low speed axis line rates are 3,000 and 30 Hz, respectively. To enable precision tracking, mechanical resonances 10 times greater than the associated line rates are desired. To limit the effects of cross-coupling, the first mechanical resonance mode of each stage body should be in its corresponding actuation direction (piston mode). The methods used to do this are described.

This chapter is organized as follows. First, serial- and parallel-kinematic stage designs are compared, followed by a brief discussion of the history of the designs in this research that lead up to the final high-speed stage. The mechanical design for high-speed positioning is described next, with details on stiffness and how the out-of-plane stiffness was increased through proper selection of piezo-stack actuators, flexure design, flexure placement, modal analysis, and the z-stage design. Finally, the fabrication an assembly of the new stage are discussed.

3.1 Serial-Kinematic Nanopositioning

The two displacement configurations for multi-degree-of-freedom motion in nanopositioning are serial-kinematic and parallel-kinematic [47]. Figure 3.1 shows the equivalent lump-parameter 3D models for both configurations as well as a hybrid configuration, where k_x, k_y, and k_z model the effective stiffness of an actuator along the x, y, and z directions, respectively. The effective damping is omitted for brevity, but in general appears in parallel with each spring element. In a full serial-kinematic design [Fig. 3.1(a)], the actuators for each degree-of-freedom are connected in series, *i.e.*, stacked on top of each other. In a full parallel-kinematic design [Fig. 3.1(b)], the actuators are connected in parallel with respect to ground and the sample platform. In a hybrid configuration such as the parallel-serial-kinematic configuration shown in Fig. 3.1(c), a parallel-kinematic configuration is used for the lateral x-, y-stage, while the vertical z-stage is configured in series with the ground [24, 33, 48].

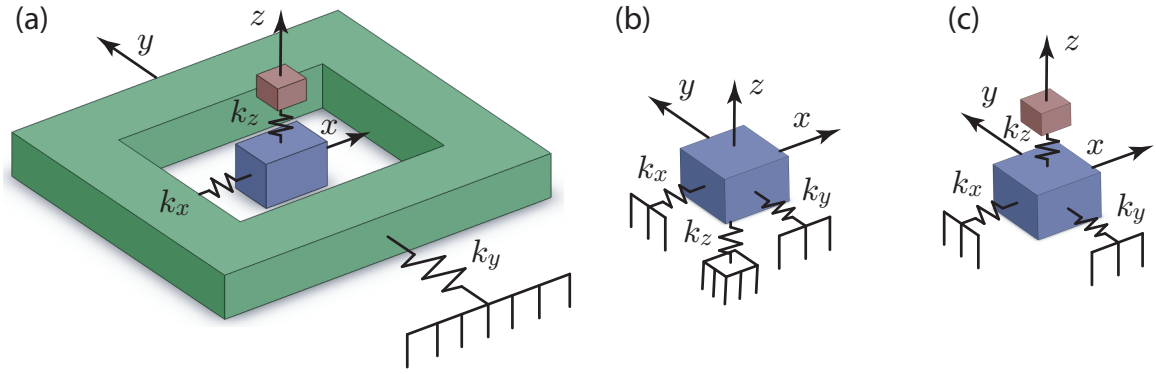

Figure 3.1: (a) Serial-kinematic xyz, (b) parallel-kinematic xyz, and (c) parallel-kinematic xy with serial-kinematic z.

The advantages of a parallel-kinematic configuration are that runout can easily be measured and corrected for, and if both lateral axes have the same mechanical bandwidth, the scan direction can be chosen arbitrarily [33]. Hybrid serial-parallel-kinematic designs are often used for x, y, z positioning [6, 24, 33, 48]. The benefit of

a hybrid design is the benefit of having two high-speed lateral axes with a decoupled z-stage for higher speed vertical tracking.

For raster-type scanning, one lateral stage moves considerably faster than the other. For example, to acquire an $n \times n$-pixels image in SPM, motion along one lateral axis is n-times faster than the other axis. For this reason, a serial-kinematic design with one high-speed stage is sufficient and may be more cost effective to design and manufacture. Particularly, only the high-speed axis will require a costly high-bandwidth, high-power piezo-amplifier. One disadvantage of this design is the inability to measure (and correct for) parasitic motion such as runout or guiding error. Therefore, it is important to design the stage with as low of runout and cross-coupling as possible. This is achievable with properly-designed flexures and mechanisms for guiding the sample stage. In fact, the serial-kinematic configuration has been exploited for developing nanopositioning stages for high-speed SPM applications [1, 9].

3.2 Design Challenges

The major challenge faced in the mechanical design of serial-kinematic stages is ensuring that the first mechanical resonance for each stage occur in the actuation direction. This is particularly challenging when designing the high-speed stage because the piezoactuator is much stiffer in actuation than it is out-of-plane, for example bending and fixed/guided deflection.

While scanning at low speed, parasitic motion of the sample platform can be minimized using a simple beam flexure to guide the motion of the platform [1]. As the actuation frequency increases, both in- and out-of-plane resonant modes can be excited due to lack of stiffness along the out-of-plane directions, thus limiting the positioning speed. However, dominant resonances occurring in the actuation direction are tolerable compared to out-of-plane modes; preferably, if the actuation modes

precede the out-of-plane or off-axis modes. Figure 3.2 shows the FEA modal analysis of an xz-stage configuration with two flexures aligned along the center of the x-stage. In this particular design, the out of plane modes of the x-stage body, rotation about the y axis θ_y and vertical z trampolining occur before the actuation mode along the x-axis. Additionally, the z-piezoactuator has a tendency to bend about the y-axis during the x actuation mode causing the sample platform to rock. This is undesirable because the rocking of the sample platform causes the fore and aft sample surfaces to travel vertically as well.

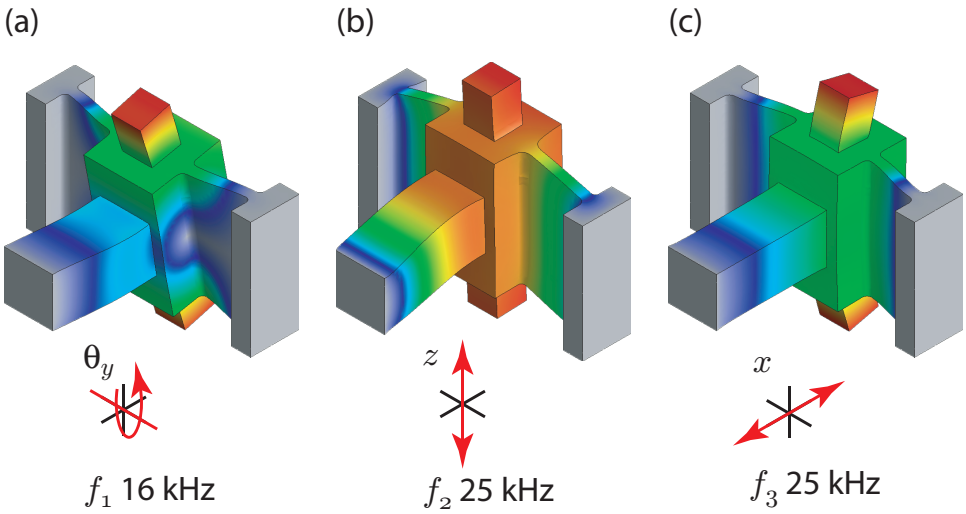

Figure 3.2: FEA modal analysis of x-, z-stage with out-of-plane resonance modes (a) and (b) occurring before the actuation mode (c).

To ensure that the actuation mode precedes out-of-plane modes, the compliant flexures are designed to have high out-of-plane stiffness, while being sufficiently *soft* to avoid affecting the achievable stroke of the piezoactuator [7, 48, 49]. It is pointed out that by using stiff and compact piezoactuators, high mechanical resonances can be achieved, but the cost is reduction in range. The cross-sectional area of the piezo-stack actuators can also be increased to improve mechanical stiffness, but doing so will increase the overall capacitance of the piezoactuator, and thus increase the required power to drive the actuator at high speed. The most practical approach is to focus

on improving the design of the flexures which guide the motion of the sample stage as discussed below.

3.2.1 Design History

A first-generation serial-kinematic two-axis nanopositioner based on simple beam flexures and consisting of multiple parts and assembled using fasteners is shown in Fig. 3.3 [1]. The high-bandwidth x-axis is nested within the low-speed y-axis. The measured first resonances in the x- and y-axes are 29 kHz and 1.5 kHz, respectively [1]. Since the stage consisted of many parts assembled together to create the complete system, slight misalignment during assembly caused incorrect preload on the flexures and the piezoactuator. And thus, the stage's dynamic response was sensitive to the assembly process and variations in the mounting and boundary conditions.

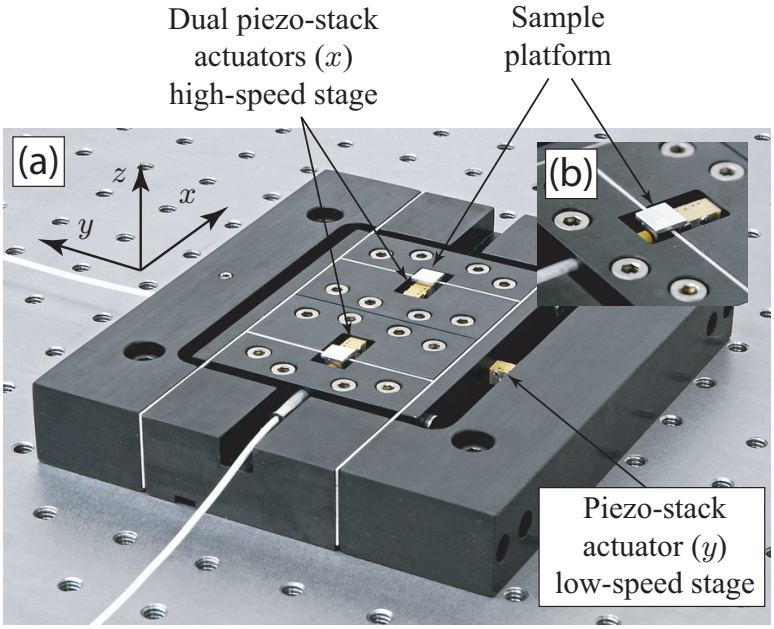

Figure 3.3: First-generation two-axis serial-kinematic high-speed scanner: high-speed stage (x) is nested inside of the low-speed stage (y). Inset: A close-up view of sample platform and x-axis piezo-stack actuator [1].

An improvement to the first-generation design is shown in Fig. 3.4. For better repeatability, the stage body is manufactured from 7075 aluminum using the wire EDM process to create a monolithic design. Positioning of the sample in the vertical direction is achieved using a piezo-stack actuator embedded into the x-positioning stage. The dominant resonances in the x and y axes are measured at 10 kHz and 2.4 kHz, respectively. The problems with this initial design were that high-speed stage flexures were incorrectly designed resulting in low actuation stiffness and low out of plane stiffness, and the stage had high lateral and rotational inertia values, resulting in poor dynamic response.

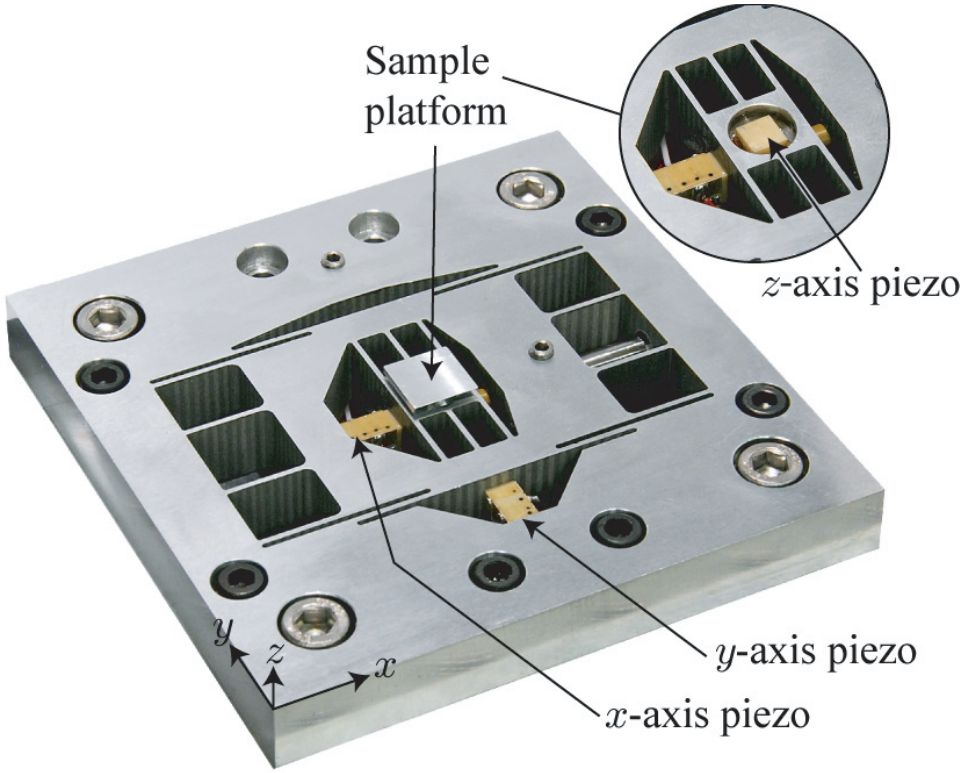

Figure 3.4: Second-generation three-axis serial-kinematic stage.

To take advantage of the monolithic design and further increase the mechanical bandwidth, a new serial-kinematic nanopositioning stage is proposed. This new design incorporates compliant flexures with improved vertical-stiffness to minimize

out-of-plane motion. Also, strategically-placed flexures minimize the sample platform's tendency to rotate ($\theta_x,\ \theta_y,\ \theta_z$) at high frequencies. The stage is designed to ensure that the first resonance in all three axes are axial (piston) modes, rather than off-axis modes which can severely limit scan speed. A functioning prototype is shown in Fig. 3.5, and the details of the design, performance, and application in AFM imaging are described next.

3.3 High-Performance Mechanical Design

3.3.1 Mechanical Stiffness

For translational motion the single degree of freedom mechanical resonance u_i ($i = x,\ y,\ z$) is

$$f_{u_i,0} = \frac{1}{2\pi}\sqrt{\frac{k_i}{m_i}} \tag{3.1}$$

where m_i and k_i are the effective translational mass and stiffness, respectively. Likewise for rotational motion θ_i ($i = x,\ y,\ z$), the first resonance is

$$f_{\theta_i,0} = \frac{1}{2\pi}\sqrt{\frac{k_{\theta_i}}{J_i}}, \tag{3.2}$$

where J_i and k_{θ_i} are the effective mass moment of inertia and rotational stiffness, respectively. To insure that actuation modes occur before the out-of-plane modes, the strategy taken is to design the stage geometry and flexure configuration so that the out-of-plane stiffness-to-mass ratios ($k_z/m_z,\ k_{\theta y}/J_y,\ k_{\theta z}/J_z$) are higher than the actuation stiffness-to-mass ratio k_x/m_x. Figure 3.6 shows the simplification of a high-speed x-stage into single degree-of-freedom systems to model four of the dominating resonance modes. Isometric, top, and side views of the stage are shown in Fig. 3.6(a) through (d), respectively. The top, back, and side views are broken down to show the

effective springs and masses effecting the body for actuation u_x (e), lateral u_y (f) rotational θ_z (g), rotational θ_x (h), rotational θ_y (i), and vertical u_z (j) modes (damping is ignored for convenience).

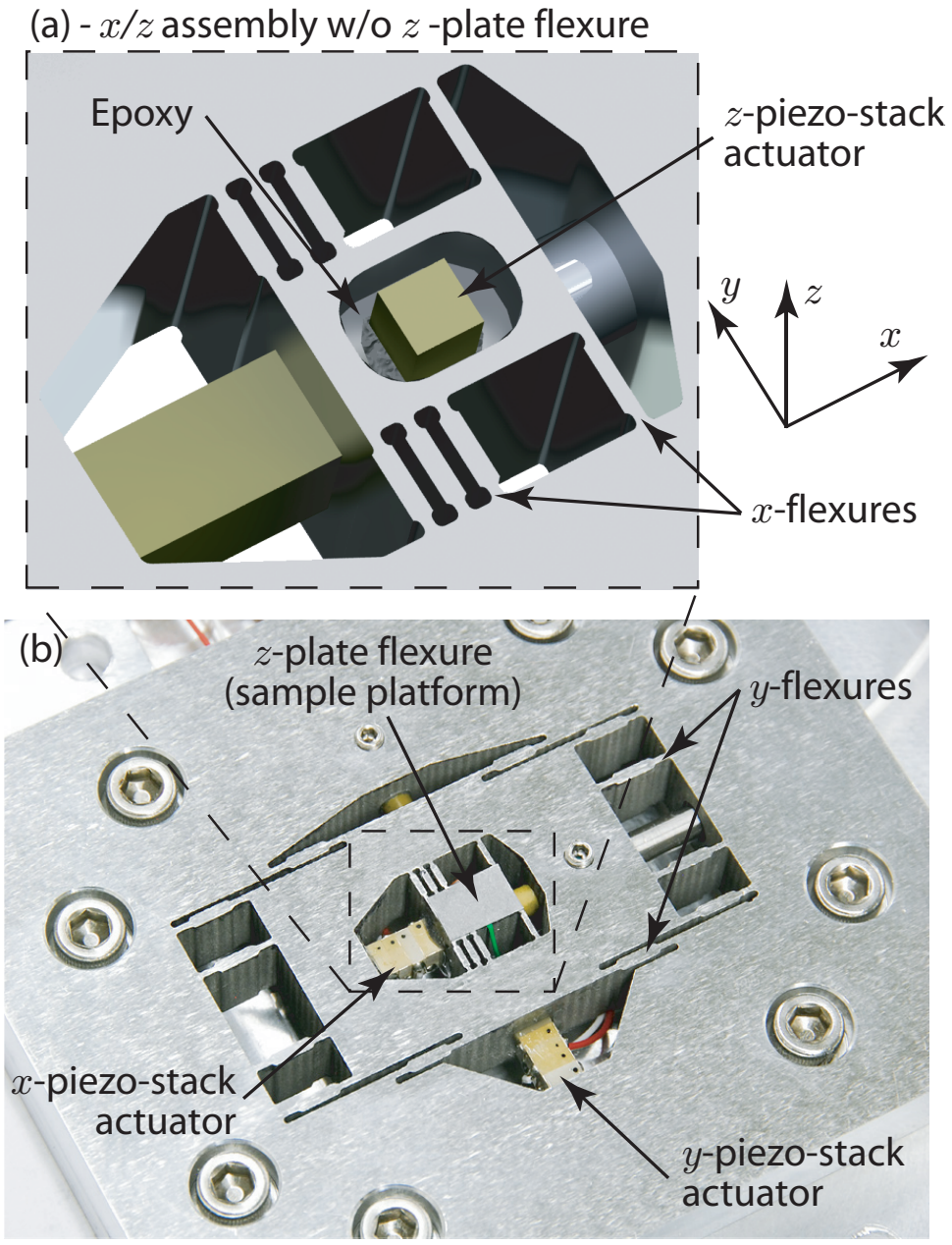

Figure 3.5: Third-generation three-axis serial-kinematic nanopositioner: (a) a zoomed-in detailed view of the z piezo-stack actuator assembly with vertically-stiffened x-flexures and (b) the full stage body with the high-speed x- and low-speed y-axis piezoactuators and vertically-stiffened flexures.

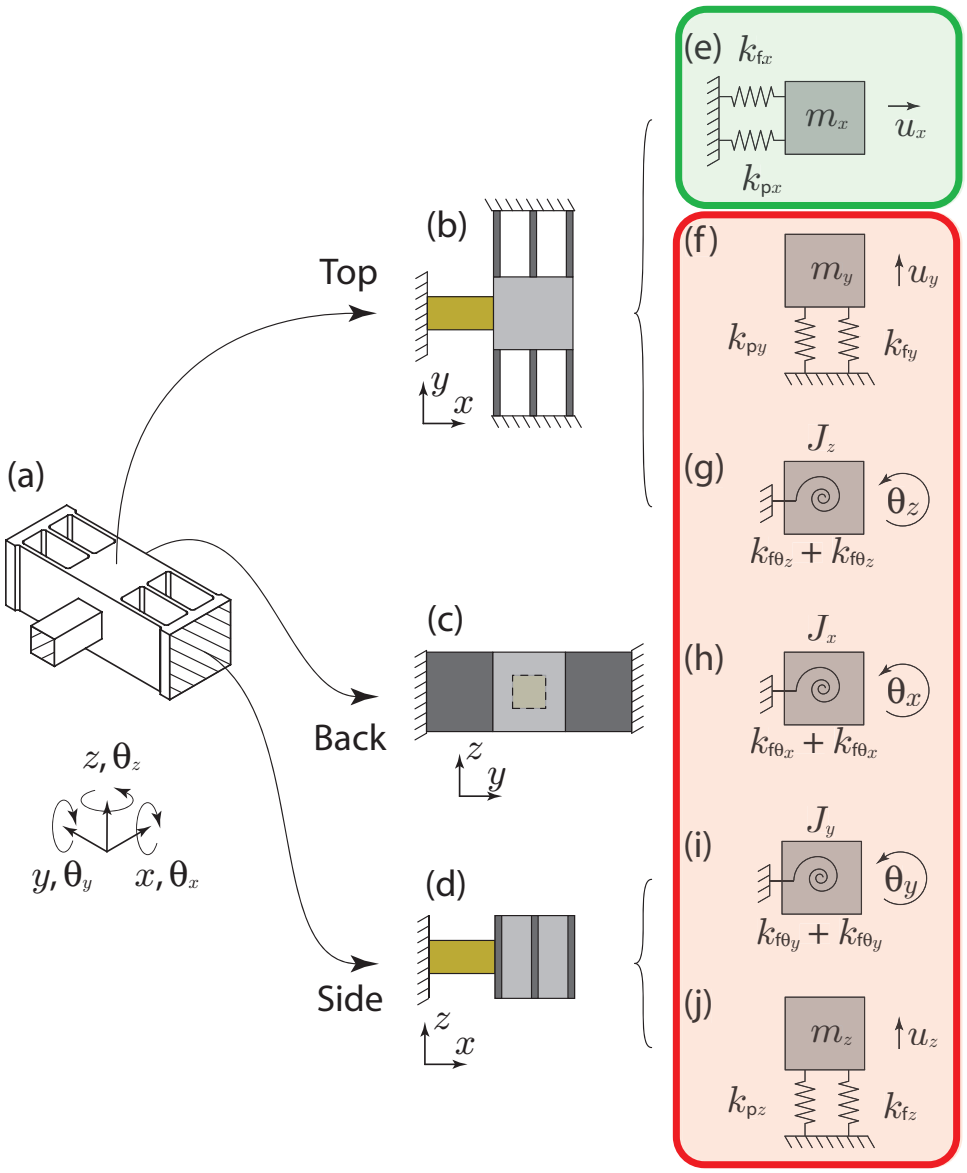

Figure 3.6: Generic high-speed stage shown in its (a) isometric, (b) top, (c) back, and (c) side views and then broken down into one-degree-of-freedom lumped parameter models (e)–(j) representing the first mechanical resonance modes for each of the six degrees of freedom. The actuation mode is represented in (e) and the five undesirable out of plane modes are represented by (f)–(j).

To satisfy the objective of having the out-of-plane modes occur beyond the actuation mode, we must increase the stiffness and decrease the inertia values associated with these modes. First of all the lateral u_y (f), rotational θ_z (g), and rotational θ_x (h) modes tend to be very high because of the high axial stiffness of the flexures. This

leaves the rotational θ_y (i), and vertical u_z (j) modes battling with the actuation u_x (e) mode. Both of these modes are highly dependant on the vertical stiffness of the flexures and piezoactuator. For this reason we focus on ways to increase the vertical flexure stiffness without increasing the actuation stiffness. Prior to this we will first address how piezoactuators are selected for the design.

3.3.2 Piezo-Stack Actuator

Piezo-stack actuators are chosen because they are compact, stiff, and have relatively high mechanical resonances. A comparison of four plate-stack piezoactuators (Noliac) of varying cross-sectional areas is shown in Table 3.1. Each actuator in this comparison is 10-mm long and meets the desired free stroke of 11 μm. (A small percentage of the free stroke will be lost due to stage stiffness and gluing the piezo-stack to the stage during assembly.) The cross-sectional dimensions (height h and width w) range from 3×3 to 10×10 mm. The capacitance increase is nearly proportional to the cross-sectional area with an average of 15.5 nF/mm^2 (for a 10-mm long piezo-stack actuator). The Young's modulus for each actuator is calculated from the blocking force and free stroke. For instance, the Young's modulus of a 5×5×10 mm piezoactuator is determined to be 33.9 GPa [1]. As shown in Table 3.1, higher actuation k_a and out-of-plane stiffness k_z can be obtained by using larger (cross section) piezo-stacks. The cost, however, is higher capacitance which increases the net power to drive the actuators, especially at high frequencies.

The stiffness in the actuation direction is maximized by using the piezoactuator in direct-drive configuration. Although mechanical displacement amplification is an affective way to increase resultant stage displacement, the added mass and reduced actuation stiffness reduces actuation resonance values [32, 34, 50]. When used in direct drive, the mechanical properties of the piezoactuator can be exploited to aid

in increasing out-of-plane resonances [9, 33].

Table 3.1: Comparison of plate-stack piezoactuators.

size (mm)	**Free stroke** (μm)	**Cap.** (nF)	k_a N/μm	k_z* N/μm	$k_z/k_a \times 100$
3x3x10	11.15	114	30.5	2.0	6.6
5x5x10	11.78	387	84.8	10.7	12.6
7x7x10	12.09	835	166.1	28.0	16.9
10x10x10	12.13	1673	339.0	69.2	20.4
* Stiffness for fixed-guided beam accounting for shear (see § 3.3.3).					

Dynamic Limitations

The first longitudinal resonant frequency (actuation mode) f_a for a fixed free beam as shown in Fig. 3.7(a) with its lumped parameter model in (b) is

$$f_a = \frac{1}{2\pi}\sqrt{\frac{k_a}{m_{eff}}} \tag{3.3}$$

where

$$m_{eff} = \frac{1}{3}htL\rho_{piezo} \tag{3.4}$$

is the effective mass, h is height, t is thickness, L is length, ρ_{piezo} is the density of the piezoactuator,

$$k_a = \frac{htE}{L} \tag{3.5}$$

is the actuation stiffness (*i.e.*longitudinal), and E is the modulus of elasticity [51]. For the case where there is no end mass as shown in (a), the first mechanical resonance in the actuation direction is

$$f_a = \frac{1}{2\pi}\sqrt{\frac{\frac{htE}{L}}{\frac{1}{3}htL\rho_{piezo}}} \tag{3.6}$$

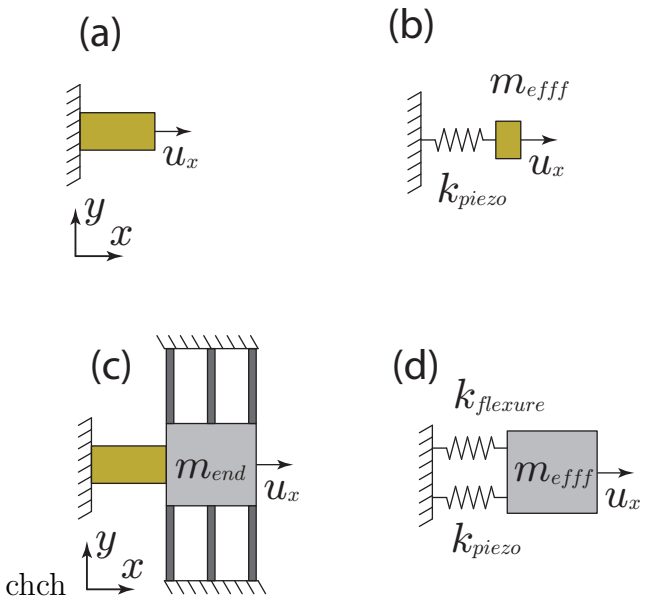

Figure 3.7: Top view of (a) piezoactuator and (c) piezoactuator with end mass and flexures broken down into lumped parameter models (b) and (d).

which simplifies to

$$f_a = \frac{1}{2\pi L}\sqrt{\frac{3E}{\rho_{piezo}}} \propto \frac{1}{L}. \tag{3.7}$$

Substituting in E and ρ yields

$$f_a = 567.46L^{-1} \tag{3.8}$$

where f_a is in Hz and L is in meters. Typically piezoactuators produce approximately 1 μm of displacement range R in μm for every 1 mm of length giving the maximum frequency for a given range to be

$$f_a = 567,460R^{-1} \tag{3.9}$$

and likewise

$$R = 567,460f_a^{-1}. \tag{3.10}$$

This means that for a fixed-free piezoactuator with no end mass, the maximum actuation frequency is inversely proportional to the desired range.

In the high-speed stage though, there is an added end mass and flexures are used to guide the displacement and the fixed-free piezoactuator in Fig. 3.7(a) takes the form of the model in (c). For this model, the effective mass is now increased by the end mass m_{end} to be

$$m_{eff} = \frac{1}{3} htL\rho_{piezo} + m_{end} \tag{3.11}$$

and the actuation stiffness in creased by the actuation stiffness of the flexures. The maximum actuation frequency is now

$$f_a = \frac{1}{2\pi}\sqrt{\frac{\frac{htE}{L} + k_{flexures}}{\frac{1}{3}htL\rho_{piezo} + m_{end}}}. \tag{3.12}$$

Flexures can be used to stiffen the system in the actuation direction but, added stiffness decreases the range as a function of

$$R_f = R_0\left(\frac{k_{piezo}}{k_{piezo} + k_{flexure}}\right) \tag{3.13}$$

where R_f is the final range and R_0 is the free range of the piezoactuator [41]. For this reason, the flexures are often limited to 10% of the actuator stiffness to limit the reduction in range. By limiting the flexure actuation stiffness to 10% of the piezoactuator actuation stiffness simplifies Eq. (3.12) to

$$f_a = \frac{1}{2\pi}\sqrt{\frac{1.1\frac{htE}{L}}{\frac{1}{3}htL\rho_{piezo} + m_{end}}}. \tag{3.14}$$

The maximum actuation frequencies for the four actuators given in Table 3.1 with varying end masses are given in Table 3.2

Table 3.2: Maximum actuation frequency for plate-stack piezoactuators.

Size (mm)	Frequency (kHz) for given end mass*						
	0 g	1 g	2 g	2.5 g	3 g	4 g	5 g
3x3x10	59.6	26.2	19.5	17.6	16.2	14.2	12.7
5x5x10	59.6	37.7	29.8	27.3	25.4	22.5	20.4
7x7x10	59.6	44.8	37.4	34.9	32.8	29.6	27.1
10x10x10	59.6	50.8	45.0	42.8	40.9	37.7	35.1
*10% additional stiffness from flexures [Eq. (3.14)]. Note: a US dime weighs approximately 2.2 g.							

Although a larger piezoactuator such as a 7×7×10 mm piezo may be used to increase the actuation stiffness and mechanical resonance it increases the drive electronic requirements. Therefore a smaller piezoactuator such as a 5x5x10 mm piezo is preferred. To achieve an actuation resonance of 25 kHz, the stage must weigh 3 g or less. Because the vertical stiffness of the 5×5×10 mm actuator is 1/8th of the actuation stiffness, the flexures must be designed to increase the vertical stiffness so the actuation resonance proceeds the out-of-plane resonances.

3.3.3 Flexure Design for Lateral Positioning (x, y, z)

The vertical stiffness of the x- and y-stages is increased by (1) increasing the number of flexures, (2) utilizing shorter (effective length) flexures, and (3) converting the flexures from constant rectangular cross section beam flexures to a serial-compliant double-hinged flexure with a "rigid" center connecting link (see Fig. 3.11).

The first step taken to increase the flexure stiffness in the vertical direction is studying how the total number of flexures n used in parallel, flexure thickness t, and length L affect the vertical stiffness k_z for a given actuation stiffness k_a. This comparison is done using both analytical and finite element analysis (FEA).

The stiffness of a flexure is defined as the ratio of a load F and the resulting displacement u. The displacements and loads are: translational displacement u_i,

rotational displacement θ_i, translational force F_i acting on a point in the i direction, and moment M_i (torque T) acting about the i axis (θ_i), where $i = x, y, z$. Figure 3.8(a) illustrates the corresponding directions of the displacements and loads acting on the free end of a fixed/free cantilever beam. The in- and out-of-plane compliances for a fixed/free beam is derived using Castigliano's second theorem [43, 52, 53]. The compliance equations are then used to derive equations for the actuation and vertical stiffness k_i of a fixed/roller guided beam shown in Fig. 3.8(b) through (d). In the second-generation design (Fig. 3.4), the fillet radius is considerably smaller compared to the flexure length and therefore has minimal effect on the flexure stiffness. For this reason, to simplify the flexure stiffness equations in this initial analysis, the compliance equations are derived for a beam with a constant cross-sectional thickness.

Application of Castigliano's Second Theorem

For a fixed/free beam of rectangular cross section the total strain energy is

$$\begin{aligned} U &= U_{axial} + U_{torsion} + U_{bending} + U_{shear} \\ U &= \int_0^L \left[\frac{F^2}{2AE} + \frac{T^2}{2GJ} + \frac{M^2}{2EI} + \frac{\alpha V^2}{2GA} \right] dx. \end{aligned} \tag{3.15}$$

where L is the beam length, $A = ht$ is the cross sectional area of the beam, h is the height, t is the thickness, E is Young's modulus, $G = \frac{E}{2(1+\nu)}$ is the shear modulus, ν is Poisson's ratio, $J = ht^3 \left[\frac{1}{3} - 0.21 \frac{t}{h} \left(1 - \frac{t^4}{12h^4} \right) \right]$ is the approximate torsional moment of inertia given in [54] on pp. 401, $I = \frac{ht^3}{12}$ is the second moment of inertia about the vertical z axis, and α is a shape factor for the cross section used in the shear equation (for a rectangular cross section $\alpha = 3/2$) [53]– [55].

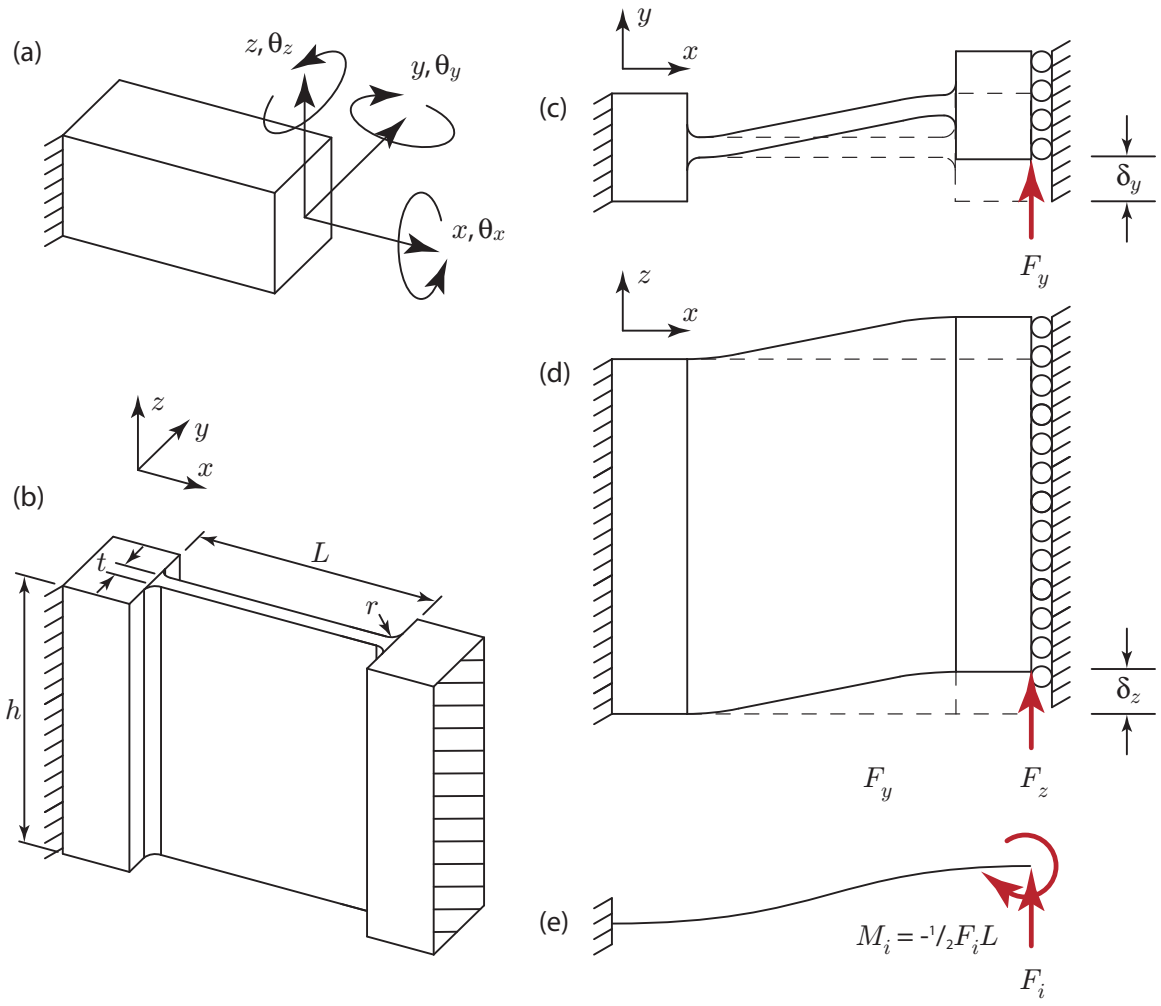

Figure 3.8: A fixed/free cantilever beam shown in (a) with the six degrees-of-freedom associated with the applied loads and displacements acting on the free end. Corner-filleted beam flexure: (b) isometric view, (c) top and (d) side views showing displacement caused by force F_i, for $i = x,\ y$, in a fixed/guided end configuration. (e) Free body diagram of the corner-filleted beam flexure illustrating the acting loads on the free end of a fixed/free beam.

Applying Castigliano's second theorem, the displacement of a point in a given direction u_i, θ_i is the partial derivative of the total strain energy with respect to the applied force, *i.e.*,

$$u_i = \frac{\partial U}{\partial F_i} \tag{3.16}$$

$$\theta_i = \frac{\partial U}{\partial M_i}. \tag{3.17}$$

From here the compliance is simply found by dividing both sides of the displacement by the applied load, *i.e.*,

$$C_{u_i,F_j} = \frac{u_i}{F_j} \tag{3.18}$$

$$C_{\theta_i\ M_j} = \frac{\theta_i}{M_j}. \tag{3.19}$$

For example, the compliance of the rectangular cross section fixed-free beam in Fig. 3.8(a) due to a point load in the y direction is found by first finding the total strain energy

$$U = \int_0^L \frac{M(x)^2}{2EI(x)}\, dx + \int_0^L \frac{\alpha V(x)^2}{2GA(x)}\, dx, \tag{3.20}$$

where $A(x)$ and $I(x)$ are constant. For simplification purposes, the coordinate system is placed on the free end of the flexure as shown in [43] where the shear is $V(x) = F_y$ and moment is $M(x) = F_y(x)$. The total strain energy for the applied load is

$$\begin{aligned} U &= \frac{F_y^2}{2EI}\int_0^L x^2\, dx + \frac{\alpha F_y^2}{2GA}\int_0^L\, dx \\ &= \frac{F_y^2 L^3}{6EI} + \frac{\alpha F_y^2 L}{2GA}. \end{aligned} \tag{3.21}$$

Therefore, the resultant displacement is

$$u_y = \frac{\partial U}{\partial F_y} = \frac{F_y L^3}{3EI} + \frac{\alpha L F_y}{GA}, \tag{3.22}$$

and the compliance is

$$C_{yy} = C_{22} = \frac{u_y}{F_y} = \frac{L^3}{3EI} + \frac{\alpha L}{GA}. \tag{3.23}$$

The compliances are then used to form the multi-dimensional compliance matrix $\mathbf{C}$ which is defined as the ratio of the displacement $\mathbf{U} = [x\ y\ \theta_z\ z\ \theta_y\ \theta_x]^T$ for a given load $\mathbf{L} = [F_x\ F_y\ M_z\ F_z\ M_y\ M_x]^T$, hence the displacement vector is

$$\begin{Bmatrix} u_x \\ u_y \\ \theta_z \\ u_z \\ \theta_y \\ \theta_x \end{Bmatrix} = \begin{bmatrix} C_{11} & 0 & 0 & 0 & 0 & 0 \\ 0 & C_{22} & C_{23} & 0 & 0 & 0 \\ 0 & C_{23} & C_{33} & 0 & 0 & 0 \\ 0 & 0 & 0 & C_{44} & C_{45} & 0 \\ 0 & 0 & 0 & C_{45} & C_{55} & 0 \\ 0 & 0 & 0 & 0 & 0 & C_{66} \end{bmatrix} \begin{Bmatrix} F_x \\ F_y \\ M_z \\ F_z \\ M_y \\ M_x \end{Bmatrix}. \tag{3.24}$$

For a constant cross section fixed/free beam the compliances are

$$\begin{aligned} C_{11} &= \frac{L}{AE} & C_{22} &= \frac{L^3}{3EI} + \frac{\alpha L}{GA} & C_{23} &= \frac{L^2}{2EI} \\ C_{33} &= \frac{L}{EI} & C_{44} &= \frac{4L^3}{Eh^3t} + \frac{\alpha L}{GA} & C_{45} &= \frac{6L^2}{Eh^3t} \\ C_{55} &= \frac{12L}{Eh^3t} & C_{66} &= \frac{L}{GJ}. \end{aligned} \tag{3.25}$$

For a long slender beam, shear strain has little effect and can therefore be ignored in C_{22}. For a short beam with a significant height-to-length aspect ratio, such as the vertical displacement of the flexure shown in Fig. 3.8(d), much of the deflection is in shear, and therefore cannot be ignored.

The displacement vector equation presented above is used to solve for the actuation stiffness k_y and vertical stiffness k_z of a fixed/guided flexure beam, *i.e.*, $F_i/u_i = k_i$. Torsional stiffness is not investigated because the θ_y rotational mode is largely dependant upon the vertical flexure stiffness when the flexures are placed at the corners of the stage body as mentioned in Sec. 3.3.4. Figure 3.8(e) shows the applied load and the expected deflection curve of the flexure in both the (c) actuation direction and (d) vertical direction. The active load being applied to the flexure is the in-plane force F_i. The resultant moment $M_i = -1/(2F_iL)$ is caused by the roller-guided end constraint. Therefore, the flexure displacement in the actuation direction u_y due to the applied force F_y and moment $M_z = -1/(2F_yL)$ is

$$\begin{aligned} u_y &= C_{22}F_y + C_{23}M_z = C_{22}F_y - C_{23}F_yL/2 \\ &= F_y\left[\frac{L^3}{3EI} + \frac{\alpha L}{Ght} - \frac{L}{2}\frac{L^2}{2EI}\right], \end{aligned} \tag{3.26}$$

where the compliances C_{ij} are given in (3.25). Taking the ratio of the applied load to the displacement, the actuation stiffness (neglecting shear) is

$$k_y = \frac{F_y}{y} = \left[\frac{L^3}{12EI} + \frac{\alpha L}{Ght}\right]^{-1} \cong \frac{12EI}{L^3}. \tag{3.27}$$

This result matches the fixed-guided Euler-Bernoulli beam equation in [53]. Using the same method, the displacement of the flexure in the vertical direction u_z is

$$\begin{aligned} u_z &= C_{44}F_z + C_{45}M_z = C_{44}F_z - C_{45}F_zL/2 \\ &= F_z\left[\frac{4L^3}{Eh^3t} + \frac{\alpha L}{Ght} - \frac{L}{2}\frac{6L^2}{Eh^3t}\right]. \end{aligned} \tag{3.28}$$

Similarly, the vertical stiffness is

$$k_z = \left[\frac{L^3}{Eh^3t} + \frac{\alpha L}{Ght}\right]^{-1}. \tag{3.29}$$

Because of the high aspect ratio in the vertical direction, shear cannot be ignored.

Equations (3.27) and (3.29) are used to study the effect of the quantity of flexures n and flexure thickness t on the effective vertical out-of-plane stiffness $k_{z\ eff}$. To do this, a given effective actuation stiffness $k_{y\ eff} = 10$ N/μm was divided by the number of flexures n to give the actuation stiffness for an individual flexure $k_{y\ i}$. Equation (3.27) is then used to calculate the length L of the individual flexure for a given thickness (0.3 to 1-mm thick). The individual vertical stiffness $k_{z\ i}$ is then calculated using Eq. (3.29). The individual vertical stiffness is multiplied by the quantity of flexures n to give the effective vertical stiffness. By increasing the number of flexures from 2 to 12 (1-mm thick) the vertical stiffness is increased from 76 to 226 N/μm, resulting in 197% increase. For $n = 2$, decreasing the flexure thickness from 1 to 0.3-mm thick (which effectively decreases the flexure length) increased the vertical stiffness from 76 to 79.5 N/μm (4.6% increase). Increasing the number of flexures from 2 to 12 and decreasing the flexure thickness from 1 to 0.3-mm thick produces a vertical stiffness of 260 N/μm (242% increase). In Fig. 3.9, the circles denote the $k_{z\ eff}$ values obtained using FEA. The FEA results follow the trend of the analytical results with the only variance being an increase in effective stiffness (average increase = 27%). Increasing flexure height h also contributes to increasing vertical stiffness but at the cost of a taller stage body, which increases the mass m and rotational inertia J, thus reducing the actuation resonance.

Summary of the Effects of Quantity of Flexures and Thickness

The most dramatic increase in vertical stiffness for a beam flexure is observed by increasing the number of flexures n. Further increases are observed by decreasing the flexure thickness (and as a result the flexure length). But the limiting factor of decreasing the flexure thickness is stress. A shorter thinner beam flexure will have higher stress concentration than a longer thicker beam flexure of equal stiffness.

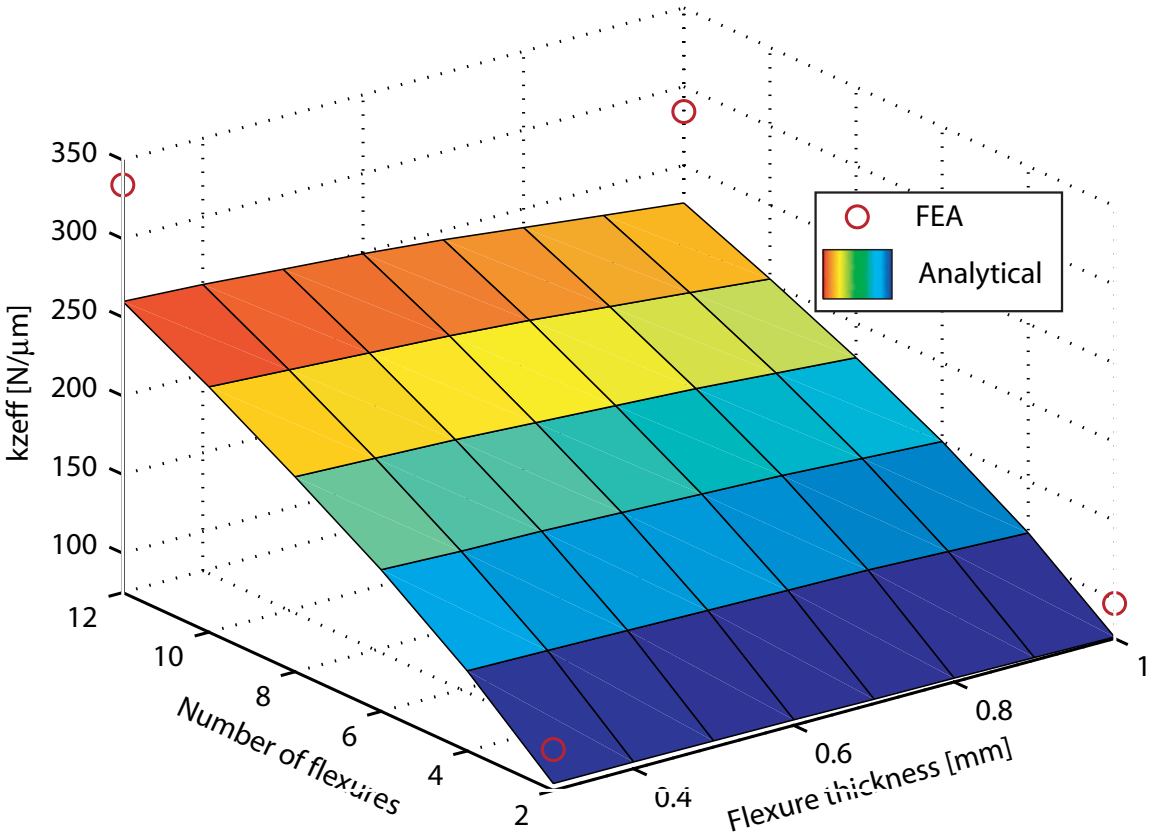

Figure 3.9: FEA and numerical analysis results showing effective vertical flexure stiffness $k_{z\ eff}$ with respect to flexure thickness t and quantity of flexures n. Effective actuation stiffness $k_{y\ eff}$ is held constant at 10 N/μm.

Thickened Beam Flexure

When a corner-filleted beam flexure, as studied above, is displaced in the actuation direction [Fig. 3.10(a2)], the majority of the strain (and stress) is located at the flexure ends near the fillets. Additionally, when the same flexure is displaced in the vertical direction [Fig. 3.10(a3)], the majority of the vertical displacement is in shear strain located at the center cross section. An effective way to further increase the out-of-plane stiffness of a beam flexure is to increase the thickness of the center section of the flexure, thus converting the beam flexure into a double-hinged serial flexure as shown in Fig. 3.11(b). Figure 3.10(a3) shows how the vertical stiffness is increased by thickening the center section of the beam flexure to decrease the shear stress. Both analytical and FEA methods are used to study the vertical stiffness of the 'thickened' flexures. For the analytical analysis, the cross sectional area and second moment of inertia values in Eq. (3.20) are replaced with $A(x) = ht(x)$ and $I(x) = ht(x)^3$, respectively.

For example, the thickness of the flexure in Fig. 3.11(b) is

$$t(x) = \begin{cases} t + 2\left[r - \sqrt{x(2r-x)}\right] & , x \in [0, r] \\ t & , x \in [r, l-r] \\ t + 2\left[r - \sqrt{(l-x)(2r-l+x)}\right] & , x \in [l-r, l] \\ t + 2r & , x \in [l, L-l] \\ t + 2\left[r - \sqrt{(l-(L-x))(2r-l+L-x)}\right] & , x \in [L-l, L-l+r] \\ t & , x \in [L-l+r, L-r] \\ t + 2\left[r - \sqrt{(L-x)(2r-(L-x))}\right] & , x \in [L-r, L] \end{cases} \tag{3.30}$$

where t and l are thickness and length of the thin section of the flexure, r is the fillet radius, $t + 2r = T$ is the thickness of the thickened section, and L is the length of the entire flexure. For this case, the compliance is derived by first solving for the total

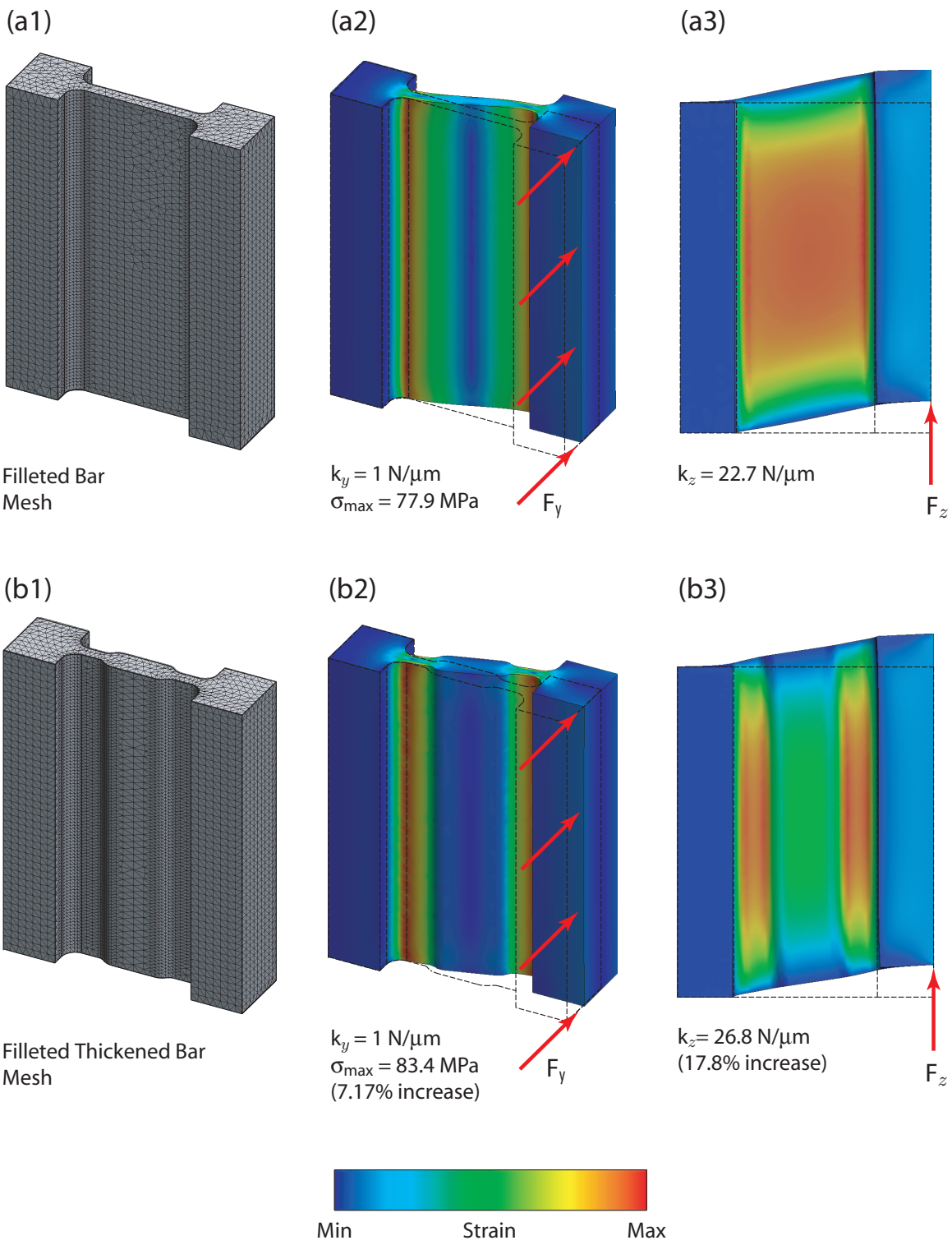

Figure 3.10: FEA analysis of corner filleted beam flexure and a thickened filleted beam flexure (corner-filleted serial-compliant flexure).

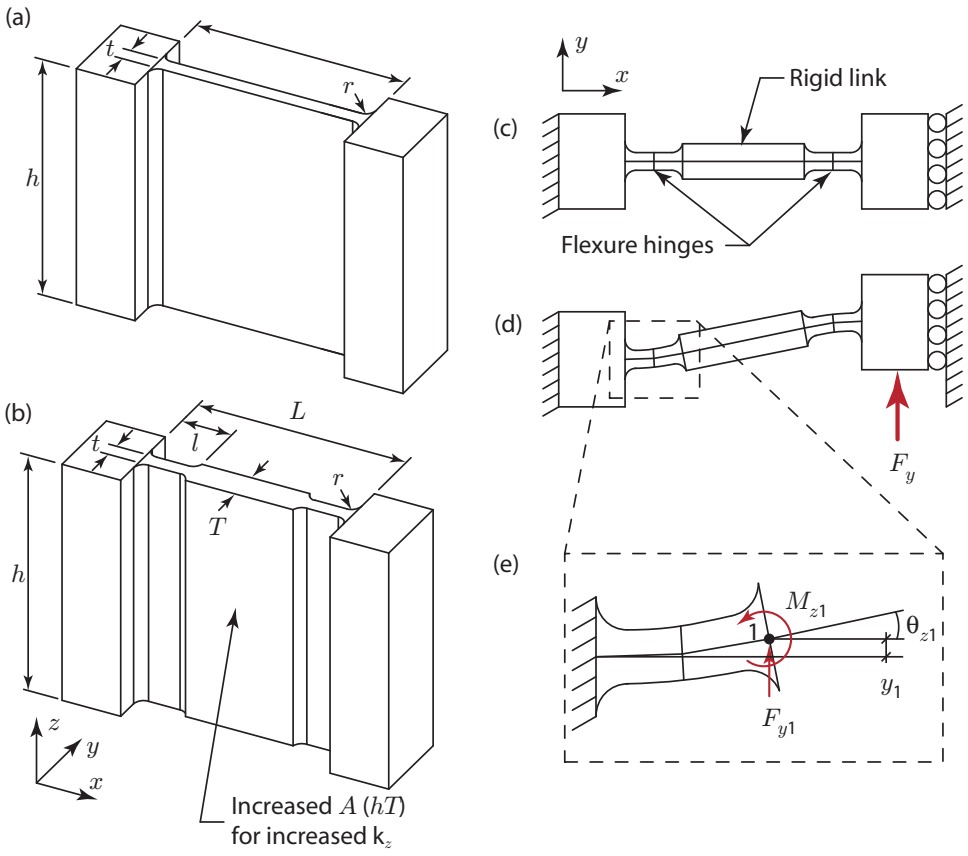

Figure 3.11: Beam flexure design: (a) trimetric view of constant cross section corner-filleted flexure beam, (b) trimetric view of corner-filleted serial-compliant flexure, (c) top view, (d) top view with applied load, and (e) expanded view of corner-filleted flexure hinge.

strain energy [Eq. (3.20)] while using the thickness function $t(x)$ in the area $A(x)$ and second moment of inertia $I(x)$ expressions. Again, the coordinate system is placed on the free end for simplification and to allow for direct integration as shown in [43]. The applied shear is $V(x) = F_y$ and the moment is $M(x) = F_y x$. The total strain energy for bending due to a point load is

$$\begin{aligned} U &= \int_0^L \frac{M(x)^2}{2E\frac{ht(x)^3}{12}}\,dx + \int_0^L \frac{\alpha V(x)^2}{2Ght(x)}\,dx \\ &= \frac{12F_y^2}{2Eh}\int_0^L \frac{x^2}{t(x)^3}\,dx + \frac{\alpha F_y^2}{2Gh}\int_0^L \frac{1}{t(x)}\,dx. \end{aligned} \tag{3.31}$$

Taking the partial derivative with respect to the applied force F_y gives the displacement

$$u_y = \frac{\partial U}{\partial F_y} = \frac{12F_y}{Eh}\int_0^L \frac{x^2}{t(x)^3}\,dx + \frac{\alpha F_y}{Gh}\int_0^L \frac{1}{t(x)}\,dx. \tag{3.32}$$

The in-plane (and out-of-plane) stiffness is then calculated numerically by taking the ratio of the force to deflection.

Table 3.3 compares the actuation and vertical stiffness of a standard filleted flexure beam to a thickened flexure beam obtained through Eq. (3.32) and FEA. This comparison shows how the vertical stiffness of beam flexures similar to the ones used on the y stage can be increased an additional 20% by increasing the thickness of the center section. To keep the actuation stiffness $k_{y\ eff}$ constant, the length L of the thickened flexure is increased from 9.75 mm to 10.70 mm.

Table 3.3: y-axis flexure stiffness comparison.

Type	$k_{y\ eff}$ $(N/\mu m)$		$k_{z\ eff}$ $(N/\mu m)$	
	Analytical	**FEA**	**Analytical**	**FEA**
Filleted beam	5.82	6.00	196.6	213.9
Thickened center	5.84	5.32	237.6	238.2

In summary, the effective vertical stiffness can be improved to increase the out-of-plane stiffness by:

1. increasing the number of flexures n,
2. decreasing the flexure length L, and
3. thickening the center section of a beam flexure to create a serial-compliant double-hinged flexure.

3.3.4 Flexure Placement to Minimize Rotation

Flexure placement is important to help increase rotational stiffness. Increasing the length (and width) of a stage and placing flexures at the corners of the moving platform increase rotational stiffness of the platform. However, the cost of increasing the size of the platform is increasing overall mass, thus lowering the mechanical resonance. The highest resonance values are achieved with high stiffness-to-mass/inertia ratios.

3.3.5 Stress Stiffening

When single beam flexures [Fig. 3.12(a)] are used symmetrically about the drive axis such as in the x and y stage [Fig. 3.12(b)], large displacements will cause stress stiffening and therefore restrict range of motion [56, 57]. To allow for larger displacements, double beam flexures or double parallelogram flexures should be used [58,59] as shown in Fig. 3.12(c) and (d). The cost of using multiple beam flexures in series is reduced out-of-plane stiffness, which lowers mechanical resonances. Because the stages in this specific design have relatively small displacements relative to the flexure length and thickness (worst case of 10μm displacement for 7mm long 0.4mm thick flexure) stress stiffening for single beam flexures is minimal and is therefore neglected. Additionally, because the stages are being specifically designed for high mechanical resonances, out-of-plane stiffness is critical. For this reason, single beam flexures are used.

3.3.6 Modal Analysis

The first five modes for the x- y- and z-stages are predicted using the *frequency* tool in COSMOSWorks (FEA). It is assumed that the resonances of the y-stage would not be excited by the dynamic motion of the inner nested x-stage. This allows the design shown in Fig 3.13(a) to be broken down into the low-speed y-stage [Fig. 3.13(b1-b5)], high-speed x-stage [Fig. 3.13(c1-c5)], and vertical z-stage [Fig. 3.13(d1-d5)]. The

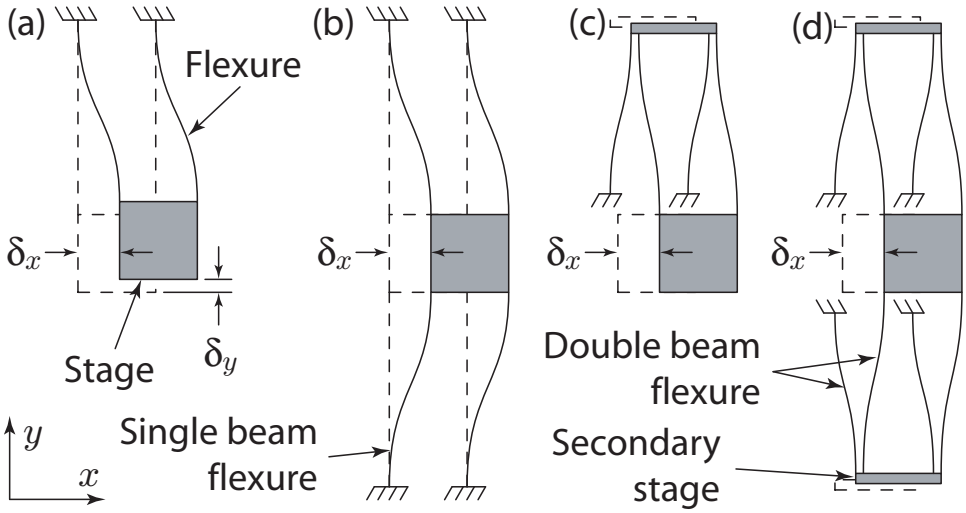

Figure 3.12: Flexure-guided stages: guided by (a) two single-beam flexures on one side of drive axis, (b) four single-beam flexures symmetric about drive axis, (c) one double parallelogram flexure module, and (d) two double parallelogram flexure modules symmetric about the drive axis.

boundary faces of each stage (shown hatched) have a fixed boundary condition. All contacting components are bonded together with compatible mesh. The meshing is done at "high quality" with refined meshing at the flexure fillets and pivot points (0.25 mm minimum element size on surfaces). Table 3.4 lists the materials used and their corresponding mechanical properties. The predicted first mechanical resonance for the y-, x-, and z-stage are 5.96 kHz, 25.9 kHz, and 113 kHz, respectively, all of which are in the corresponding stage actuation direction as preferred.

Table 3.4: Material properties.

Material	E (GPa)	ν	ρ (Kg/m^3)
Aluminum	72	0.33	2700
Steel	200	0.28	7800
PZT	33.9*	0.30	8000
Alumina	300	0.21	3960
* Calculated from stiffness and blocking force.			

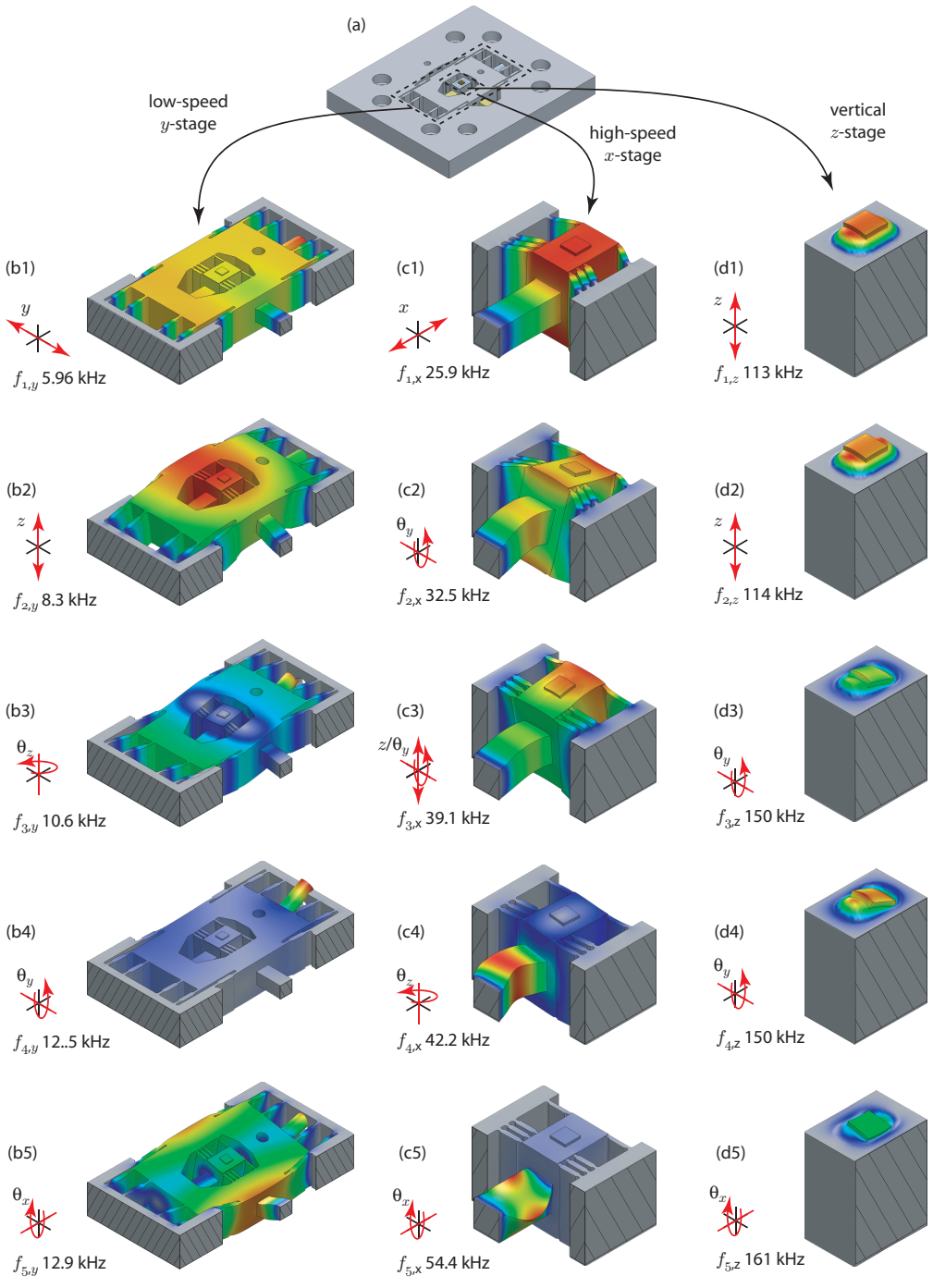

Figure 3.13: Finite element analysis results showing first five modes: (a) high-speed scanning stage; (b1)-(b5) modes for low-speed y-stage; (c1)-(c5) modes for high-speed x-stage; and (d1)-(d5)modes for vertical z-stage. Each stage section is designed to have the first mechanical resonance to occur in the actuation direction.

Simulated FEA frequency response is done using the *Linear Dynamic (Harmonic)* tool in COSMOSWorks for the x- and y-stages. A constant amplitude sinusoidal force is applied in the actuation direction at the corners of the piezoactuator/stage interfaces. A global modal damping ratio of 0.025 is applied to mimic the damping of aluminum alloy. Figures 3.14(a) and (b) show the predicted frequency response plots for the x- and y-axes with the resonant peaks occurring at 25.9 kHz and 5.96 kHz respectively.

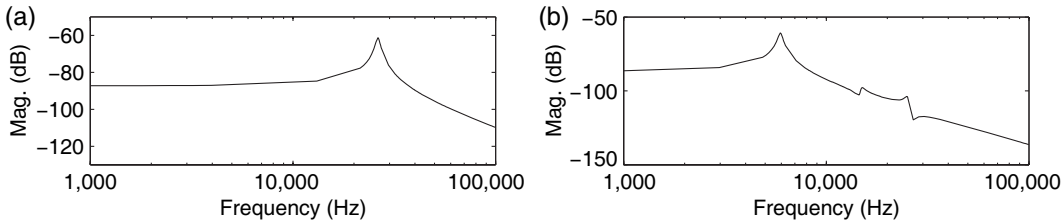

Figure 3.14: FEA predicted frequency response plots for the (a) high-speed x-axis and (b) low-speed y-axis.

3.3.7 z-Stage Design

The quick movements of the z-stage when tracking sample features such as steps, may excite the resonance modes of the nesting x-stage. To minimize impulsive forces along the vertical direction, a dual counterbalance configuration is utilized. Ando *et al.* [9] describe four configurations which include face mounting, mounting both faces of the actuator to flexures, and inserting the piezoactuator in a hole and allowing the end faces to be free. Dual face-mounted z-piezoactuators are a simple and effective method for counterbalancing. However, the disadvantage with this setup is the first resonance mode for a slender piezoactuator is bending as shown in Fig. 3.15(a1), instead of the desired actuation mode as illustrated in Fig. 3.15(a2). Inserting the piezoactuator into a hole in the x-stage is tested in the Generation 2 design shown in Fig. 3.4. Unfortunately, the design requires a long piezoactuator and did not constrain

the end faces well.

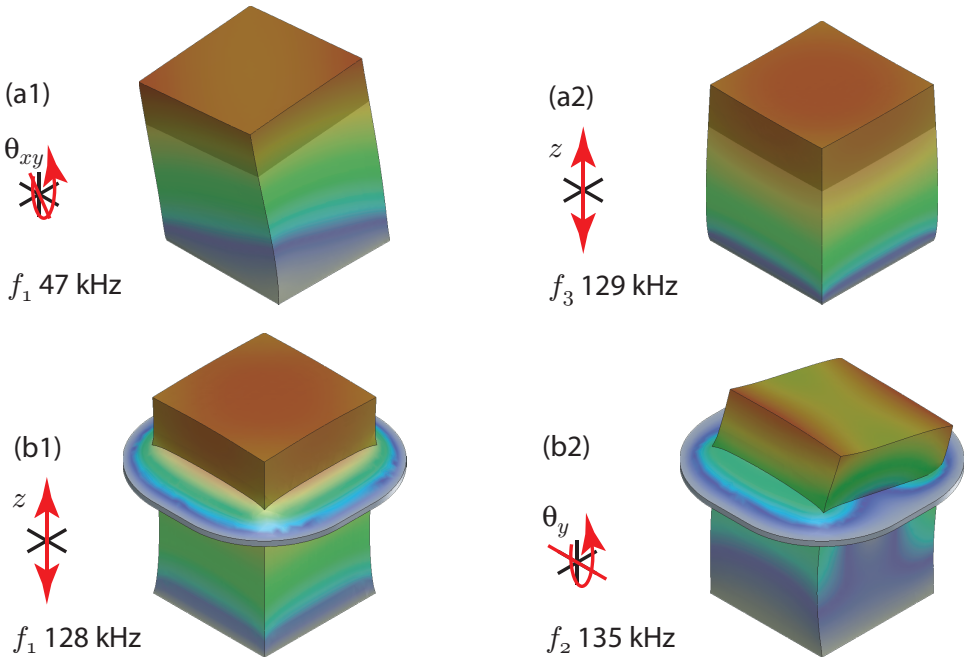

Figure 3.15: Vertical z-piezoactuator with 1 mm thick sample shown with and without plate flexure.

A new alternative is proposed in which a dual face mounted piezo configuration is combined with a compliant end plate flexure. The piezoactuators are first recessed within the nesting stage so that the free face is flush with the top surface of the nesting stage. The plate flexure is glued to the free end of the piezoactuator and the surrounding surface of the stage. Figures 3.15(b1)-(b2) show how by using a plate flexure, the bending (and torsional) modes can be shifted beyond the actuation mode.

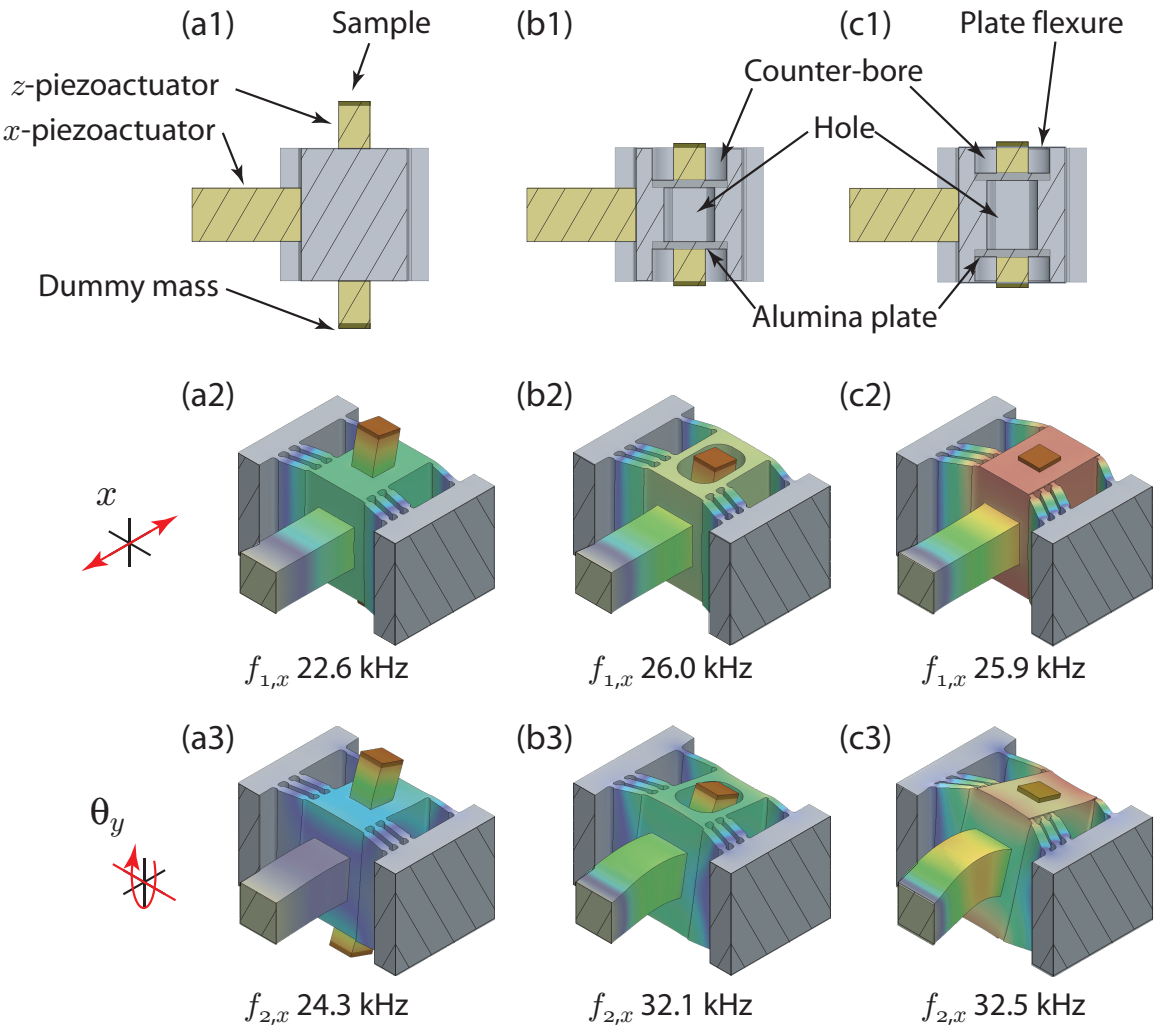

Figure 3.16: Three configurations for the z-piezoactuator and corresponding first two resonance modes. The dynamic characteristics of the face-mounted configuration in (a) are improved by recessing the z-piezoactuator into the x-stage body (b), and adding a plate flexure to the free face z-piezoactuator (c).

3.4 Fabrication and Assembly

The final experimental prototype is shown in Fig. 3.17 with the scanner body bolted to an aluminum base. To reduce mass, the 5×5×0.45 mm sample (Mikromasch TGZ01) is cut to 3×3 mm and is glued directly to the sample platform [shown in Fig. 3.17(a)]. Countersinks are milled into the scanner body and base to hold the AFM head (Nanosurf, easyScan 2) in place [Fig. 3.17(b)].

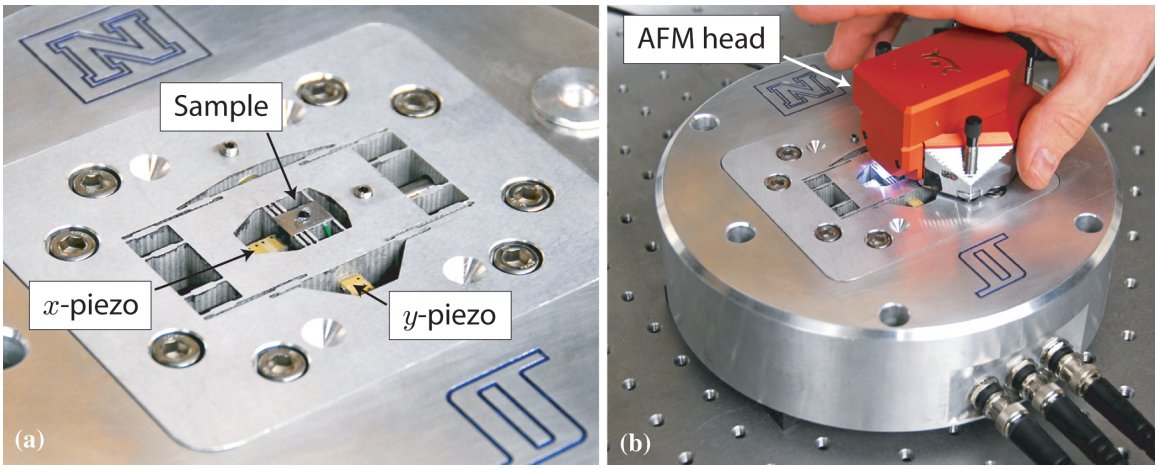

Figure 3.17: Final experimental prototype: (a) stage with sample glued to sample platform and (b) an AFM head [Nanosurf easyScan 2 AFM, Nanoscience Instruments, Inc. (www.nanoscience.com)] coupled with the positioning stage for high-speed AFM imaging experiments.

The main stage body is constructed from a single block of 7075 aluminum alloy, where the features are machined using traditional milling and wire EDM process. The x- and y-stages are displaced with 5×5×10 mm Noliac SCMAP07 piezo-stack actuators (Sec. 3.3.2) and are guided in the axial direction with compliant, center-thickened flexures described above (Sec. 3.3.3). Flexure thickness tolerances are critical for obtaining desired effective actuation stiffness. The x-flexures are designed to have a pivot point thickness of 0.5±0.03-mm to produce an effective axial stiffness of 14±2-N/μm.

When assembling the x- and y-stages, it is important to preload the piezoactuators. Failure to preload will result in lower mechanical resonances that resemble the predicted free stage resonance (stage without piezoactuator). Preloading is accomplished by initially displacing the stages in the actuation direction and sliding the piezoactuators in place with shims and glue. The tension on the stage is then released onto the piezoactuator resulting in preload.

The dual sample platforms are displaced in the z-axis using two 3×3 mm Noliac SCMAP06 piezo-stack actuators. The actuators are recessed within the nested x-stage. The base of each actuator is glued to an alumina plate while the free end is constrained using plate flexures. To increase the stiffness of the piezoactuators, the plate-stacks are used without the stock 1 mm thick ceramic insulating end-plates. Instead, the mounting face is insulated by the alumina base plate, while the top surface is insulated from the plate flexure with a thin sheet of mica.

Chapter 4

Drive Electronics and Position Sensing

The power amplifier and position sensors directly effect the systems response and positioning/tracking accuracy. Figure 4.1(a) shows a block diagram representation of the system where $r(s)$ is the reference input signal, $G(s)$ is the transfer function of the mechanical system, and $y(s)$ it the output signal. The system is then shown in Fig. 4.1(b) broken down into its electrical $G_E(s)$, mechanical $G_M(s)$, and sensor $G_S(s)$ subsystems where $y_E(s)$ is the output from the electrical system in volts, $y_M(s)$ is the output from the mechanical system in μm and $y(s)$ is the output from the sensor in volts. The electrical subsystem directly effects the mechanical subsystem and is therefore a critical component for positioning. The sensor subsystem however does not directly effect the position of the mechanical system $y_M(s)$, rather it effects the measured position and is therefore is critical for open-loop measurement and closed-loop control. The following sections provide details of performance and limitations for the drive electronics and position sensors.

4.1 Drive Electronics

The high-speed lateral x- and vertical z-axes require drive electronics capable of supplying sufficient power to drive the capacitive piezoelectric loads at high frequencies.

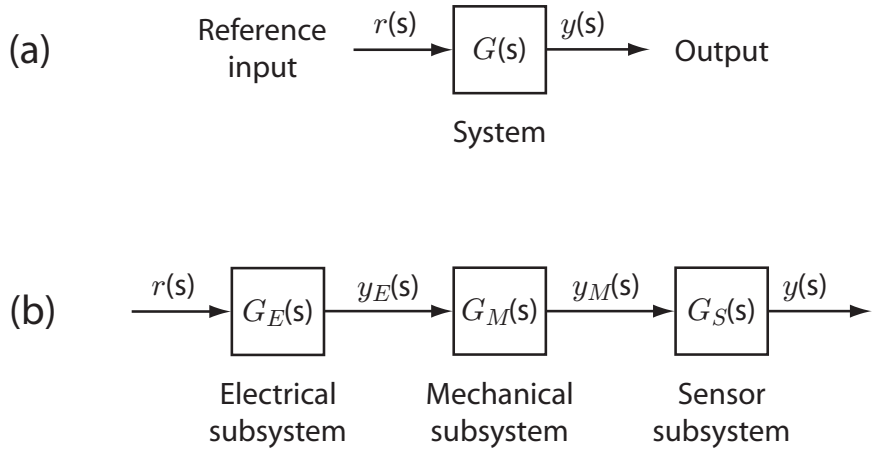

Figure 4.1: (a) Block diagram representation of system broken down into (b) a block diagram representation of the electrical, mechanical, and sensor subsystems.

A capacitor circuit symbol is shown in Fig. 4.2 showing the current $i(t)$ and voltage $v(t)$ across the capacitor. For an AC power system the voltage V_C across a capacitor

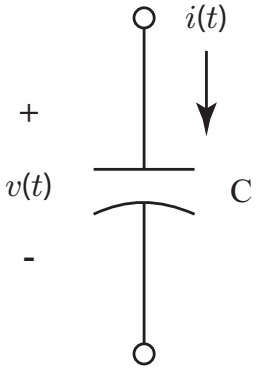

Figure 4.2: Capacitor circuit symbol showing voltage $v(t)$ and current $i(t)$.

is

$$V_C = Z_C \times I_C \tag{4.1}$$

where I_C is the current across a capacitor and Z_C is the impedance for the capacitor defined as

$$Z_C = \frac{1}{j\omega C} \tag{4.2}$$

where ω is the frequency of the input voltage in radians and C is capacitance in farads. Rearranging Equation (4.1) to

$$I_C = V_C j\omega C \tag{4.3}$$

shows that as capacitance and frequency increase, so does the required current (and power) to drive the system. The nominal capacitances for the x- and z-axis actuators are 380 and 100 nF, respectively. To drive the 380 nF piezoactuator with 200 V at 3 kHz requires 1.4 amps and 287 watts.

4.1.1 Commercially Available Power Amplifiers

A commercial power amplifier is the easiest solution for the electrical subsystem in a piezo-actuated nanopositioning system. However, the performance of commercial amplifiers may not be sufficient to drive the mechanical components. Table 4.1 lists three commercial amplifiers along with their listed performance and cost. As shown, the PiezoDrive PDL200 offers the best performance out of the three amplifiers with a maximum current range of ±600 mA and a bandwidth greater than 400 kHz. The ±600 mA voltage range however is only sufficient to drive the high-speed stage at 1,256 Hz. For this reason, a custom high-bandwidth power amplifier was developed using off the shelf components.

Table 4.1: Commercial power supplies.

Model	Voltage range	Current range	Signal bandwidth	Slew rate	Cost (USD)
Trek PZD700A	±700 V	±100 mA	125 kHz	150 V/μs	$3000-4000
Trek PZD603	0 to 250 V	±80 mA	150 kHz	100 V/μs	$3000-4000
PiezoDrive PDL200	0 to 200 V	±600 mA	¿400 kHz	N/A	$2,000

4.1.2 High-Bandwidth Power Amplifiers

The drive electronics for the high-speed stages are designed using off-the-shelf components. The piezo-amplifiers are built around the Power Amp Design (www.powerampdesign.net) PAD129 power op-amp, with a gain bandwidth product of 1 MHz. A DC power supply is constructed from two linear regulated 100 V, 3 A DC power supplies (Acopian A100HT300). The two 100 V supplies are wired in series to create a 200 V supply for the power op-amp as shown in Fig. 4.3. The power op-amp is wired as a non-inverting amplifier with a gain K of approximately 15. The gain K is a function of

$$K = \frac{V_{out}}{V_{in}} = 1 + \frac{R1}{R2} \tag{4.4}$$

where V_{in} is the input voltage or reference signal, V_{out} is the output voltage, and $R1$ and $R2$ are resistor values. A 35 kHz low pass filter is used to smooth the input signal to the power op-amp. The electrical system was assembled and mounted in an electronics rack as shown in Fig. 4.4.

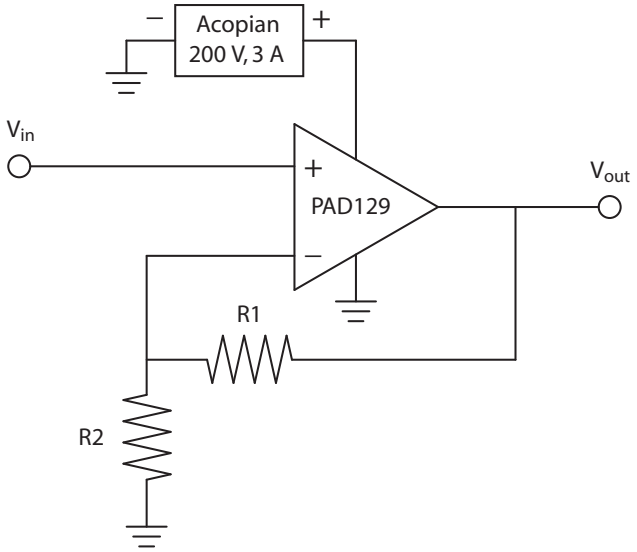

Figure 4.3: Circuit diagram for high-bandwidth power amplifier.

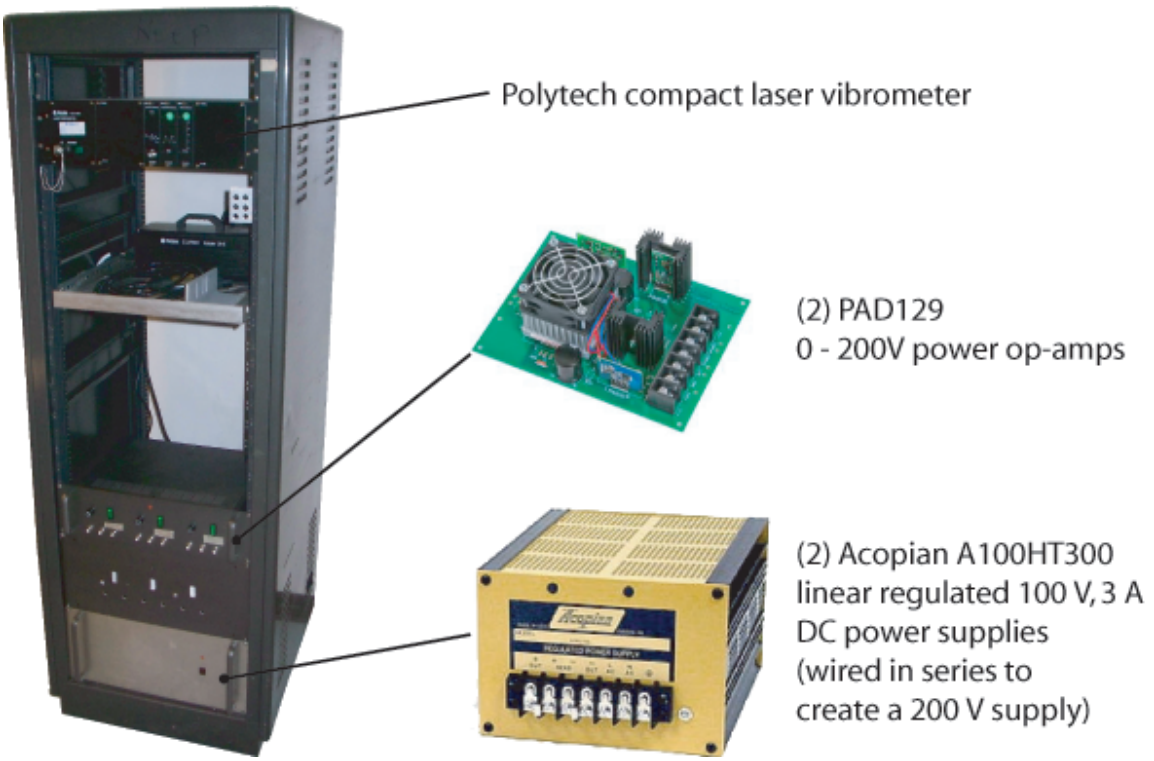

Figure 4.4: Electronics rack used to hold the Polytec compact laser vibrometer, Acopian DC power supply, and PowerAmp Design PAD129 power op-amp.

4.1.3 Amplifier Performance

The performance of the custom power amplifier was quantified and compare it to the commercially available power supplies. Sine sweep frequency response analysis was performed using a dynamic signal analyzer (DSA) (Stanford Research Systems SRT785). The block diagram for the frequency response setup is shown in Fig. 4.5. The DSA is connected to the power amplifier which is then connected to a grounded 420 nF capacitor. Note, the capacitance of the 5×5×10 mm plate-stack piezoactuator used in the x-stage is 387 nF.

The results for the frequency response analysis are shown as Bode plots in Fig. 4.6, the performance characteristics are listed in Table 4.2. The Trek PZD700 and PZD603 models perform very similar to each other in that they both have a resonance mode

around 5 kHz and a bandwidth near 9 kHz. The PiezoDrive model PDL200 performs much better with a bandwidth of 16 kHz and no noticeable resonance mode. The Acopian/PAD129 power supply however does have a resonance mode, but it occurs far beyond 100 kHz. The bandwidth for the Acopian/PAD129 system was not measurable in this analysis. In summary, for high-speed applications, the Acopian/PAD power supply is the best performing power supply available to this research. Therefore, the Acopian/PAD129 system will be used to power the high-speed x-, and z-axes while the performance of the PiezoDrive PDL200 is sufficient for the low speed y-stage.

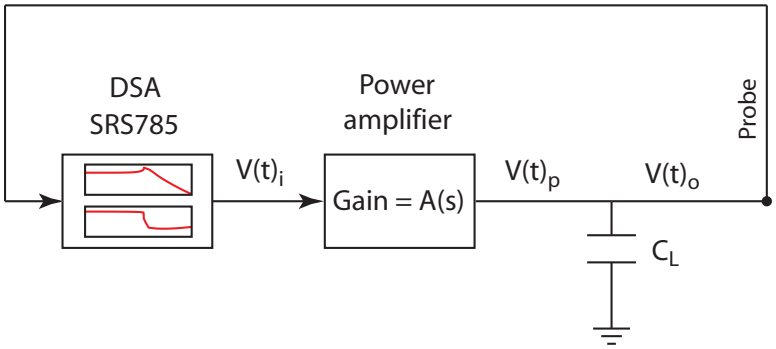

Figure 4.5: Block diagram for power supply frequency response analysis.

Table 4.2: Power amplifier characteristics.

Model	M_O (dB)	M_{BW} (dB)	Bandwidth kHz	Resonance kHz
Trek PZD700	25.89	22.89	8.7	5.26
Trek PZD603	27.96	24.96	9.8	4.5
PiezoDrive PDL200	26.04	23.04	16	N/A
Acopian/PAD129	23.54	20.54	$\gg$ 100 kHz	$\gg$ 100 kHz

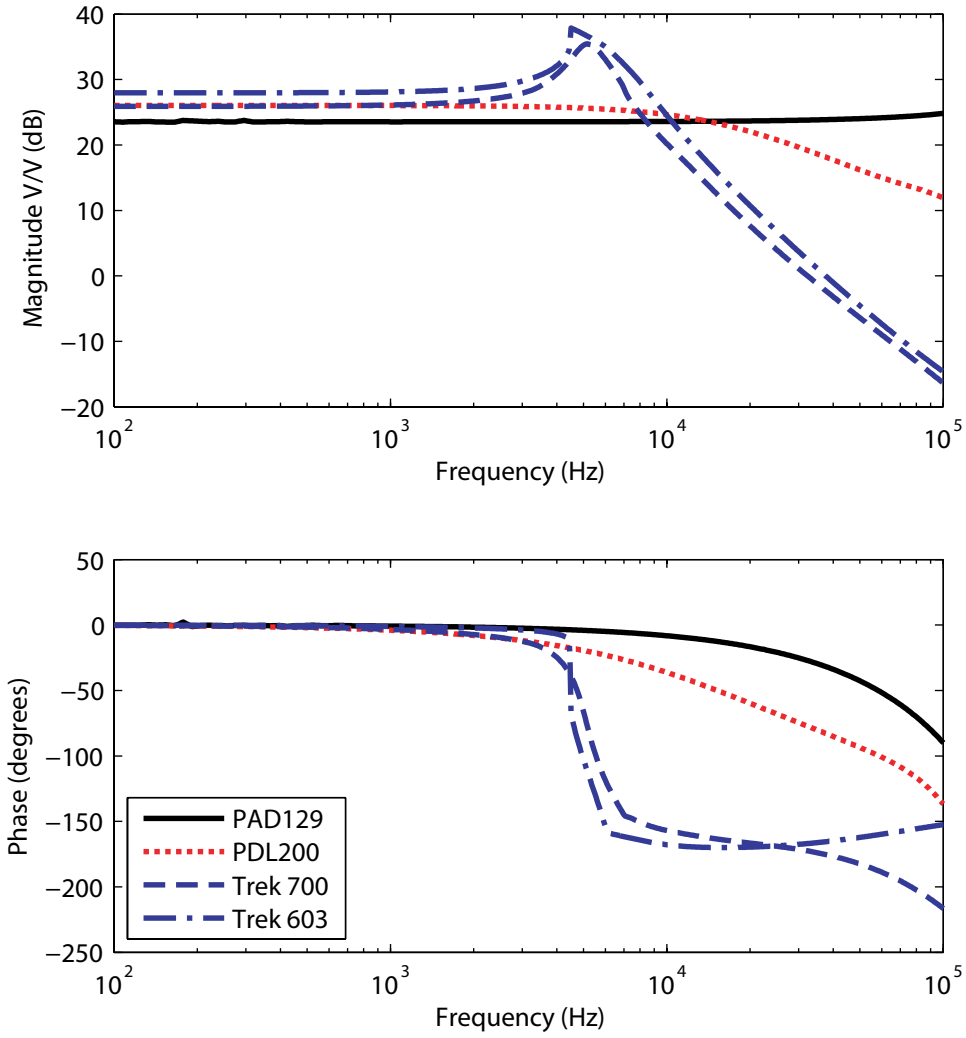

Figure 4.6: Frequency response plots for various power supplies with a capacitive load of 442 nF.

4.2 Position Sensing

Position sensors are transducers that convert the physical input of displacement into a measurable signal, usually voltage. The key attributes for high-speed nanopositioning are resolution and bandwidth. Although there are many types of position sensors, the two types used in this project are capacitive, and inductive sensors.

The x-axis displacement is measured with a Kaman inductive sensor (SMU9000-15N). The Kaman inductive sensor is ideal for this application because it offers reasonably high-bandwidth of 10 kHz, good resolution of 0.1 nm, and it is compact and light weight. Size and weight are an important factor because the x-sensor is mounted to the y-stage body. Increased mass will adversely affect the y-stage performance. An ADE capacitive sensor (ADE 2805 sensor with ADE 4810S module) is used to measure the y-displacement. The ADE capacitive sensor is larger, has lower bandwidth of 1 kHz, and lower resolution of 1.6 nm.

The sensors are mounted to the nanopositioner by feeding them through holes drilled directly into the stage body and securing them with set screws. Figure 4.7 shows a top view of the nanopositioning stage to show the locations of the sensors. The hole for the y-sensor is drilled through the ground-stage along the y-axis aligned with the y-piezoactuator. The hole for the x-sensor is drilled through the ground-stage and the y-stage along the x-axis and aligned with the x-piezoactuator. The x-sensor is thus mounted directly to the y-stage and therefore measures displacement of the x-stage with respect to the y-stage. The problem with this configuration is that runout of the y-stage along the x-axis is unmeasurable. Additionally, small distortion in the y-stage due to y-actuation may cause the x-actuator to move laterally with respect to the x-stage. As a result, the sensor reading may not represent the true displacement of the sample.

For dynamic characterization of the high-speed stage, a single point compact laser vibrometer (Polytec CLV-1000 with CLV M200 Input Module, CLV M030 Decoder Module, CLV M001 output module, and CLV-800-vf25 laser unit) was used because its very-high-bandwidth of 250 kHz. To do this, the inductive and capacitive sensors were removed from the stage and the laser was aimed through the sensor holes on to the face of the stages. The single point laser vibrometer was not used for displacement

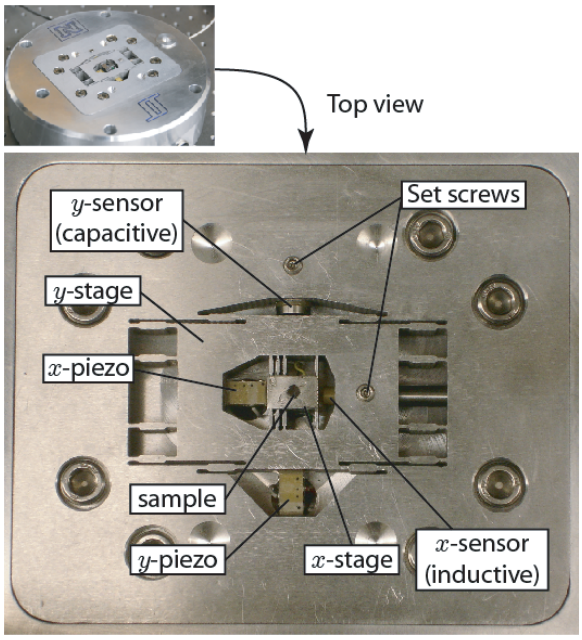

Figure 4.7: Top view of nanopositioner showing the mounting locations of the x-and y-sensors.

measurement because it is strictly a doppler based velocity sensor. Table 4.3 provides the range, resolution, and bandwidth information for the three sensors used in this project.

Table 4.3: Displacement sensors.

Model	Range μm	Resolution nm	Bandwidth kHz
ADE capacitive sensor	50	1.6	1
Kaman Inductive Sensor	900	0.1	10
Polytec CLV	N/A	500 s^{-}1	250

Chapter 5

Stage Performance Characterization

This chapter explains how the stage performance was measured to validate the expected performance of the mechanical design. In Section 5.1 the in-plane flexure stiffness is measured prior to assembly and compared to predicted stiffness values. In Section 5.2 the maximum x- and y-axis range and sensor cross-coupling is measured by applying the maximum voltage to the piezoactuators and measuring the displacements. In Section 5.3 the stage dynamics are measured through frequency response analyses.

5.1 Stiffness

The fabricated scanner shown in Fig. 3.17 is tested to determine the stiffness, maximum range, and dynamic characteristics. Prior to assembly, the actuation stiffness of the x- and y-stage flexures are determined by taking the ratio of the measured displacement due to an applied load. Static loads are applied to the stages by mounting the scanner to a fixture with the z-axis perpendicular to ground, then running a cable

through the hole in the x-stage, and hanging masses from the cable. For example, a positive load is applied to the x-stage by orienting the scanner so the x-axis is pointing down (in the direction of gravity) allowing the cable/mass system to apply a load in the positive x-direction. A total of 15 Lbf (66.7 N) is applied in the positive and negative direction in 2.5 Lbf (11.1 N) increments. Displacement is measured using the Kaman inductive sensor (SMU9000-15N). The flexures for the x-, and y-stages were designed to have the thin sections of the flexures to be 0.4 and 0.8 mm thick, resulting in actuation stiffness of 10 and 6 n/μm respectively. The thickness of the fabricated flexures were measured to be 0.37 and 0.77 mm thick. Figure 5.1 shows the measured displacements due to loading for the x- and y-stages along with the expected stiffness for the fabricated flexures. The analytical, FEA predicted, and measured stiffness is 7.82, 7.42, and 3.81 N/μm, respectively, for the x-stage and 4.28, 4.04, and 5.10 N/μm, respectively, for the y-stage. The large discrepancy between the desired (designed) and measured values are attributed to poor machining tolerances. The discrepancy between the predicted and measured x-stage stiffness value is attributed to poor thickness measurements.

5.2 Range and Cross-Coupling

The displacement characteristics of the sample platform are measured using the Kaman inductive sensor. Application of 180 V peak-to-peak sine input at 10 Hz to the x and y piezoactuators resulted in 8.19 μm and 8.34 μm travel, respectively. Over these ranges, the measured x/y sensor cross-coupling is measured at 75 nm peak-to-peak (1.83% or -34.75 dB) caused by actuating the x piezo and 24 nm peak-to-peak (0.6% or -44.44 dB) caused by actuating the y piezo. The measured time responses at 10 Hz scanning (sine wave input) for the lateral cross-coupling are shown in Fig. 5.2(a). The measured vertical runouts are 27.6 nm peak-to-peak (0.35% or -49.2 dB) caused by

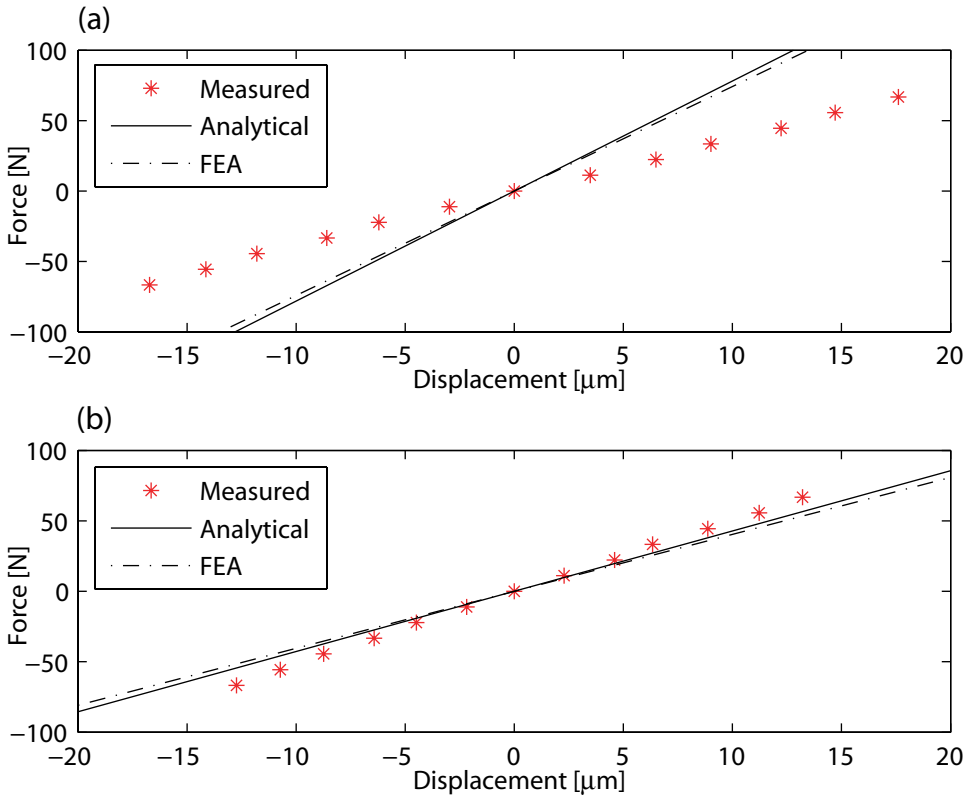

Figure 5.1: Flexure stiffness comparison for the x- and y-stage.

actuating the x piezo and 81.4 nm peak-to-peak (0.97% or -40.3 dB) caused by actuating the y piezo. The measured time responses at 100 Hz scanning (sine wave input) for the vertical runout are shown in Fig. 5.2(b). It is noted that in the sensor configuration of the design described, lateral x-to-y and y-to-x cross-coupling may be caused by y-stage compliance. For example, x-actuation may cause slight deformation in the y-stage body leading to sensor cross-coupling. Lateral-to-vertical cross-coupling such as x-to-z and y-to-z may be caused by a tilted sample or sensor surface, *i.e.*, when the tilted sample translates laterally, the surface translates vertically relative to a fixed sensor. Since the x- and y-axes can tolerate a maximum of 200 V, the maximum lateral range of the stage is approximately 9×9 μm. Application of 200 V peak-to-peak sine input at 10 Hz to the vertical z piezoactuators will give approximately 1 μm of travel.

5.3 Dynamics

Frequency response functions are measured using a dynamic signal analyzer (Stanford Research Systems SRT785). Small inputs (<70 mV) are applied to the piezo amplifiers during the test to minimize the effect of nonlinearity such as hysteresis. Measurements for the x- and y-stages where taken with both the stage mounted sensors (inductive sensor for x, and ADE Capacitive sensor for y) and again with a single point laser vibrometer (Polytec CLV-1000 with CLV-800-vf40 laser unit) mounted to the vibration table (for both x and y). The sensor setup for measuring the x-axis frequency response with the CLV is shown in Fig. 5.3 where (a) shows the general configuration, and (b) shows a closeup view of the stage. In this configuration, the x-axis inductive sensor is taken out and the laser is pointed through the sensor mount hole onto the x-stage face.

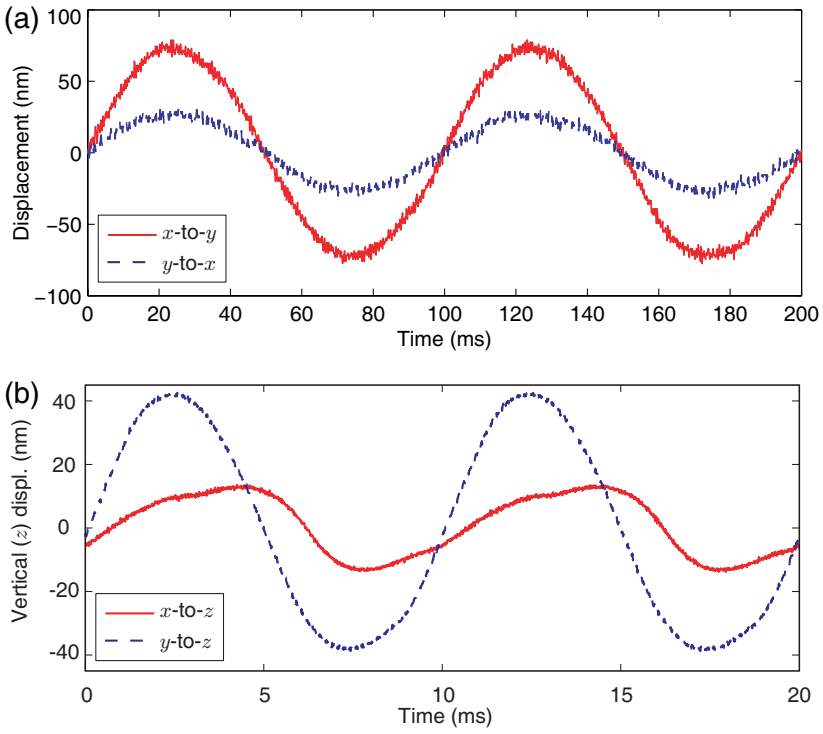

Figure 5.2: Measured cross-coupling due to actuating in x and y. Input voltage to x and y is a 180 V, peak-to-peak sine wave at (a) 10 Hz and (b) 100 Hz.

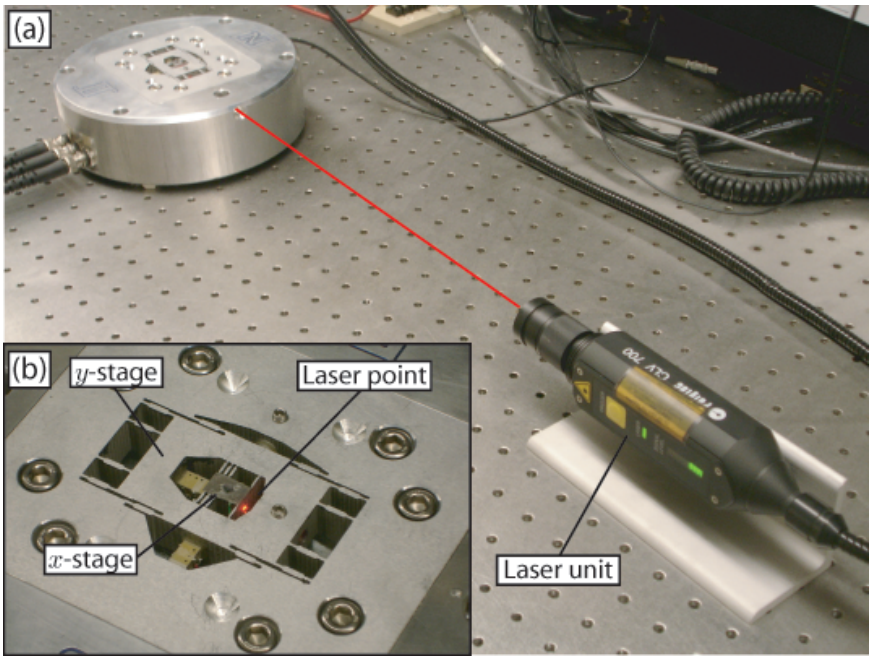

Figure 5.3: CLV (laser sensor) configuration for measuring the x-axis frequency response.

The measured responses for the x- and y-stage are shown in Fig. 5.5 along with the FEA predictions. When measured relative to the y-stage body, the x-stage has a dominant first resonance peak at 24.2 kHz (a2) which matches well with the predicted value of 25.9 kHz (a1). Several small pole/zero pairs appear before the dominant peak. However, when measured relative to an outside body such as the vibration isolation table with a laser vibrometer (a3), the response shows additional unexpected resonances. These peaks are thought to be due to modes in the y-stage being excited by the x-stage. Unfortunately, these modes are not detectable when the sensor is attached to the y-stage body because the measurement is of the x-stage relative to the y-stage body. The measured results for the y-stage of 6.00 kHz for the capacitive sensor on stage body (a2) and laser vibrometer from on table (a3) match the predicted FEA value (a1) of 5.96 kHz very well. It is pointed out that the dominant resonances agree with the FEA results, and they are piston modes relative the their mounting point as predicted by FEA. The frequency response for the z-axis is mea-

sured using the deflection of a 360 kHz tapping-mode AFM cantilever (Vista Probes T300 www.vistaprobes.com) in contact-mode over the sample surface. The results for the z-stage frequency response are shown in Fig.5.6 where the dominant resonance is approximately 70 kHz in the actuation (piston) mode.

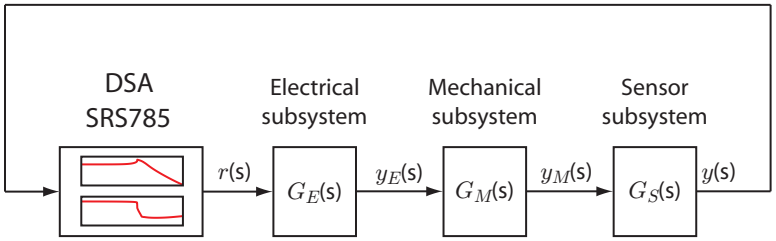

Figure 5.4: Block diagram for system frequency response analysis.

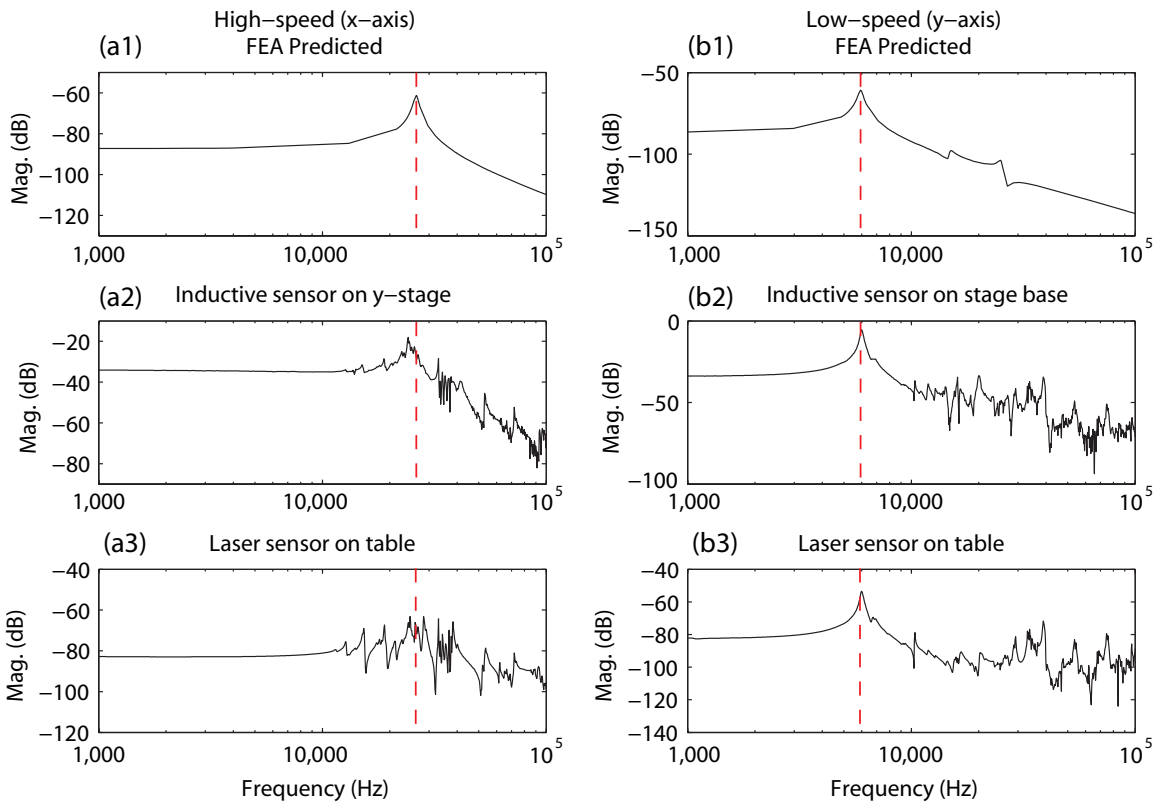

Figure 5.5: (a1)-(a3) Comparison of predicted and measured frequency response functions for the high-speed stage (x-axis) and (b1)-(b3) the low-speed stage (y-axis). The vertical dashed lines, aligned with the predicted first mechanical resonance of 25.9 kHz for the high-speed x-stage in (a1)-(a3) and 5.96 kHz for the low speed y-stage in (b1)-(b3), is used to compare the experimentally measured results to the FEA predicted first resonance peak. When measured from the y-stage body, the high-speed x-stage matches the predicted well with a dominant peak at 24.2 kHz with relatively small peaks occurring at 15.0, 18.8, and 22.8 kHz. However, when measured from the ground using the laser vibrometer, the resonance mode at 24.2 kHz is not dominantly large compared to the peaks at 15.0, 18.8, and 22.8 kHz. For the y-stage, the FEA predicted value of 5.96 kHz and experimentally measured values of 6.00 kHz match very well.

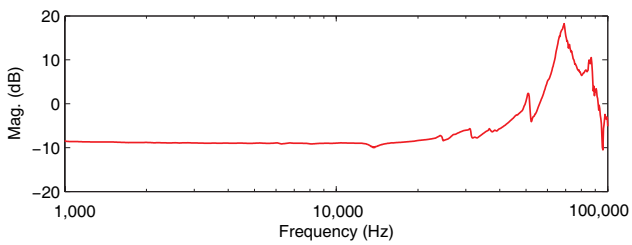

Figure 5.6: Measured z-stage frequency response.

Chapter 6

Control

Due to the hysteresis and creep behaviors in the piezo-stack actuators and the inherent structural dynamics, control is required for precision positioning, especially at high scan frequencies [16, 60]. Unfortunately, one control method cannot cover the full operating range and frequency of the stage. Therefore, four methods to control the actuation of the stage in the lateral directions are investigated: (1) open-loop with smooth inputs, (2) PID feedback control (which is the industry standard), (3) discrete-time repetitive control, and (4) model-based feedforward control. In the end, the user selects a controller based on the operating range and frequency, and required precision. Also, the complexity of the controller should be considered as more time is required to appropriately tune a given controller.

6.1 System

The open-loop system is represented in Fig. 6.1. The system includes a personal computer with custom developed LabView graphic user interface (GUI) (developed by Pat Leang), high-speed National Instruments data acquisition hardware, power amplifiers, high-speed nanopositioning stage, x- and y-axis position sensors, and the NanoSurf AFM head.

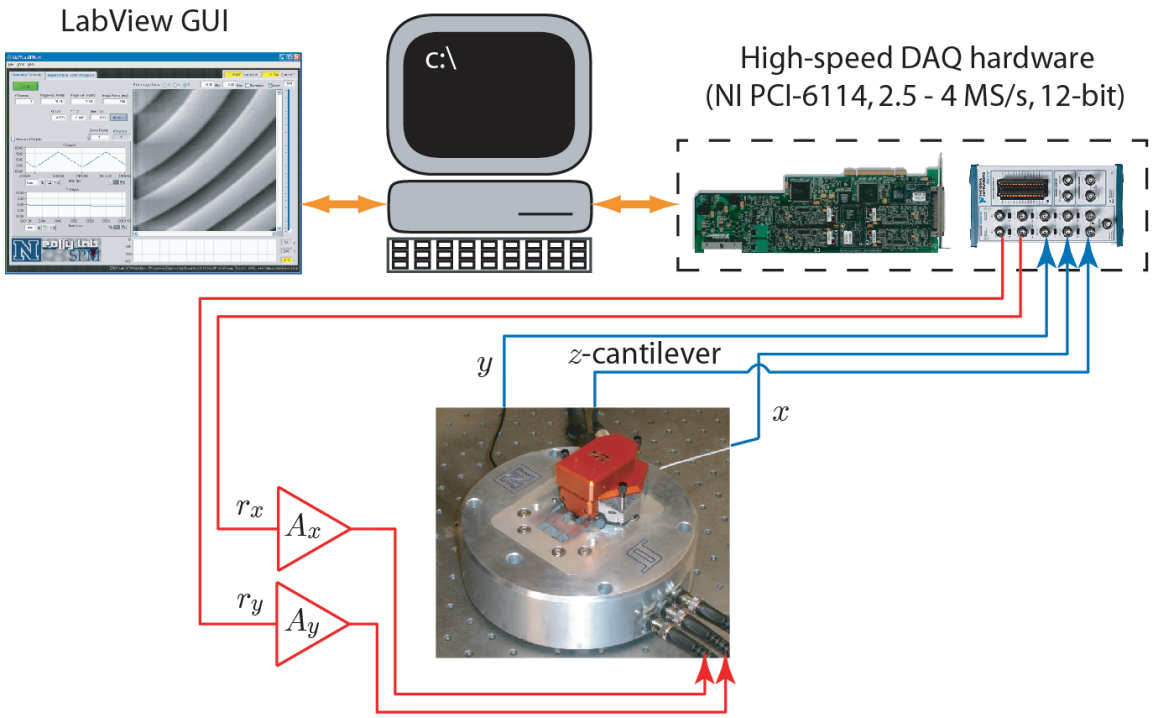

Figure 6.1: Block Diagram for open loop imaging.

6.1.1 SPM Imaging Software

The SPM imaging GUI shown in Fig.6.2 was developed by Pat Leang using National Instruments LabView software. The GUI allows the user to select and adjust imaging parameters such as reference trajectory amplitude and shape, line rate, number of data points per line, number of lines per image, back-scan delay, and number of consecutive images. The software was used to input reference trajectories for both tracking and imaging experiments.

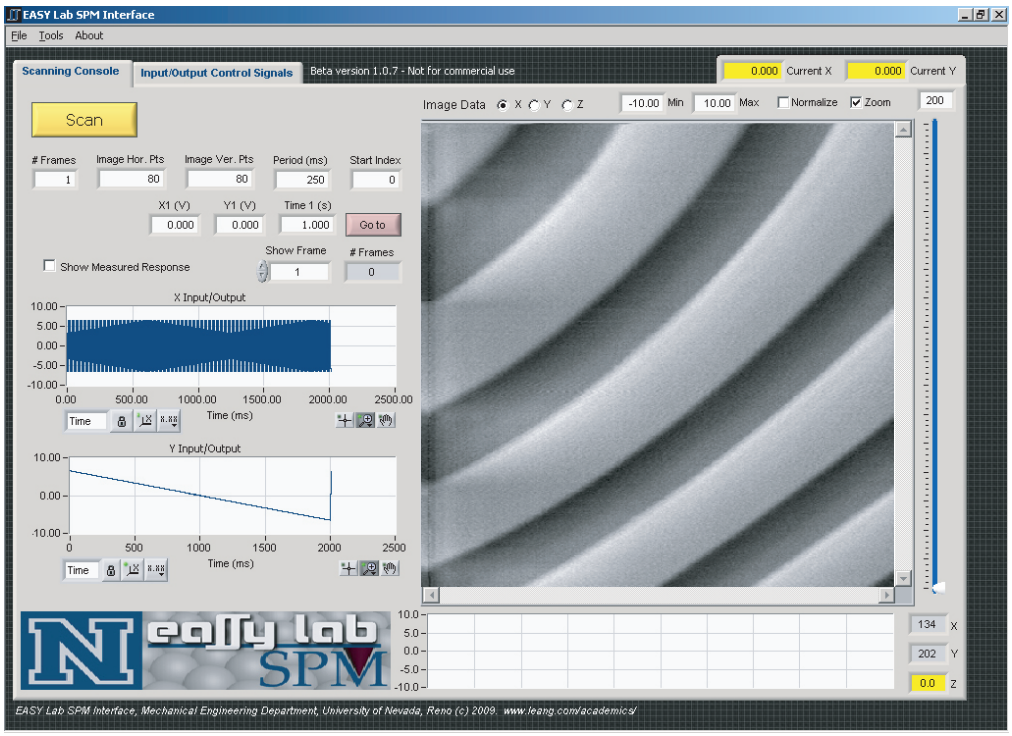

(a) Scanning Console

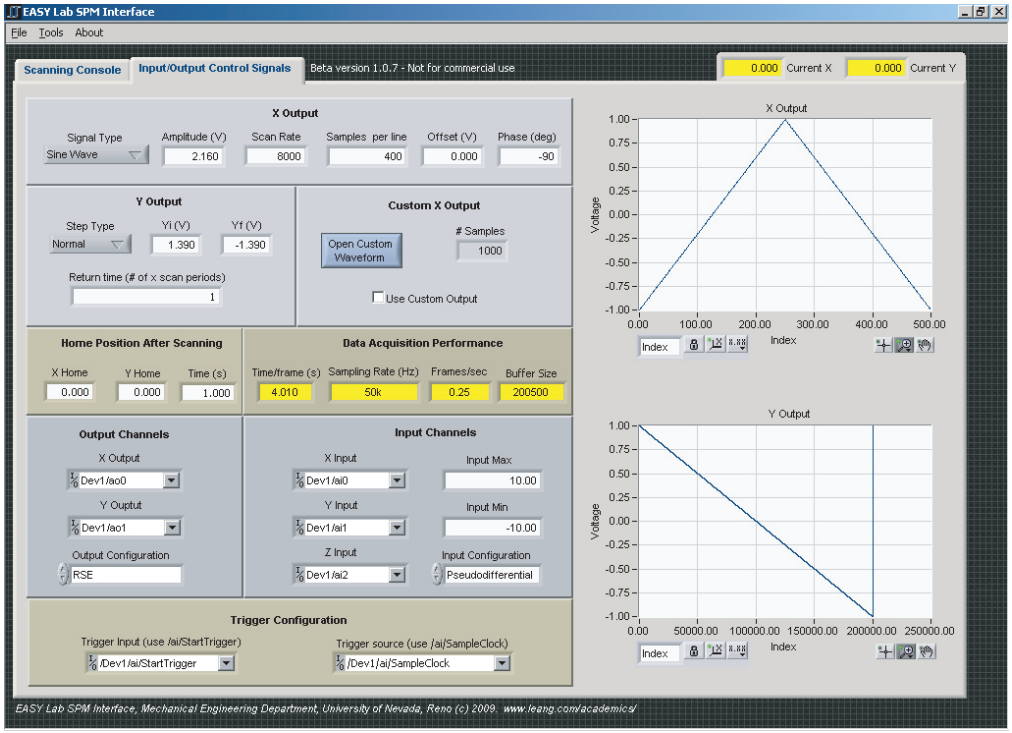

(b) Input/Output Control Signals

Figure 6.2: EASY Lab SPM imaging software GUI.

6.2 Open-Loop Smooth Input Signal

Nanopositioners used in SPM systems for scanning applications are commonly driven by triangle input signals. Such a signal is used because it causes the stage move to with constant velocity across the sample surface. However, a triangle input signal can excite the dynamics of the stage due to the sharp turn-around points. To minimize this, a smooth triangle input signal consisting of ten term Fourier representation is created to control the positioning along the x direction. Other input-shaping techniques can also be applied with the same objective [33, 61].

The Fourier series expansion for a function $f(x)$ of period $p = 2L$ is

$$F(x) = a_0 + \sum_{n=1}^{\infty} \left(a_n \cos \frac{n\pi}{L} x + b_n \sin \frac{n\pi}{L} x \right) \tag{6.1}$$

where L is the half period length and

$$a_0 = \frac{1}{2L} \int_{-L}^{L} f(x)\ dx \tag{6.2}$$

$$a_n = \frac{1}{L} \int_{-L}^{L} f(x) \cos \frac{n\pi x}{L}\ dx \tag{6.3}$$

$$b_n = \frac{1}{L} \int_{-L}^{L} f(x) \sin \frac{n\pi x}{L}\ dx \tag{6.4}$$

are the Fourier coefficients of $f(x)$. The equation for a triangle wave is

$$f(x) = \begin{cases} \frac{-2Ax}{L} - A & , x \in [-L, 0] \\ \frac{2Ax}{L} - A & , x \in [0, L] \end{cases} \tag{6.5}$$

where A is the amplitude. Substituting Eq. (6.5) into Eqs. (6.2)–(6.4) gives the

coefficients;

$$\begin{aligned} a_0 &= \frac{1}{2L}\left[\int_{-L}^{0}\left(\frac{-2Ax}{L}-A\right)\,dx+\int_{0}^{L}\left(\frac{2Ax}{L}-A\right)\,dx\right] \\ &= \frac{1}{2L}\left[0-(-AL+AL)+(AL-AL)-0\right] \\ &= 0, \end{aligned} \tag{6.6}$$

$$\begin{aligned} a_n &= \frac{1}{L}\left[\int_{-L}^{0}\left(\frac{-2Ax}{L}-A\right)\cos\left(\frac{n\pi x}{L}\right)dx+\int_{0}^{L}\left(\frac{2Ax}{L}-A\right)\cos\left(\frac{n\pi x}{L}\right)dx\right] \\ &= \frac{1}{L}\left[\frac{AL[\pi n\sin(\pi n)+2\cos(\pi n)-2]}{\pi^2n^2}+\frac{AL[\pi n\sin(\pi n)+2\cos(\pi n)-2]}{\pi^2n^2}\right] \\ &= \frac{2A[\pi n\sin(\pi n)+2\cos(\pi n)-2]}{\pi^2n^2}, \end{aligned} \tag{6.7}$$

and

$$\begin{aligned} b_n &= \frac{1}{L}\left[\int_{-L}^{0}\left(\frac{-2Ax}{L}-A\right)\sin\left(\frac{n\pi x}{L}\right)dx+\int_{0}^{L}\left(\frac{2Ax}{L}-A\right)\sin\left(\frac{n\pi x}{L}\right)dx\right] \\ &= \frac{1}{L}\left[\frac{AL[\pi n+\pi n\cos(\pi n)-2\sin(\pi n)]}{\pi^2n^2}-\frac{AL[\pi n+\pi n\cos(\pi n)-2\sin(\pi n)]}{\pi^2n^2}\right] \\ &= 0. \end{aligned} \tag{6.8}$$

Equations (6.2)–(6.4) are then substituted into Eq. (6.1) to give the Fourier series expansion representation of a triangle wave

$$f(x)=\sum_{n=}^{\infty}\left[\frac{2A[\pi n\sin(\pi n)+2\cos(\pi n)-2]}{\pi^2n^2}\cos\left(\frac{n\pi x}{L}\right)\right] \tag{6.9}$$

where n is the number of terms. A ten-term Fourier series expansion for a triangle wave is formed using the MATLAB code in Appendix A.1. Figure 6.3 shows the ten-term Fourier series triangle wave ($n = 10$) with a period p of 1000 data points and an amplitude A of 5.048 volts compared to a pure triangle wave.

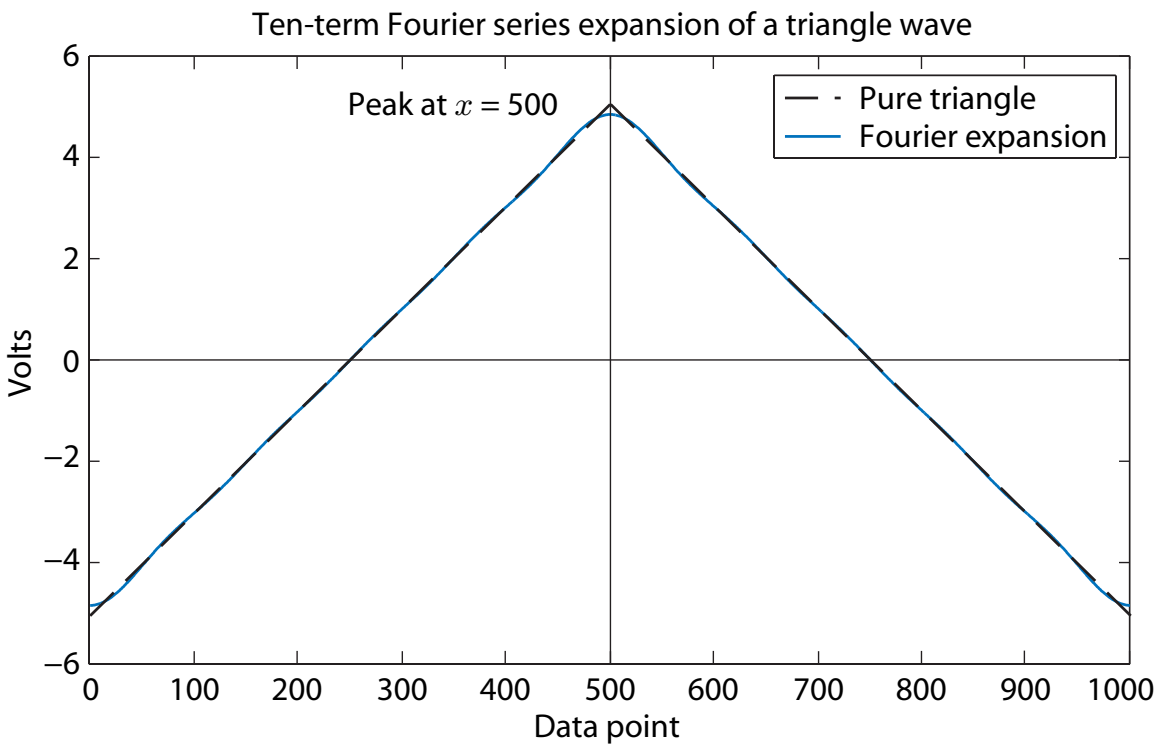

Figure 6.3: Ten-term Fourier triangle wave compared to a pure triangle.

6.3 Analog PID Control

Proportional-integral-derivative control is the industry standard for nanopositioners. When the stage is operated at low frequencies, such as less than 1 kHz, standard PID feedback control is an effective approach to minimize creep and hysteresis, as well as to improve dynamic performance. An analog PID control board is designed to control the positioning along the lateral directions, where the controller transfer function is given by

$$C(s) = \frac{U(s)}{E(s)} = k_p + \frac{k_i}{s} + k_d s. \tag{6.10}$$

Such a controller is easy to implement and established methods are available for tuning it. Figure 6.5 shows the block diagram and fabricated board based on the Linear Technology LT1362 high-speed operational amplifier. The board is designed

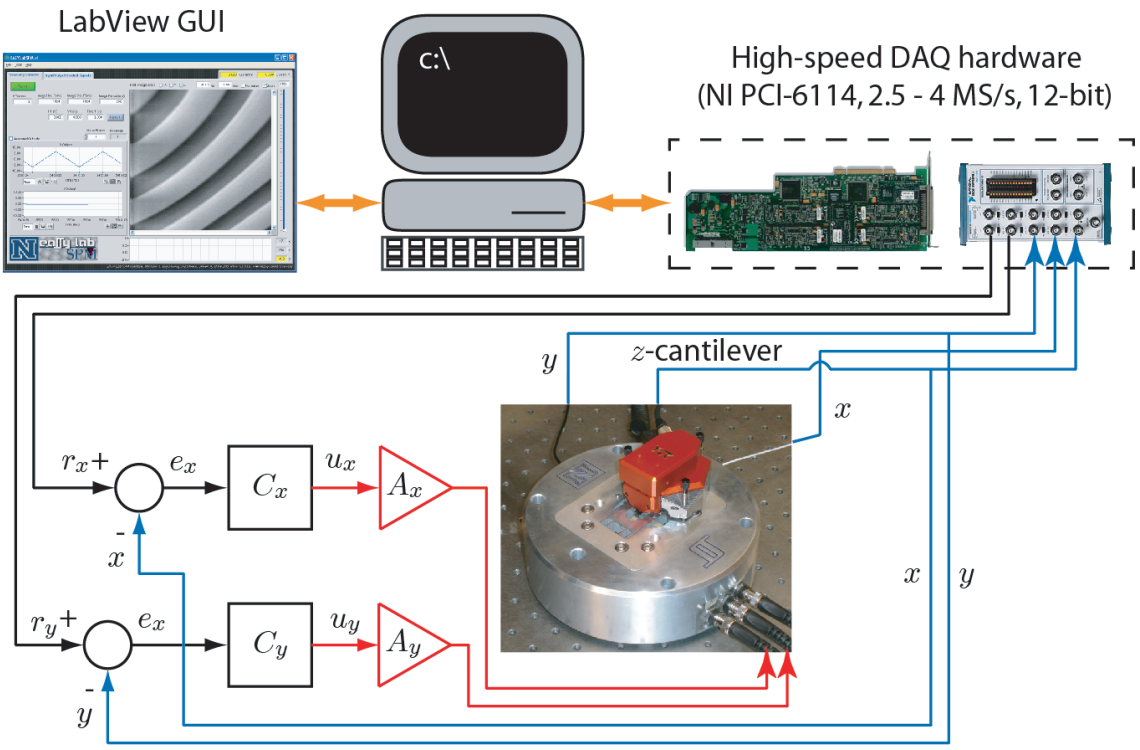

Figure 6.4: Block Diagram for closed loop imaging.

to accommodate feedforward inputs u_1, u_2 and u_{ff}, for implementing integrated controllers [62]. The PID gains are tuned using a dynamics model of the positioning stage. For example, the measured frequency response functions shown in Fig. 5.5 are curve fitted to linear transfer function models using the Matlab System Identification toolbox ©. For the low-speed axis (y), the derivative term is omitted ($k_d = 0$) and integral control is used with a gain of approximately $k_i = 30,000$. The measured bandwidth (-3.01 dB cutoff) of the controller in the y direction is 300 Hz. For the x axis, the PID gains are tuned to $kp = 1.2$, $k_i = 1 \times 10^5$, and $k_d = 1 \times 10^{-5}$. The control bandwidth is 2.5 kHz.

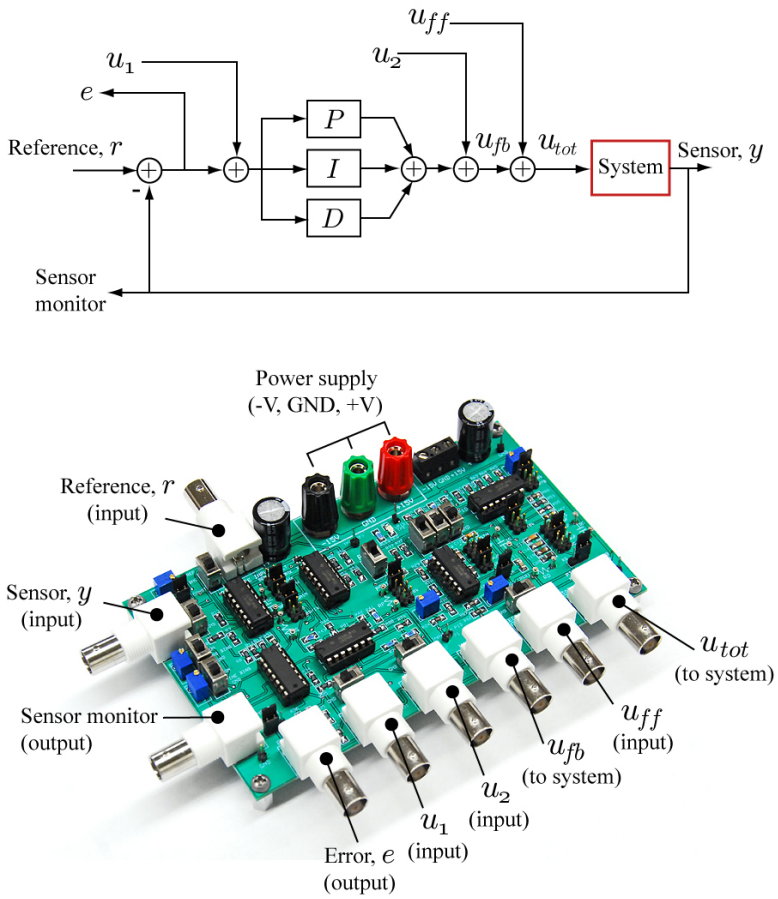

Figure 6.5: Analog PID feedback controller board. Two boards are used to control the x and y axes.

6.4 FPGA-Based Discrete-Time Repetitive Control

For relatively low-speed positioning, PID control is adequate. However, as the scanning speed increases, significant tracking error exists due to dynamic effects. Particularly, the tracking error for periodic scanning motion repeats from one period to the next. To improve the tracking precision for scanning applications in which the desired trajectory is periodic, repetitive control (RC) is added to the PID controller for positioning along the high-speed x-axis. For applications such as AFM imaging, the low-speed y-axis operates at a significantly lower frequency than the x-axis, therefore

RC is only applied to the x-axis.

Repetitive control is based on the Internal Model Principle [63], where a signal generator is incorporated into a feedback control loop for tracking periodic reference trajectories [64]. Repetitive and iteration-based control methods can reduce the tracking error from one operating cycle to the next for high performance operation. In SPM applications such as imaging and patterning, the reference signal is periodic and the scanning period is often known in advance.

The block diagram of the plug-in RC is shown in Fig. 6.6(a), where a signal generator with period T_p is created by a positive feedback loop and pure delay z^{-N}. The positive integer $N = T_p/T_s \in \mathbb{N}$ is the number of points per period of the reference trajectory $r(t)$ and T_s is the sampling period. The plant (*i.e.*, piezo-stack actuator) is assumed to be linear and represented by the transfer function $G(z)$, where $z = e^{j\omega T_s}$, $\omega \in (0, \pi/T_s)$. The PID controller is represented by $G_c(z)$. The low-pass filter $Q(z)$ in the RC block provides stability by reducing the effects of high gain at high frequencies. The parameters for the RC include the RC gain k_{rc} and two phase lead compensators $P_1(z) = z^{m_1}$ and $P_2(z) = z^{m_2}$, where m_1 and m_2 provide a linear phase lead (in units of radians) of $\theta_i(\omega) = m_i T_s \omega$, for $i = 1, 2$ and $\omega \in (0, \pi/T_s)$. The two phase lead compensators can be adjusted to compensate for the phase lag in the closed-loop system and to improve the tracking performance. By inspection, the transfer function of the signal generator that relates $E(z)$ to $A(z)$ in Fig. 6.6(a) is given by

$$\frac{A(z)}{E(z)} = \frac{Q(z)P_1(z)z^{-N}}{1 - Q(z)P_1(z)z^{-N}} = \frac{Q(z)z^{(-N+m_1)}}{1 - Q(z)z^{(-N+m_1)}}. \tag{6.11}$$

In the absence of the low-pass filter $Q(z)$ and positive phase lead $P_1(z) = z^{m_1}$, the poles of the signal generator are $1 - z^{-N} = 0$, which implies infinite gain at the harmonics of the periodic reference trajectory. Such large gain is what gives the RC

its ability to track periodic trajectories. However, practical RC design requires a low-pass filter $Q(z)$ because the large gain at high frequencies can lead to instability of the closed-loop system. For simplicity, a standard low-pass filter of the form $Q(z) = \frac{a}{z+b}$, where $|a| + |b| = 1$, is chosen. The cut-off frequency of the low pass filter is set to 7 kHz. Alternatively, a zero-phase filter can also be considered [65, 66].

The stability of the RC system is presented as follows. Let $H(z) = Q(z)z^{(-N+m_1)}$ and $G_0(z) = G_c(z)G(z)$. It is assumed that (1) the reference trajectory $R(z)$ is periodic and (2) the closed-loop system without the RC loop is asymptotically stable, *i.e.*, $1 + G_c(z)G(z) = 0$ has no roots outside of the unit circle in the z-plane.

The stability is shown by applying the Small Gain Theorem [67]. First, the transfer function relating the reference trajectory $R(z)$ and the tracking error $E(z)$ is

$$S_{rc}(z) = \frac{E(z)}{R(z)} = \frac{[1 - H(z)]S(z)}{1 - H(z)[1 - k_{rc}P_2(z)G_0(z)S(z)]}, \tag{6.12}$$

where $S(z) = 1/(1+G_0(z))$ is the sensitivity function of the feedback system without the repetitive controller. Furthermore, let $T(z)$ represent the complimentary sensitive function of the closed-loop feedback system without RC, that is, $T(z) = G_0(z)S(z)$. Since $S(z)$ has no poles outside the unit circle in the z-plane, it is stable. Replacing $z = e^{j\omega T_s}$, and since $1 - H(z)$ stable, the positive feedback closed-loop system in Fig. 6.6(b) is asymptotically stable when

$$\begin{aligned} &|H(z)[1 - k_{rc}P_2(z)G_0(z)S(z)]| = \\ &|H(e^{j\omega T_s})[1 - k_{rc}e^{j\theta_2(\omega)}G_0(e^{j\omega T_s})S(e^{j\omega T_s})]| < 1, \end{aligned} \tag{6.13}$$

for all $\omega \in (0, \pi/T_s)$, where the phase lead $\theta_2(\omega) = m_2T_s$. Observing that $|Q(e^{j\omega T_s})| \leq 1$ and replacing the complimentary sensitive function of the closed-loop system without RC with $T(e^{j\omega T_s}) = A(\omega)e^{j\theta_T(\omega)}$, where $A(\omega) > 0$ and $\theta_T(\omega)$ are the magnitude and

phase of $T(e^{j\omega T_s})$, respectively, Eq. (6.13) can be simplified to

$$|1 - k_{rc}A(\omega)e^{j[\theta_T(\omega)+\theta_2(\omega)]}| < 1. \tag{6.14}$$

Therefore, the system is stable if

$$\begin{aligned} 0 < k_{rc} < \frac{2\cos[\theta_T(\omega) + \theta_2(\omega)]}{A(\omega)} \quad \text{and} \\ -\pi/2 < [\theta_T(\omega) + \theta_2(\omega)] < \pi/2. \end{aligned} \tag{6.15}$$

The RC is implemented using FPGA hardware, National Instruments cRIO-9002, using $N = 100$, $m_1 = 6$, $m_2 = 0$, and closed-loop sampling frequency of 100 kHz. The RC gain is chosen as $k_{rc} = 0.95$ to satisfy the stability conditions given in Eq. (6.15). Additional details of RC design for SPM can be found in [68].

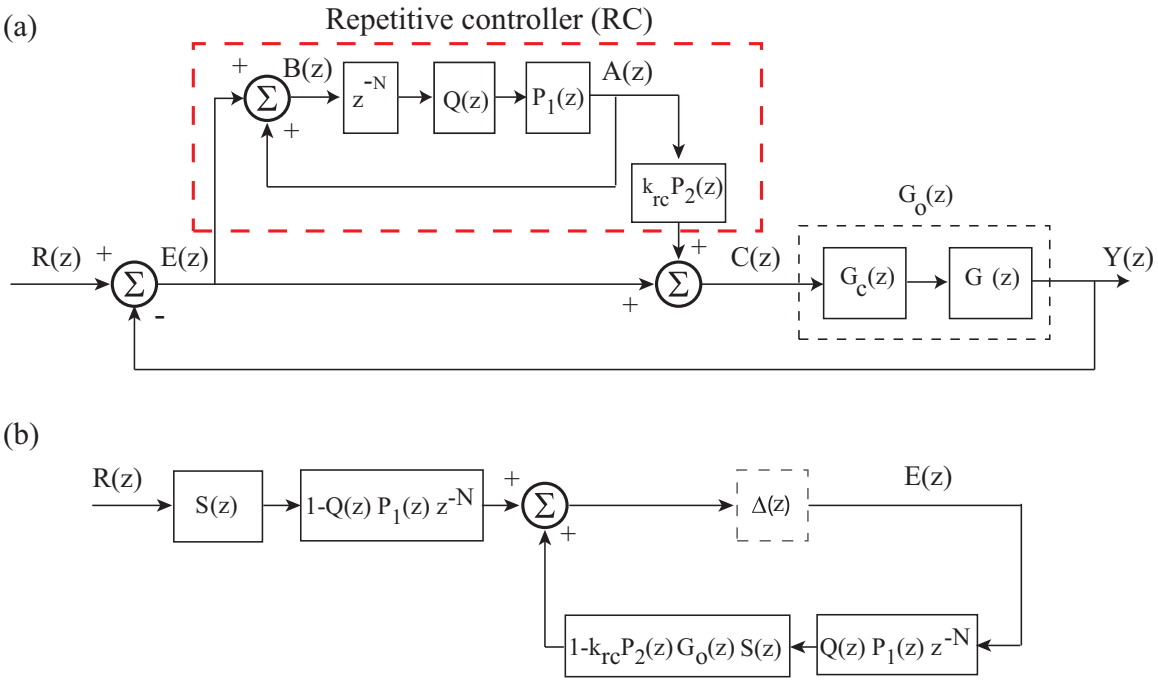

Figure 6.6: Repetitive control for nanopositioning: (a) a plug-in RC with phase lead compensators, $P_1(z)$ and $P_2(z)$, to enhance performance; (b) equivalent system for stability analysis.

6.5 Feedforward Hysteresis and Dynamic Compensation

The piezoactuators used to displace the sample platform exhibits hysteresis, and at high scan rates, vibrational dynamics also cause additional tracking error. Model-based feedforward control can be used to minimize both effects [16, 60]. Since during scanning, the x-axis is operated at high frequencies, both dynamic and hysteresis feedforward compensation are applied to this axis (see Fig. 6.7). Closed-loop integral control is used for the low-speed y axis to minimize hysteresis and creep effect. To minimize excitation of high-order dynamics and out-of-plane modes along the x axis, the desired output trajectory $x_d(t)$ is chosen as a sine wave and the inversion-based approach is used to determine the feedforward input, specifically

$$V_{ff}(j\omega) = G(j\omega)^{-1} X_d(j\omega), \tag{6.16}$$

where $G(j\omega)^{-1}$ is the inverse of the plant dynamics and $X_d(j\omega)$ is the Fourier transform of the desired output trajectory. The inverse of the plant is determined from the measured frequency response function for the x-direction [see Fig. 5.5(a2)]. Then, the time-domain solution to the feedforward input $v_{ff}(t)$ is computed by the inverse Fourier transform of $V_{ff}(j\omega)$.

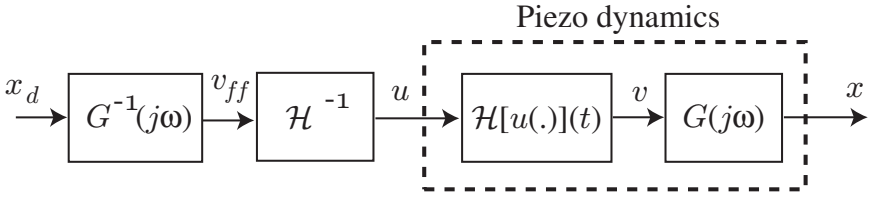

Figure 6.7: The inversion-based feedforward control approach.

Afterwards, the dynamic-compensated feedforward input $v_{ff}(t)$ is used as an input to a hysteresis feedforward compensator, $\mathcal{H}^{-1}[\cdot]$. The compensator is based on the Prandtl-Ishlinskii (P-I) model [69–71]. Particularly, an inverse of the P-I model is proposed based on the observation of the shape of the input versus output curve shown in Fig. 6.8(a) (u vs. v plot). For such a curve, the inverse-play-type operator shown in Fig. 6.8(b) is proposed for constructing the inverse model, where the inverse-play operator is described by

$$\mathcal{P}_{inv,r'}[v](0) = p_{inv,r'}(h(0), 0) = 0, \tag{6.17}$$

with $\mathcal{P}_{inv,r'}[v](t) = p_{inv,r'}(h(t_i), \mathcal{P}_{inv,r'}[h](t_i))$. In (6.17), $p_{inv,r'}(h(t), p_{inv,r'}[h](t_i)) = \max(-h - r', \min(-h + r', p_{inv,r'}[h](t_{i-1})))$ and r' denotes the threshold of the inverse-play operator. Then, the output of the inverse hysteresis model is given by

$$\mathcal{H}^{-1}[v](t) \triangleq k_{inv}h(t) + \int_0^R d_{inv}(r')\mathcal{P}_{inv,r'}[v](t)dr'. \tag{6.18}$$

The function $h(t) = g_0'v(t) + g_1'$, where $v(t)$ is the output of the hysteresis behavior and g_0' and g_1' are constants. The parameters for the inverse model are obtained by curve-fitting the measured input-output data (hysteresis curve) using the nonlinear least-square optimization toolbox in Matlab. Specifically, the density function is chosen as $d_{inv}(r') = \lambda' e^{-\delta' r'}$, where $r' = \rho' j$, for $j = 1, 2, \cdots, 8$. The parameters are determined as $g_0' = 2.7742$, $g_1' = -0.0123$, $\lambda' = 0.0211$, $\delta' = -3.851$, $\rho' = 0.1322$, and $k' = 1$.

One of the advantages of the P-I model over other hysteresis models such as the Preisach model is the smaller number of parameters that need to be identified, and as a result, the model is more computationally efficient for real-time applications [71].

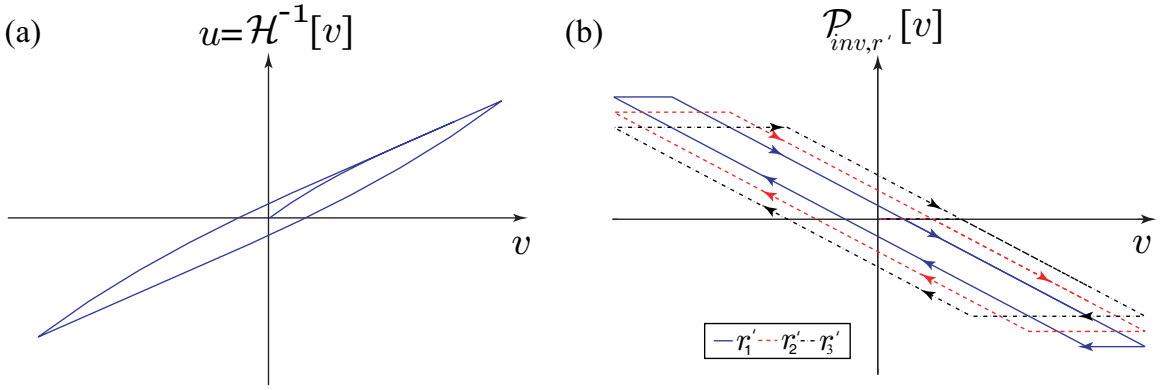

Figure 6.8: Operators for the inverse P-I model: (a) input versus measured output plot (hysteresis curve); (b) play-type operator for the inverse model with threshold r'.

Chapter 7

Tracking and AFM Imaging Results

Tracking and AFM imaging results are presented to demonstrate the performance of the control methods and capabilities of the positioning stage. First, tracking results for the high-speed stage are presented in Sec. 7.1 to show its performance with and without feedback and feedforward control. Next, preliminary AFM imaging are obtained using the commercial in Sec. 7.2 using the Nanosurf easyScan 2 at 1 Hz and 10 Hz line rates to show the limitations. Finally, high-speed AFM images are presented to show the increased performance of the combined system.

7.1 High-Speed Tracking

Six approaches to control the positioning along the fast-scan direction (x-axis) are compared: (1) open-loop triangle input (OL), (2) open-loop smooth triangle input (ST), (3) PID control (FB), (4) repetitive control (RC), (5) dynamic and hysteresis feedforward control (FF), and (6) sine-wave feedforward control (SF).

The lateral movements of the stage are measured with an inductive (x-axis) and capacitive sensor (y-axis). The maximum and root-mean-squared tracking error (as a

percentage of the total displacement range) for different scan frequencies are listed in Table 7.1. A sample of the tracking performance at 1 and 2 kHz is shown in Fig. 7.1.

Table 7.1: Steady-state tracking error results for x axis scanning.

CTR	e_{max} (%)				e_{rms} (%)			
	100 (Hz)	500 (Hz)	1000 (Hz)	2000 (Hz)	100 (Hz)	500 (Hz)	1000 (Hz)	2000 (Hz)
OL	9.7	12.0	14.5	20.6	6.0	8.1	10.7	15.7
ST	9.9	11.6	15.1	20.2	6.1	8.1	10.8	16.0
FB	2.8	10.0	19.3	37.3	1.4	6.8	13.9	29.2
RC	2.7	2.74	3.7	6.8	0.6	0.8	1.2	2.7
FF	3.9	4.8	5.7	6.9	1.6	2.4	3.0	3.7
SF	3.0	4.2	4.5	4.9	0.9	1.8	2.4	2.5

OL=Open-loop triangle input, FB = PID feedback control, ST = Smooth triangle input, RC = Repetitive control, FF = Dynamic and hysteresis feedforward control, SF = Sinusoidal feedforward input.

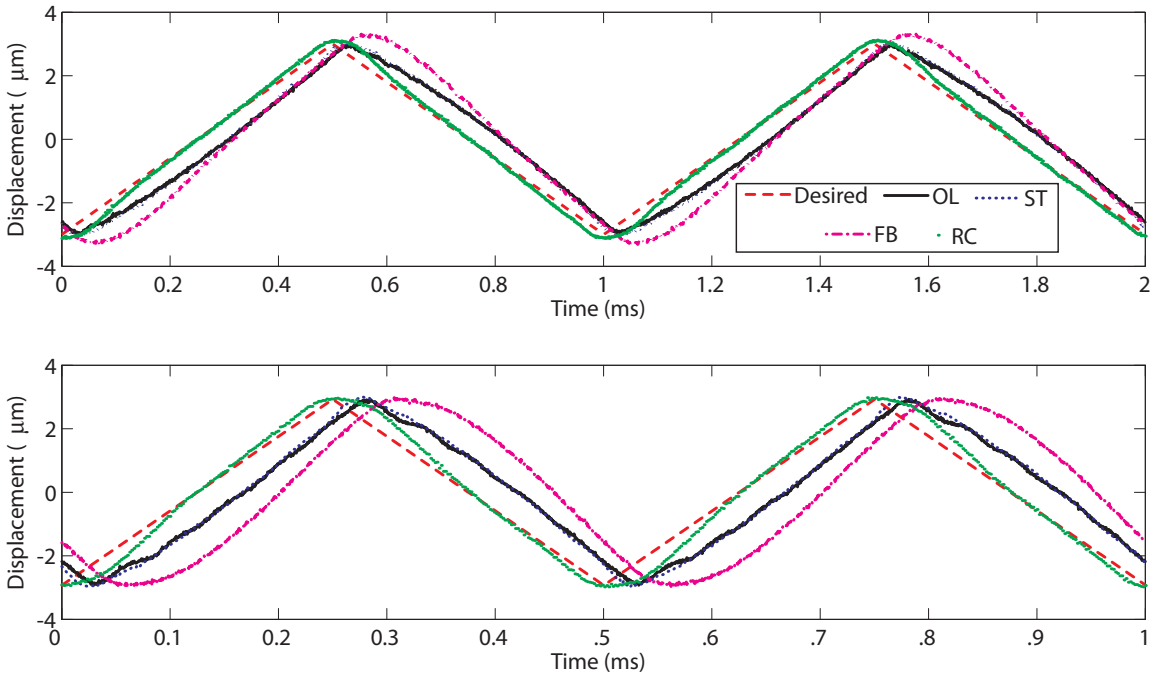

Figure 7.1: Measured tracking results for scanning at (a) 1 kHz and (b) 2 kHz comparing open-loop (OL), smooth triangle (ST), PID feedback (FB), and repetitive control (RC).

7.2 Commercial AFM Imaging

The commercially available nanoScience, Nanosurf® easyScan 2 AFM system is used to obtain preliminary imaging results and to show its mechanical limitations. The NanoSurf AFM system uses electromagnetic actuators to provide a maximum range of 110 μm with a mechanical resonance of approximately 200 Hz. Figure 7.2 shows a the commercial AFM where (a) is a view of the AFM on top of the high-speed nanopositioning stage, (b) the under side of the EasyScan 2 system showing the laser, photodiode, and cantilever chip mount, and (c) shows cantilever replacement.

Preliminary images are obtained using the EasyScan 2 system at 1 and 10 Hz in deflection mode. The commercial scanner is limited by its software to to a maximum line rate to 10 Hz. Figure 7.3 shows the images obtained using the Nanosurf AFM system at (a) 1 and (b) 10 Hz where the fast x-scan dirrection is from left to right and the slow y-scan is from the top down. The light bands are the plateau and the dark bands are the valley of a 20 nm tall, 3 μm pitch step. At 1 Hz the image shows no signs of distortion due to hysteresis, but vertical tracking error along the fast x-axis is apparent where the image gets brighter on the left and right sides. At 10 Hz severe image distortion due to dynamic excitation is seen on the left side of the image in the form of waves. The variances in color (dark to light) along the constant height plateaus and valleys are caused by oscillation in the z-axis while waves along the 45deg valley/plateau boundary line are caused by lateral x-axis tracking error.

7.3 High-Speed Imaging

The NanoSurf easyScan 2 AFM is mounted to the top of the three-axis stage as shown in Fig. 3.17 for AFM imaging experiments. A calibration sample with 3-μm pitch, 20-nm tall features is mounted to the sample platform using a strong adhesive

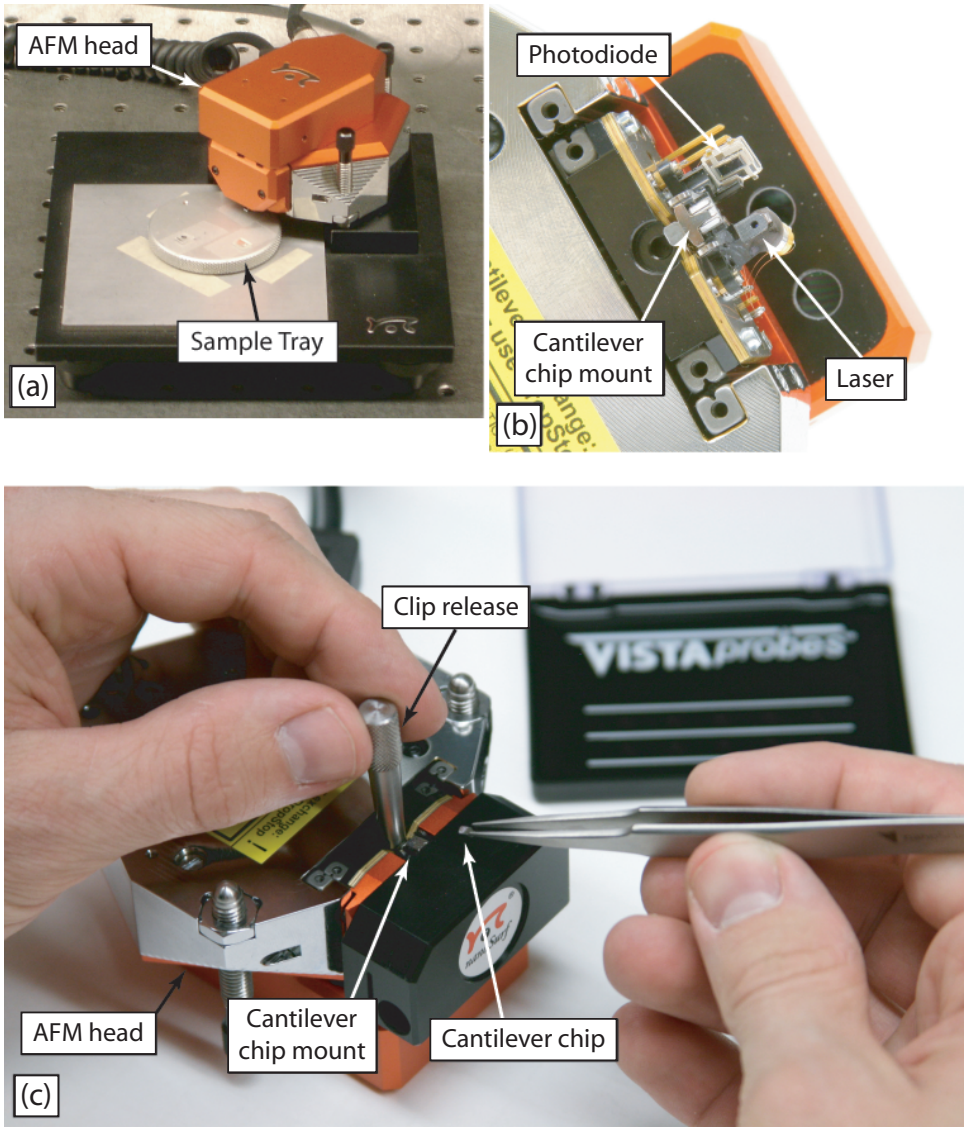

Figure 7.2: NanoSurf EasyScan 2 AFM.

(super glue). Gluing is preferred to minimize relative motion between the sample and sample platform. It is determined that commonly used double-side tape is not adequate for securing the sample for high-speed operation. A non-contact-mode AFM cantilever with a resonance of 360 kHz is used for contact-mode imaging. The AFM head used for imaging is only compatible with cantilevers with alignment grooves. Therefore, only a select group of cantilevers could be used for imaging. The 360 kHz non-contact cantilever is considered the best choice for the experiments. The gains

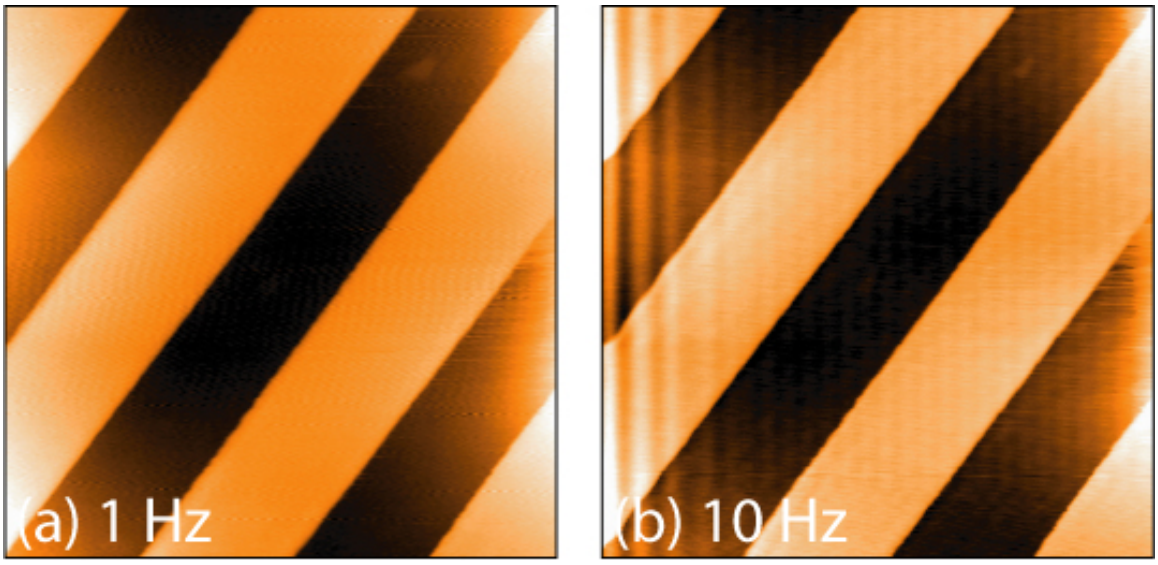

Figure 7.3: AFM images acquired using the commercial AFM system and scanner at 1 and 10 Hz line rate.

for the vertical PI controller to maintain tip-to-sample contact are set relatively low for constant-height imaging. Table 7.2 indicates the PI values used for the vertical feedback controller. The values increase with scan speed to ensure that the probe tip does not lose contact with the sample over the length of the scan. Images are created by plotting the measured cantilever deflection with respect to the desired lateral position of the AFM probe.

Table 7.2: Feedback gains for z-controller.

Line rate HZ	P-gain	I-gain	force setpoint nN
100	500	50	60
500	500	50	60
1,000	1,000	100	60
2,000	10,000	1,000	60

AFM images acquired using the high-speed scanning stage at different scan frequencies with the six control techniques from above are presented in Fig. 7.4. For comparison, Fig. 7.3 shows AFM images acquired at 1 and 10 Hz using the scanner built into the commercial AFM system (see Fig. 3.17). It is quite evident that the

commercial scanner in the AFM is limited to scanning frequencies less than 10 Hz as ripples caused by dynamic effects are present in the image shown in Fig. 3.17(b).

Comparing the AFM images from the commercial AFM's scanner to the newly developed stage, there is an obvious advantage with the high-speed stage.

Vertical measurement or height is shown as variances in color. In the images presented, low points (flat valleys) are dark while high points (flat plateaus) are light. The color variances in constant height features, such as the vertical bands on the flat plateaus and valleys seen in the open loop images greater than 100 Hz, are likely caused by vertical motion of the sample relative to the static AFM head. The sample is aligned so that the linear plateau and valley bands are angled at approximately 45 degrees relative to the x-axis. Curvature or waviness is caused by lateral x/y tracking error. For example hysteresis is observed when the feature line is curved along the length of the band line, lateral vibration is observed where the feature line is wavy, and phase lag is observed where the feature line is angled has a 90 deg. turn at the beginning of the x scan path.

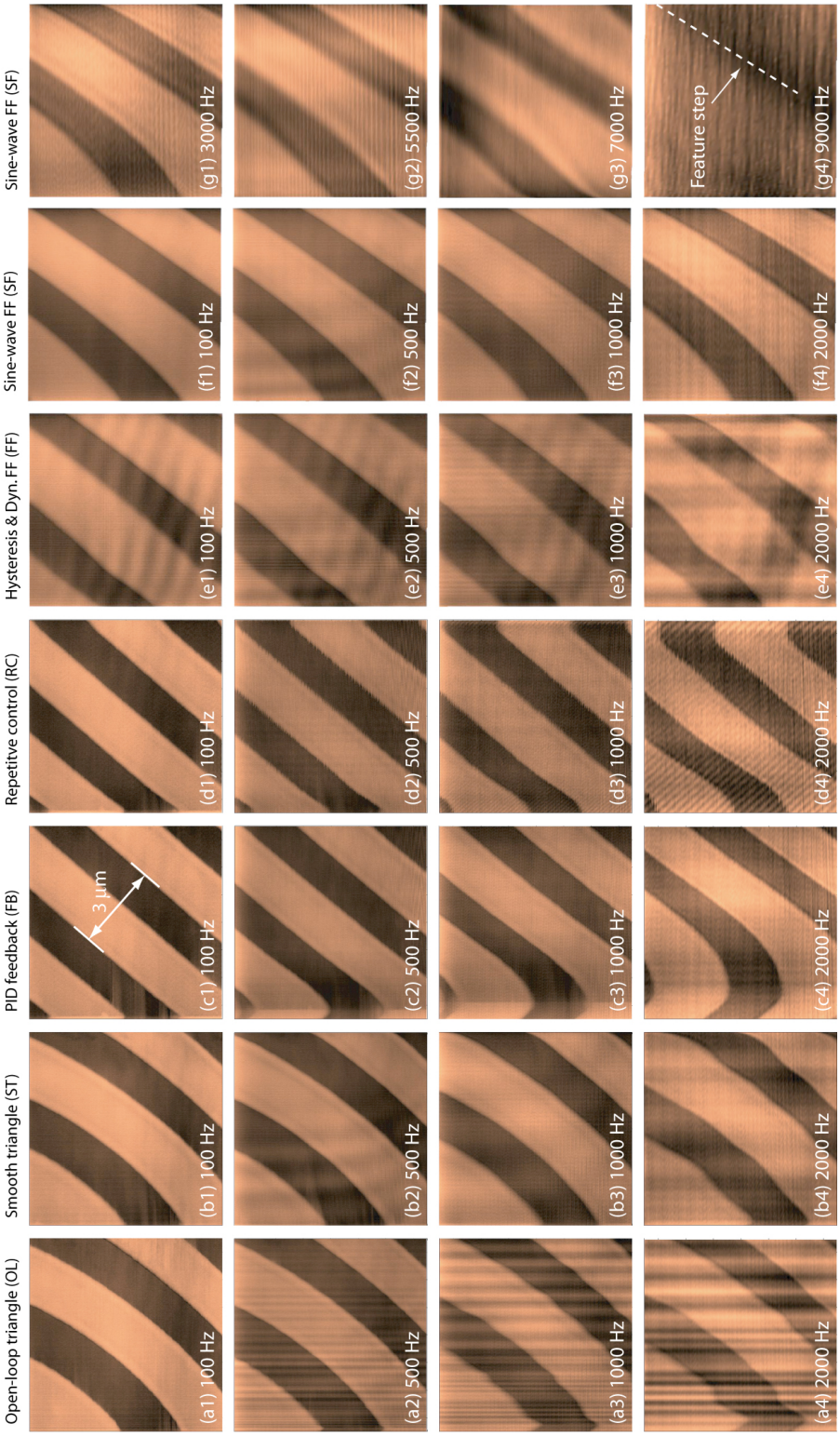

Figure 7.4: AFM images of a calibration sample with 3-μm pitch and 20-nm tall features.

Chapter 8

Discussion

Distortion (ripples) in the commercial AFM image presented in Fig. 7.3(b) show up at 10 Hz with a triangle scan trajectory. For the newly develop scanner, the image is still ripple-free with a triangle trajectory at 100 Hz [Fig. 7.4(a1)]. Instead, dynamic effects are present at 500 Hz [Fig. 7.4(a2)]. Distortion due to hysteresis which causes the parallel features to appear curved represent the major source of image distortion. With increasing frequency under open-loop control with a pure triangle input signal (OL), the tracking error shown in Table 7.1 and Fig. 7.1 are excessively large at 14.5% and 20.6% at 1 and 2 kHz, respectively. Improvement in the image quality is achieved by applying a smooth triangle input (ST) as shown in Fig. 7.4(b1)-(b4). But comparing the tracking error in Table 7.1, the smooth triangular input did not lower the tracking error significantly compared to a regular triangle input. Therefore, the majority of the ripples for the triangle input case may also be caused by exciting the vertical modes of the stage during scanning.

Under PID control, the maximum tracking error at 100 and 500 Hz scanning is 2.8% and 10.0%, respectively (Table 7.1). The hysteresis distortion is minimized by the PID feedback controller. However, at 1 kHz and 2 kHz, the error was significantly larger than the first two cases (Fig. 7.1), indicating that the controller provides

marginal performance at high scan rates. The distortion in the images on the left and right edges is caused by phase delay between the desired and actual response.

The best performing closed-loop control approach tested was RC, where the tracking error is reduced significantly to 2.7% at 100 Hz and 6.8% at 2 kHz (Fig. 7.1). The AFM images show very low distortion at 100 and 500 Hz. The effect of trajectory rounding is obvious at 1 and 2 kHz scan rates. Additionally, high-frequency ripples in the image are observed at 2 kHz scanning due to possible excitation of the vertical and unexpected modes in the x and y stages.

The inverse P-I model and the dynamic-inversion approach [Eq. (6.16)] are applied to compensate for hysteresis and dynamic effects. To minimize exciting undesirable modes, the reference trajectory was chosen as a sine-wave. Overall, the tracking error listed in Table 7.1 for this case (FF) show better performance compared to the two previous open-loop cases, where the error is less than 10% up to 2 kHz scanning. The AFM images [Fig. 7.4(e1)-(e4)] for this case shows a reduction in distortion due to hysteresis as well as the dynamic effect (*i.e.*, phase shift).

To demonstrate high-speed performance above 2 kHz, the feedforward approach [Eq. (6.16)] based on a sine-wave desired trajectory (without hysteresis compensation) was applied. The AFM images in Fig. 7.4(g1)-(g3) demonstrate the stage's capabilities for AFM imaging up to line rates of 7 kHz. A reduced-range image (approximately 1×1 μm) at 9000 Hz presented in Fig. 7.4(g4) shows a noticeable feature step. This scanning rate represents the upper limit of the stage. It is pointed out that compared to the positioning stage found on a commercial AFM system (NanoSurf EasyScan2 AFM), the newly developed nanopositioner offers an improvement in the line rate by a factor of 700 (10 Hz to 7 kHz).

Chapter 9

Conclusions

In conclusion, this thesis presented the design, analysis, and control of a high-speed serial-kinematic nanopositioning stage for AFM imaging purposes. The mechanical design utilizes double-hinged serial-flexures to guide the motion of the lateral x- and y-stages. Out of plane mechanical resonances are increased to values beyond the actuation resonance by increasing the effective vertical stiffness of the flexure system. It is shown that vertical flexure stiffness is increased (while maintaining constant actuation stiffness) by increasing the quantity of flexures, decreasing the flexure thickness and length, and thickening the center section to convert beam flexures into serial-compliant double-hinged flexures.

By increasing the quantity of flexures from 2 to 12 and decreasing the thickness, from 1 to 0.3 mm (and length), the vertical stiffness of the flexures can be increased by as much as 242% (76 to 260 N/μm) while maintaining a constant effective actuation stiffness of 10 N/μm. Further increasing the quantity of flexures and decreasing the flexure thickness will provide higher vertical stiffness. However increasing the quantity of flexures can also increase the effective mass thus reducing dynamic performance, and decreasing the flexure thickness increases stress due to the decreased flexure length. Thickening the center section of the beam flexures in the y-stage from 0.8

to 1.6 mm to form a serial-compliant double-hinged flexure increased the vertical stiffness of the y-flexures by an additional 20%. Through this process, the angular displacement of the flexure is focused at the thinner sections and increases the stress. Additional increases in vertical stiffness can be attained by further increasing the thickness of the center section. The cost of further increasing thickness is increasing the effective mass. Therefore when designing a flexure-guided stage one must consider the effects of added mass and increased stress when increasing quantity and decreasing the length, and thickening the center section to convert the beam flexure into a serial-compliant double-hinged flexure.

For vertical positioning, a new z-axis design is presented. The z-axis design recesses the z-piezoactuators within the x-stage to reduce the effective mass and rotational inertia of the x-stage to increase the mechanical resonances. A plate flexure is attached to the free end of the z-piezoactuator to increase the out-of-plane stiffness and guide the free in the actuation direction. The added plate flexure increases the out-of-plane mechanical resonance values above the actuation resonance. Therefore, by recessing the z-piezoactuator and guiding the free end with a plate flexure is an effective method for increasing the dynamic performance of the both the lateral and vertical positioners.

Four control approaches were investigated and used in AFM imaging: (1) open-loop with smooth inputs, (2) PID feedback control, (3) discretetime repetitive control, and (4) model-based feedforward control. Tracking results and AFM imaging results are presented to demonstrate the performance of the stage. To reduce the excitation of resonance modes caused by pure-triangle trajectory, smooth inputs such as the ten-term Fourier series triangle wave wave are used. PID feedback control is used to increase tracking performance, however scan rates are limited by phase lag. To compensate for phase lag, discretetime repetitive control is used, but scan rates are

limited by the speed of the data acquisition system. Model-based feedforward control to compensate for hysteresis and dynamic behavior is effective, but accurate modeling is essential for good performance. To achieve the fastest scan rates, pure sine wave inputs are used because they are least likely to excite the resonances of the stage. By using dynamic feedforward sine wave inputs, scan rates of 7,000 Hz were achieved. This is an increase by a factor of 700 compared to the commercial AFM which is limited to a line rate of 10 Hz.

9.1 Future Work

Future work includes further increasing the performance of the high-speed stage presented in this thesis, increasing the range of high-speed positioners through the development of dual-stage positioning and control systems, and investigating nanofabrication processes such as probe-based nanomachining.

Improvements in the performance of the nanopositioner presented in this thesis could be achieved by incorporating advanced materials such as metal matrix composites [72], utilizing more advanced flexure geometry such as parabolic flexure fillets [73], and reducing the profile of the x-stage.

As shown in Sec.2.1.3, the maximum achievable resonant frequency of nanopositioners is limited by the range of the positioner. Dual stage positioning is currently used in applications such as computer hard drives [74] to provide large displacement with high-bandwidth performance. By incorporating dual-stage designs and control techniques in nanopositioners, it is expected that high-bandwidth performance can be maintained while increasing range.

Bibliography

[1] K. K. Leang and A. J. Fleming, "High-speed serial-kinematic AFM scanner: design and drive considerations," *Asian Journal of Control, special issue on Advanced Control Methods for Scanning Probe Microscopy*, vol. 11, no. 2, pp. 144–153, 2009.

[2] G. Binnig, C. F. Quate, and C. Gerber, "Atomic force microscope," *Physical Review Letters*, vol. 56, no. 9, p. 930, 1986.

[3] T. Hassenkam, G. E. Fantner, J. A. Cutroni, J. C. Weaver, D. E. Morse, and P. K. Hansma, "High-resolution afm imaging of intact and fractured trabecular bone," *Bone*, vol. 35, no. 1, pp. 4–10, 2004.

[4] S. Kumar, K. Chaudhury, P. Sen, and S. Guha, "Atomic force microscopy: a powerful tool for high-resolution imaging of spermatozoa," *Journal of Nanobiotechnology*, vol. 3, no. 1, p. 9, 2005.

[5] P. K. Hansma, G. Schitter, G. E. Fantner, and C. Prater, "Applied physics: High-speed atomic force microscopy," *Science*, vol. 314, no. 5799, pp. 601–602, 2006, 10.1126/science.1133497.

[6] G. E.Fantner, G. Schitter, J. H.Kindt, T. Ivanov, K. Ivanova, R. Patel, N. Holten-Andersen, J. Adams, P. J. Thurner, I. W. Rangelow, and P. K. Hansma, "Com-

ponents for high speed atomic force microscopy," *Ultramicroscopy*, vol. 106, no. 8-9, pp. 881–887, 2006.

[7] T. Ando, T. Uchihashi, N. Kodera, D. Yamamoto, M. Taniguchi, A. Miyagi, and H. Yamashita, "High-speed atomic force microscopy for observing dynamic biomolecular processes," *Journal of Molecular Recognition*, vol. 20, no. 6, pp. 448–458, 2007.

[8] L. M. Picco, P. G. Dunton, A. Ulcinas, D. J. Engledew, O. Hoshi, T. Ushiki, and M. J. Miles, "High-speed afm of human chromosomes in liquid," *Nanotechnology*, no. 38, p. 384018, 2008.

[9] T. Ando, T. Uchihashi, and T. Fukuma, "High-speed atomic force microscopy for nano-visualization of dynamic biomolecular processes," *Progress in Surface Science*, vol. 83, no. 7-9, pp. 337–437, 2008.

[10] E. I. Goksu, J. M. Vanegas, C. D. Blanchette, W.-C. Lin, and M. L. Longo, "Afm for structure and dynamics of biomembranes," *Biochimica et Biophysica Acta (BBA) - Biomembranes*, vol. 1788, no. 1, pp. 254–266, 2009.

[11] S. H. Kim, A. Opdahl, C. Marmo, and G. A. Somorjai, "Afm and sfg studies of phema-based hydrogel contact lens surfaces in saline solution: adhesion, friction, and the presence of non-crosslinked polymer chains at the surface," *Biomaterials*, vol. 23, no. 7, pp. 1657–1666, 2002, 0142-9612 doi: DOI: 10.1016/S0142-9612(01)00292-7.

[12] D. J. Burns, "On single-molecule dna sequencing with atomic force microscopy using functionalized carbon nanotube probes," Ph.D. dissertation, Massachusetts Institute of Technology, 2004.

[13] A. A. Tseng, A. Notargiacomo, and T. P. Chen, "Nanofabrication by scanning probe microscope lithography: A review," *Journal of Vacuum Science & Technology B: Microelectronics and Nanometer Structures*, vol. 23, no. 3, pp. 877–894, 2005.

[14] A. Jo, W. Joo, W.-J. Jin, H. Nam, and J. K. Kim, "Ultrahigh-density phase-change data storage without the use of heating," *Nat Nano*, vol. 4, no. 11, pp. 727–731, 2009, 1748-3387 10.1038/nnano.2009.260 10.1038/nnano.2009.260.

[15] H. F. Hamann, M. O'Boyle, Y. C. Martin, M. Rooks, and H. K. Wickramasinghe, "Ultra-high-density phase-change storage and memory," *Nat Mater*, vol. 5, no. 5, pp. 383–387, 2006, 1476-1122 10.1038/nmat1627 10.1038/nmat1627.

[16] G. M. Clayton, S. Tien, K. K. Leang, Q. Zou, and S. Devasia, "A review of feedforward control approaches in nanopositioning for high-speed spm," *Journal of Dynamic Systems, Measurement, and Control, Special issue on Dynamic Modeling, Control, and Manipulation at the Nanoscale*, vol. 131, no. 6, p. 061101 (19 pages), 2009.

[17] K. Leang, Q. Zou, and S. Devasia, "Feedforward control of piezoactuators in atomic force microscope systems," *Control Systems Magazine, IEEE*, vol. 29, no. 1, pp. 70–82, 2009, 0272-1708.

[18] B. Bhikkaji, M. Ratnam, A. J. Fleming, and S. O. R. Moheimani, "High-performance control of piezoelectric tube scanners," *IEEE Transactions on Control Systems Technology*, vol. 15, no. 5, pp. 853–866, 2007.

[19] A. J. Fleming, B. J. Kenton, and K. K. Leang, "Bridging the gap between conventional and video-speed scanning probe microscopes," *Ultramicroscopy*, vol. In Press, Corrected Proof, 2010.

[20] M. J. Rost, L. Crama, P. Schakel, E. van Tol, G. B. E. M. van Velzen-Williams, C. F. Overgauw, H. ter Horst, H. Dekker, B. Okhuijsen, M. Seynen, A. Vijftigschild, P. Han, A. J. Katan, K. Schoots, R. Schumm, W. van Loo, T. H. Oosterkamp, and J. W. M. Frenken, "Scanning probe microscopes go video rate and beyond," *Review of Scientific Instruments*, vol. 76, no. 5, p. 053710, 2005.

[21] A. D. L. Humphris, M. J. Miles, and J. K. Hobbs, "A mechanical microscope: High-speed atomic force microscopy," *Applied Physics Letters*, vol. 86, no. 3, pp. 034 106–3, 2005.

[22] L. M. Picco, L. Bozec, A. Ulcinas, D. J. Engledew, M. Antognozzi, M. A. Horton, and M. J. Miles, "Breaking the speed limit with atomic force microscopy," *Nanotechnology*, no. 4, p. 044030, 2007.

[23] G. Schitter, K. J. Astrom, B. E. DeMartini, P. J. Thurner, K. L. Turner, and P. K. Hansma, "Design and modeling of a high-speed afm-scanner," *Control Systems Technology, IEEE Transactions on*, vol. 15, no. 5, pp. 906–915, 2007.

[24] Y. K. Yong and S. O. R. Moheimani, "A compact xyz scanner for fast atomic force microscopy in constant force contact mode," in *IEEE/ASME International Conference on Advanced Intelligent Mechatronics*, Montral, Canada, 2010, pp. 225 – 230.

[25] G. Schitter, K. J. Astrom, B. DeMartini, G. E. Fantner, K. Turner, P. J. Thurner, and P. K. Hansma, "Design and modeling of a high-speed scanner for atomic force microscopy," in *American Control Conference, 2006*, 2006, p. 6 pp.

[26] G. Binnig and D. P. E. Smith, "Single-tube three-dimensional scanner for scanning tunneling microscopy," *Review of Scientific Instruments*, vol. 57, no. 8, pp. 1688–1689, 1986.

[27] G. Schitter and A. Stemmer, "Identification and open-loop tracking control of a piezoelectric tube scanner for high-speed scanning-probe microscopy," *Control Systems Technology, IEEE Transactions on*, vol. 12, no. 3, pp. 449–454, 2004.

[28] G. Schitter, W. F. Rijke, and N. Phan, "Dual actuation for high-bandwidth nanopositioning," in *IEEE Conference on Decision and Control*, Cancun, Mexico, 2008, pp. 5176–5181.

[29] A. J. Fleming, "High-speed vertical positioning for contact-mode atomic force microscopy," in *Proc. IEEE/ASME International Conference on Advanced Intelligent Mechatronics*, Singapore, 2009, pp. 522–527.

[30] O. M. E. Rifai and K. Youcef-Toumi, "Coupling in piezoelectric tube scanners used in scanning probe microscopes," in *American Control Conference*, vol. 4, 2001, pp. 3251 – 3255.

[31] Y. Seo, C. S. Choi, S. H. Han, and S.-J. Han, "Real-time atomic force microscopy using mechanical resonator type scanner," *Review of Scientific Instruments*, vol. 79, no. 10, pp. 103 703–3, 2008.

[32] F. E. Scire and E. C. Teague, "Piezodriven 50-μm range stage with subnanometer resolution," *Review of Scientific Instruments*, vol. 49, no. 12, pp. 1735–1740, 1978.

[33] G. Schitter, P. J. Thurner, and P. K. Hansma, "Design and input-shaping control of a novel scanner for high-speed atomic force microscopy," *Mechatronics*, vol. 18, no. 5-6, pp. 282–288, 2008.

[34] Y. K. Yong, S. S. Aphale, and S. O. R. Moheimani, "Design, identification, and control of a flexure-based xy stage for fast nanoscale positioning," *Nanotechnology, IEEE Transactions on*, vol. 8, no. 1, pp. 46–54, 2009.

[35] Y. Li and Q. Xu, "Development and assessment of a novel decoupled xy parallel micropositioning platform," *Mechatronics, IEEE/ASME Transactions on*, vol. 15, no. 1, pp. 125–135, 2010, 1083-4435.

[36] D. Kim, D. Kang, J. Shim, I. Song, and D. Gweon, "Optimal design of a flexure hinge-based xyz atomic force microscopy scanner for minimizing abbe errors," *Review of Scientific Instruments*, vol. 76, no. 7, pp. 073 706–7, 2005.

[37] B. J. Kenton and K. K. Leang, "Design, characterization, and control of a monolithic three-axis high-bandwidth nanopositioning stage," in *American Control Conference, Special Invited Session on Advances in Actuation for Nanopositioning and Scanning Probe Systems*, Baltimore, MD, USA, 2010, pp. 4949 – 4956.

[38] A. Ballato, "Piezoelectricity: history and new thrusts," in *Ultrasonics Symposium, 1996. Proceedings., 1996 IEEE*, vol. 1, 1996, pp. 575–583 vol.1.

[39] N. Group, "Piezo ceramics," p. 7, 2010.

[40] W. D. J. Callister, *Materials Science and Engineering an Introduction*. New York: John Whiley and Sons, Inc., 1997.

[41] P. Instrumente, "Designing with piezoelectrics: Nanopositioning fundamentals," 11/14/2005 2005.

[42] J. M. Paros and L. Weisbord, "How to design flexure hinges," *Machine Design*, pp. 151 – 156, 1965.

[43] N. Lobontiu, *Compliant Mechanisms Design of Flexure Hinges*. CRC Press, 2003.

[44] G. Binnig, H. Rohrer, C. Gerber, and E. Weibel, "Surface studies by scanning tunneling microscopy," *Phys. Rev. Lett.*, vol. 49, no. 1, pp. 57–61, 1982.

[45] G. Binnig, C. Gerber, E. Stoll, T. R. Albrecht, and C. F. Quate, "Atomic resolution with atomic force microscope," *Surface Science*, vol. 189-190, pp. 1–6, 1987, 0039-6028 doi: DOI: 10.1016/S0039-6028(87)80407-7.

[46] D. J. Burns, "On single-molecule dna sequencing with atomic force microscopy using functionalized carbon nanotube probes," Ph.D. dissertation, Massachusetts Institute of Technology, 2001.

[47] P. Instrumente, "Piezo nano positionoing: Inspirations 2009," 2009.

[48] J. H.Kindt, G. E.Fantner, J. A.Cutroni, and P. K.Hansma, "Rigid design of fast scanning probe microscopes using finite element analysis," *Ultramicroscopy*, vol. 100, no. 3-4, pp. 259–265, 2004.

[49] T. Ando, N. Kodera, T. Uchihashi, A. Miyagi, R. Nakakita, H. Yamashita, and K. Matada, "High-speed atomic force microscopy for capturing dynamic behavior of protein molecules at work," *e-Journal of Surface Science and Nanotechnology*, vol. 3, pp. 384–392, 2005.

[50] P. Gao, S. M. Swei, and Z. J. Yuan, "A new piezodriven precision micropositioning stage utilizing flexure hinges," *Nanotechnology*, vol. 10, no. 4, pp. 394–398, 1999.

[51] S. G. Kelly, *Fundamentals of Mechanical Vibrations*, 2nd ed. Boston: McGraw-Hill, 2000.

[52] S. P. Timoshenko, *History of Strength of Materials*. New York: McGraw-Hill Book Company, 1953.

[53] R. R. J. Craig, *Mechanics of Materials, 2nd ed.* New York: John Wiley & Sons, 2000.

[54] W. C. Young and R. G. Budynas, *Roark's Formulas fo Stress and Strain*, 7th ed. New York: McGraw-Hill, 2002.

[55] S. R. Park and S. H. Yang, "A mathematical approach for analyzing ultra precision positioning system with compliant mechanism," *Journal of Materials Processing Technology*, vol. 164-165, pp. 1584–1589, 2005, 0924-0136 doi: DOI: 10.1016/j.jmatprotec.2005.02.018.

[56] Y. Li and Q. Xu, "A novel design and analysis of a 2-dof compliant parallel micromanipulator for nanomanipulation," *Automation Science and Engineering, IEEE Transactions on*, vol. 3, no. 3, pp. 247–254, 2006, 1545-5955.

[57] Q. Xu and Y. Li, "Structure improvement of an xy flexure micromanipulator for micro/nano scale manipulation," in *17th IFAC World Congress*, M. P. Chung, Myung Jin, Ed., vol. 17. Seoul, Korea: Elsevier, 2008, pp. 12 733 – 12 738.

[58] S. Awtar and A. H. Slocum, "Constraint-based design of parallel kinematic xy flexure mechanisms," *Journal of Mechanical Design*, vol. 129, no. 8, pp. 816–830, 2007.

[59] Y. Li and Q. Xu, "Design and analysis of a totally decoupled flexure-based xy parallel micromanipulator," *Trans. Rob.*, vol. 25, no. 3, pp. 645–657, 2009, 1653137.

[60] K. K. Leang, Q. Zou, and S. Devasia, "Feedforward control of piezoactuators in atomic force microscope systems: inversion-based compensation for dynamics and hysteresis," *IEEE Cont. Syst. Mag., Special Issue on Hysteresis*, vol. 29, no. 1, pp. 70 – 82, 2009.

[61] A. J. Fleming and A. G. Wills, "Optimal periodic trajectories for band-limited systems," *IEEE Control Systems Technology*, vol. 13, no. 3, pp. 552 – 562, 2009.

[62] K. K. Leang and S. Devasia, "Feedback-linearized inverse feedforward for creep, hysteresis, and vibration compensation in AFM piezoactuators," *IEEE Trans. Cont. Syst. Tech.*, vol. 15, no. 5, pp. 927 – 935, 2007.

[63] B. A. Francis and W. M. Wonham, "The internal model principle of control theory," *Automatica*, vol. 12, no. 5, pp. 457 – 465, 1976.

[64] T. Inoue, M. Nakano, and S. Iwai, "High accuracy control of a proton synchrotron magnet power supply," in *Proc. 8thWorld Congr. IFAC*, 1981, pp. 216 – 221.

[65] M. Tomizuka, "Zero phase tracking algorithm for digital control," *ASME J. Dyn. Syst. Meas. and Cont.*, vol. 109, pp. 65 – 68, 1987.

[66] B. Zhang, D. Wang, K. Zhou, and Y. Wang, "Linear phase lead compensation repetitive control of a CVCF PWM inverter," *IEEE Trans. Industrial Electronics*, vol. 55, no. 4, pp. 1595 – 1602, 2008.

[67] K. Zhou and J. C. Doyle, *Essentials of robust control*. Prentice-Hall, Inc., 1998.

[68] U. Aridogan, Y. Shan, and K. K. Leang, "Design and analysis of discrete-time repetitive control for scanning probe microscopes," *ASME J. Dyn. Syst. Meas. and Cont., Special issue on Dynamic Modeling, Control, and Manipulation at the Nanoscale*, vol. 131, p. 061103 (12 pages), 2009.

[69] M. Brokate and J. Sprekels, *Hysteresis and phase transitions*. New York: Springer, 1996.

[70] M. A. Janaideh, C.-Y. Su, and S. Rakheja, "Development of the rate-dependent prandtl-ishlinskii model for smart actuators," *Smart Mater. Struct.*, vol. 17, p. 035026 (11pp), 2008.

[71] Y. Shan and K. K. Leang, "Repetitive control with Prandtl-Ishlinskii hysteresis inverse for piezo-based nanopositioning," in *American Control Conference, Invited Session on Advances in Control of Nanopositioning and SPM Systems*, St. Louis, MO, 2009, pp. 301 – 306.

[72] T. P. D. Rajan, R. M. Pillai, and B. C. Pai, "Characterization of centrifugal cast functionally graded aluminum-silicon carbide metal matrix composites," *Materials Characterization*, vol. In Press, Corrected Proof, 2010, 1044-5803 doi: DOI: 10.1016/j.matchar.2010.06.002.

[73] N. Lobontiu, J. S. N. Paine, E. O'Malley, and M. Samuelson, "Parabolic and hyperbolic flexure hinges: flexibility, motion precision and stress characterization based on compliance closed-form equations," *Precision Engineering*, vol. 26, no. 2, pp. 183–192, 2002.

[74] R. Horowitz, Y. Li, K. Oldham, S. Kon, and X. Huang, "Dual-stage servo systems and vibration compensation in computer hard disk drives," *Control Engineering Practice*, vol. 15, no. 3, pp. 291–305, 2007, 0967-0661 doi: DOI: 10.1016/j.conengprac.2006.09.003.

Appendix A

Matlab Files

A.1 Ten-Term Fourier Triangle Trajectory

```
% Brian Kenton
% Fourier series triangle reference trajectory
% March 1st, 2010
% TenTermFourierTriangleRoundedInput

close all
clear all
clc

A = 5.048;                  % Voltage amplitude !!!!(1/2 of VPP)!!!!!
p = 1;                      % Number of periods
c = 1;                      % constant = 1
n = 1000;                   % Number of Data points
i = 2/(n*p);                % points
x = 0:(i*p):(p*2-i);        % Data point array

Xt = 0:2*pi/n:2*pi;
XR = A*sawtooth(Xt,.5);     % Pure triangle signal

s1 = (1-(-1)^1)/1^2*cos(1*pi*x/c);
s2 = (1-(-1)^2)/2^2*cos(2*pi*x/c);
s3 = (1-(-1)^3)/3^2*cos(3*pi*x/c);
s4 = (1-(-1)^4)/4^2*cos(4*pi*x/c);
s5 = (1-(-1)^5)/5^2*cos(5*pi*x/c);
s6 = (1-(-1)^6)/6^2*cos(6*pi*x/c);
s7 = (1-(-1)^7)/7^2*cos(7*pi*x/c);
s8 = (1-(-1)^8)/8^2*cos(8*pi*x/c);
s9 = (1-(-1)^9)/9^2*cos(9*pi*x/c);
s10 = (1-(-1)^10)/10^2*cos(10*pi*x/c);

% Ten term Fourier series triangle
fx10 = .5*c-2*c/(pi^2)*(s1+s2+s3+s4+s5+s6+s7+s8+s9+s10);
```

```
fx10 = (fx10-.5);           % Centered about zero
fx10 = fx10/max(fx10)*A;    % Re-scaled for 7 um of displacement
fx10 = fx10';

figure(1)
plot(XR,'k')
hold on
plot(fx10)
axis([0,1e3,-6,6]);
title({'Ten-term fourier triangle';'reference trajectory'})
xlabel('Data point');
ylabel('Volts');
legend('Pure triangle','Ten-term fourier triangle');

save FourTri10_1000_7mum.txt -ascii fx10
```

A.2 Frequency Response Plotting

```
%  High-speed XYZ nanopositioner
%  freq. resp
%  January 20th, 2010
%  Measurements taken with x-inductive sensors bolted to stage
%  and Laser sensor mounted to table.

close all
clear all

% ======================================================================
%X-outpyt
% X-axis FEA Predicted
load XX.txt %x/x COSMOS - 1 - 100k
w_hzXX = XX(:,1);
magXX = 20*log10(abs(XX(:,2)));
% X-axis inductive sensor
!srt785 /omat 1KXXI.78D
[w_hzXXIS,GXXIS,mXXIS,phXXIS] = vib_fr_is('1KXXI.mat');  % X - in
% X-axis laser Sensor Data
!srt785 /omat 1KXXL.78D
[w_hzXXL,GXXL,mXXL,phXXL] = vib_fr('1KXXL.mat');  % X - in

% ======================================================================
%Y-output
% Y-axis FEA Predicted
load YY.txt %y/y COSMOS - 1 - 100k
w_hzYY = YY(:,1);
magYY = 20*log10(abs(YY(:,2)));
% Y-axis inductive sensor
!srt785 /omat 1KYYI.78D
[w_hzYYIS,GYYIS,mYYIS,phYYIS] = vib_fr_is('1KYYI.mat');  % Y - in
% Y-axis laser Sensor Data
!srt785 /omat 1KYYL.78D
[w_hzYYL,GYYL,mYYL,phYYL] = vib_fr('1KYYL.mat');  % Y - in

figure(1); clf;

subplot(321);
semilogx(w_hzXX,magXX,'k');
axis([1e3,1e5,-130,-50]);
title({'High-speed (x-axis)';'FEA Predicted'});
ylabel('Mag. (dB)');

subplot(323);
semilogx(w_hzXXIS,mXXIS,'k');
axis([1e3,1e5,-90,-10]);
title('Inductive sensor on y-stage');
ylabel('Mag. (dB)');
```

```
49
50 subplot(325);
51 semilogx(w_hzXXL,mXXL,'k');
52 axis([1e3,1e5,-120,-40]);
53 title('Laser sensor on table');
54 xlabel('Frequency (Hz)');
55 ylabel('Mag. (dB)');
56
57 subplot(322);
58 semilogx(w_hzYY,magYY,'k');
59 axis([1e3,1e5,-150,-50]);
60 title({'Low-speed (y-axis)';'FEA Predicted'});
61 ylabel('Mag. (dB)');
62
63 subplot(324);
64 semilogx(w_hzYYIS,mYYIS,'k');
65 axis([1e3,1e5,-100,0]);
66 title('Inductive sensor');
67 ylabel('Mag. (dB)');
68
69 subplot(326);
70 semilogx(w_hzYYL,mYYL,'k');
71 axis([1e3,1e5,-140,-40]);
72 title('Laser sensor on table');
73 xlabel('Frequency (Hz)');
74 ylabel('Mag. (dB)');
```

Appendix B

Review of Nanopositioners

Mfg.	Model	DOF	Res.	Range	Dir.
Picco *et al.*, 2007 [22]		XY	32,000	2	X
Picco *et al.*, 2007 [22]		XY	100,000	1	X
Humphris *et al.*, 2005 [21]			20,000	4.2	X
Schitter *et al.*, 2007 [23]		XYZ	22,000	13	XY
			33000	4.3	Z
Ando *et al.*, 2008 [9]			45,000	1	
Fleming *et al.*, 2010 [19]		Z	103,000	2.3	Z
Kenton & Leang, 2010 [37]		XYZ	24,200	9	X
			6,000	9	Y
			70,000	1	Z
Schitter & Stemmer, 2004 [27]		XYZ	950	125	
Li & Xu, 2010 [35]		XY	165	117	
Rost *et al.*, 2005 [20]		XYZ	64,000	0.3	X
			>100,000	0.2	X
Yong *et al.*, 2009 [34]		XY	2,700	25	XY
Yong & Moheimani, 2010 [24]		XYZ	10,000	4.2	X
			10,000	5	Y
			10,000	3.4	Z
Kim *et al.*, 2005 [36]		XYZ	127	120.8	X
			220	130	Y
			2,860	11	Z
MadCityLabs	Nano-LPS100	XYZ	450	100	X
			350	100	Y
			450	100	Z
	Nano-LPS200	XYZ	400	200	X
			300	200	Y
			350	200	Z
	Nano-LPS300	XYZ	350	300	X
			250	300	Y
			250	300	Z

MadCityLabs	Nano-LPQ	XYZ	1,000	75	X
			1,000	50	Z
	Nano-Mini		650	10	Z
	Nano-PDQ50	XYZ	2,500	50	X
			1,500	50	Y
			1,000	50	Z
	Nano-PDQ75	XYZ	2,500	75	X
			1,500	75	Y
			1,000	75	Z
	NanoT 100x100x20	XYZ	450	100	X
			250	100	Y
			450	20	Z
	NanoT 200x200x50	XYZ	400	200	X
			200	200	Y
			350	50	Z
	Nano-M250	XY	1,000	50	X
			700	50	Y
	Nano-M350	XYZ	1,000	50	X
			700	50	Y
			700	25	Z
	Nano-Max50	XY	1,500	50	X
			1,000	50	Y
	Nano-H100	XY	500	100	X
			250	100	Y
	Nano-H50	XY	500	50	X
			250	50	Y
	Nano-3D200	XYZ	150	200	XY
			500	200	Z
	Nano-3D500	XYZ	150	500	XY
			500	500	Z
	Nano-UHV200	XYZ	300	200	XY
			150	200	Y
			175	200	Z
	NanoHS2		1,500	10	XY
	NanoHS3	XYZ	1,000	10	XY
			5,000	10	Z
	Nano-Z500	Z	250	500	Z
	Nano-Bio2M	XY	500	50	X
			400	50	Y
	Nano-Bio100	XY	450	100	X
			350	100	Y
	Nano-Bio-200	XY	400	200	X
			300	200	Y

MadCityLabs	Nano-BioS100	XY	400	100	X
			280	100	Y
	Nano-BioS200	XY	350	200	X
			230	200	Y
	Nano-BioS300	XY	300	300	X
			180	300	Y
Physik Instrumente	P-313	XY	4,000	1	
	P-363	XYZ	9,800	5	
	P-517.2	XY	450	130	
	P-527.2	XY	350	250	
	P-541.2	XY	255	175	
	P-542.2	XY	230	290	
	P-541.2	XY	1,550	60	
	P-561.3CD	XYZ	190	150	
	P-562.3	XYZ	160	300	
	P-563.3	XYZ	140	340	
	P-561.3DD	XYZ	920	58	
	P-587.6CD	6DOF	800	103	
	P-601.1	Z	750	100	
	P-601.3	Z	440	250	
	P-601.4	Z	350	400	
	P-611.2S	XY	345	120	
	P-611.XZO	XY	365	120	
	P-611.1	X	400	120	
	P-612.2	XY	400	130	
	P-615.3	XYZ	210	420	XY
	P-620.1	X	1,100	60	
	P-620.2	XY	575	60	
	P-621.1	X	800	120	
	P-621.2	XY	420	120	
	P-622.1	X	400	300	
	P-622.2	XY	225	300	
	P-625.1	X	215	600	
	P-625.2	XY	135	600	
	P-628.1	X	125	950	
	P-628.2	XY	75	950	
	P-629.1	X	125	1,800	
	P-629.2	XY	60	1,800	
	P-631.1	X	800	120	
	P-712.1	X	1,550	40	
	P-713.2, P-714.2	XY	2,250	20	
	P-713P-714		2,176	20	
	P-733.2C	XY	500	115	

Physik Instrumente	P-733.3C	XYZ	460	115	
	P-733.2D	XY	2,230	33	
	P-733.3D	XYZ	1,200	33	
	P-734.2	XY	500	110	
	P-750	X	600	75	
	P-752.1	X	3,200	20	
	P-752.2	X	2,100	35	
	P-753.11	X	2,500	12	
	P-753.21	X	1,700	25	
	P-753.31	X	1,400	38	
	P-772.1	X	1,700	12	
	P-915KLVS	XYZ	110	100	
	P-915KXYS	XY	4		
	P-915KHDS	XY	1,850	15	
	S-303	Z	25,000	3	
Thor Labs	APB301	XYZ	150	90	
Npoint	NPX25A	X	4,000	25	X
	NPZ25A	Z	4,000	25	Z
	NPZ25B	Z	1,600	25	Z
	NP270A	Z	2,000	70	Z
	NPX100A	X	1,100	100	X
	NPX100B	X	900	100	X
	NPX150A	X	630	150	X
	NPX200A	X	600	200	X
	NPX200B	X	300	200	X
	NPXY30A	XY	2,500	20	XY
	NPXY100A	XY	700	100	XY
	NPXY100B	XY	1,000	100	XY
	NPXY100C	XY	400	100	XY
	NPXY100D	XY	700	100	XY
	NPXY100E	XY	1,000	100	XY
	NPXY150A	XY	800	150	XY
	NPXY200A	XY	400	200	XY
	NPXY200B	XY	400	200	XY
	NPXY200C	XY	200	200	XY
	NPXY400A	XY	300	400	XY
	NPXY50Z50A	XYZ	1,000	50	XY
			1,000	50	Z
	NPXY100Z10A	XYZ	600	100	XY
			1,600	10	Z
	NPXY100Z15A	XYZ	500	100	XY
			5,000	15	Z

NPoint	NPXY100Z25A	XYZ	400	100	XY
			1600	25	Z
	NPXY100Z25B	XYZ	300	100	XY
			1,500	25	Z
	NPXY100Z100	XYZ	600	100	XY
			600	100	Z
	NPXY150Z10	XYZ	500	150	XY
			1,600	10	Z
	NPXY200Z25A	XYZ	350	200	XY
			1,600	25	Z
	NPXY200Z25B	XYZ	250	200	XY
			1,500	25	Z
	NPXY400Z100A	XYZ	200	400	XY
			1,000	100	Z
Queensgate Instruments	NPS-X-15A	X	3,000	15	X
	NPS-Z-15A	Z	2,500	15	Z
	NPS-Z-15B	Z	1,800	15	Z
	NPS-Z-15H	Z	900	15	Z
	NPS-Z-15L	Z	8,000	15	Z
	NPS-XY-100A	XY	350	100	XY
	NPS-XY-100B	XY	600	100	XY